ADVANCED STEEL CONSTRUCTION

An International Journal

Volume 10 Number 4

December 2014

CONTENTS

Technical Papers

Website: *http://www.hkisc.org*
ISSN 1816-112X
Science Citation Index Expanded, Materials Science Citation Index and ISI Alerting

Cover: Flower Dome Conservatories @Gardens by The Bay, Singapore

ADVANCED STEEL CONSTRUCTION

VOL.10, NO.4 (2014)

ADVANCED STEEL CONSTRUCTION

an International Journal

ISSN 1816-112X

Volume 10 Number 4 *December 2014*

ISSN 1816-112X

Science Citation Index Expanded, Materials Science Citation Index and ISI Alerting

Advanced Steel Construction
an international journal

Cover: Flower Dome Conservatories @Gardens by The Bay, Singapore
The two arch structures behind the big trees. Grand Award of IStructE-UK/Structural Division-HKIE 2013. Stability design by second-order direct analysis without effective length, jointly by The National University of Singapore and The Hong Kong Polytechnic University

General Information
Advanced Steel Construction, an international journal

Aims and scope

The International Journal of Advanced Steel Construction provides a platform for the publication and rapid dissemination of original and up-to-date research and technological developments in steel construction, design and analysis. Scope of research papers published in this journal includes but is not limited to theoretical and experimental research on elements, assemblages, systems, material, design philosophy and codification, standards, fabrication, projects of innovative nature and computer techniques. The journal is specifically tailored to channel the exchange of technological know-how between researchers and practitioners. Contributions from all aspects related to the recent developments of advanced steel construction are welcome.

Instructions to authors

Submission of the manuscript. Authors may submit double-spaced manuscripts preferably in MS Word by emailing to one of the chief editors as follows for arrangement of review. Alternatively papers can be submitted on a diskette to one of the chief editors.

Asian Pacific , African and organizing editor : Professor S.L. Chan, Email: ceslchan@polyu.edu.hk
American editor : Professor W.F. Chen, Email: waifah@hawaii.edu
European editor : Professor R. Zandonini, Email: riccardo_zandonini@ing.unitn.it

All manuscripts submitted to the journal are recommended to accompany with a list of four potential reviewers suggested by the author(s). This list should include the complete name, address, telephone and fax numbers, email address, and at least five keywords that identify the expertise of each reviewer. This scheme will improve the process of review.

Style of manuscript

General. Author(s) should provide full postal and email addresses and fax number for correspondence. The manuscript including abstract, keywords, references, figures and tables should be in English with pages numbered and typed with double line spacing on single side of A4 or letter-sized paper. The front page of the article should contain:

a) a short title (reflecting the content of the paper);
b) all the name(s) and postal and email addresses of author(s) specifying the author to whom correspondence and proofs should be sent;
c) an abstract of 100-200 words; and
d) 5 to 8 keywords.

The paper must contain an introduction and a conclusion. The length of paper should not exceed 25 journal pages (approximately 15,000 words equivalents).

Tables and figures. Tables and figures including photographs should be typed, numbered consecutively in Arabic numerals and with short titles. They should be referred in the text as Figure 1, Table 2, etc. Originally drawn figures and photographs should be provided in a form suitable for photographic reproduction and reduction in the journal.

Mathematical expressions and units. The Systeme Internationale (SI) should be followed whenever possible. The numbers identifying the displayed mathematical expression should be referred to in the text as Eq. (1), Eq. (2).

References. References to published literature should be referred in the text, in the order of citation with Arabic numerals, by the last name(s) of the author(s) (e.g. Zandonini and Zanon [3]) or if more than three authors (e.g. Zandonini et al. [4]). References should be in English with occasional allowance of 1-2 exceptional references in local languages and reflect the current state-of-technology. Journal titles should be abbreviated in the style of the Word List of Scientific Periodicals. References should be cited in the following style [1, 2, 3].

Journal: [1] Chen, W.F. and Kishi, N., "Semi-rigid Steel Beam-to-column Connections, Data Base and Modelling", Journal of Structural Engineering, ASCE, 1989, Vol. 115, No. 1, pp. 105-119.
Book: [2] Chan, S.L. and Chui, P.P.T., "Non-linear Static and Cyclic Analysis of Semi-rigid Steel Frames", Elsevier Science, 2000.
Proceedings: [3] Zandonini, R. and Zanon, P., "Experimental Analysis of Steel Beams with Semi-rigid Joints", Proceedings of International Conference on Advances in Steel Structures, Hong Kong, 1996, Vol. 1, pp. 356-364.

Proofs. Proof will be sent to the corresponding author to correct any typesetting errors. Alternations to the original manuscript at this stage will not be accepted. Proofs should be returned within 48 hours of receipt by Express Mail, Fax or Email.

Copyright. Submission of an article to "Advanced Steel Construction" implies that it presents the original and unpublished work, and not under consideration for publication nor published elsewhere. On acceptance of a manuscript submitted, the copyright thereof is transferred to the publisher by the Transfer of Copyright Agreement and upon the acceptance of publication for the papers, the corresponding author must sign the form for Transfer of Copyright.

Permission. Quoting from this journal is granted provided that the customary acknowledgement is given to the source.

Page charge and Reprints. There will be no page charges if the length of paper is within the limit of 25 journal pages. A total of 30 free offprints will be supplied free of charge to the corresponding author. Purchasing orders for additional offprints can be made on order forms which will be sent to the authors. These instructions can be obtained at the Hong Kong Institute of Steel Construction, Journal website: http://www.hkisc.org

The International Journal of Advanced Steel Construction is published quarterly by learnt society, The Hong Kong Institute of Steel Construction, c/o Department of Civil & Environmental Engineering, The Hong Kong Polytechnic University, Hung Hom, Kowloon, Hong Kong.

Subscription inquiries and change of address. Address all subscription inquiries and correspondence to Member Records, IJASC. Notify an address change as soon as possible. All communications should include both old and new addresses with zip codes and be accompanied by a mailing label from a recent issue. Allow six weeks for all changes to become effective.

The Hong Kong Institute of Steel Construction
HKISC
c/o Department of Civil and Environmental Engineering,
The Hong Kong Polytechnic University,
Hunghom, Kowloon, Hong Kong, China.
Tel: 852- 2766 6047 Fax: 852- 2334 6389
Email: *ceslchan@polyu.edu.hk* Website: *http://www.hkisc.org/*
ISSN 1816-112X
Science Citation Index Expanded, Materials Science Citation Index and ISI Alerting

ISSN 1816-112X

Science Citation Index Expanded, Materials Science Citation Index and ISI Alerting

Advanced Steel Construction
an international journal

VOLUME 10 NUMBER 4 DECEMBER 2014

Technical Papers

A SIMPLIFIED METHOD FOR SEISMIC PERFORMANCE EVALUATION OF STEEL BRIDGE PIERS WITH THIN-WALLED STIFFENED BOX SECTIONS

Jiandong Zhang[1,2], Chun-Lin Wang[1] and Hanbin Ge[1,3*]

[1] *International Institute for Urban Systems Engineering, Southeast University, Sipailou 2, Nanjing 210096, China*
[2] *Jiangsu Transportation Research Institute Co., Ltd, Nanjing, 210017, China*
[3] *Department of Civil Engineering, Meijo University, Tempaku-ku, Nagoya 468-8502, Japan*
**(Corresponding author: E-mail: gehanbin@meijo-u.ac.jp)*

Received: 28 September 2012; Revised: 22 December 2012; Accepted: 27 December 2012

ABSTRACT: This paper proposes a simplified seismic evaluation method for the thin-walled stiffened box steel pier to predict its strength and ductility. In this method, two modified bilinear material models for the fiber-beam element are suggested to include the local buckling of the base stiffened plate. An experiment validated a shell element based model, which was selected for comparison with the proposed fiber-beam based model. Twelve numerical cases were then simulated by the shell element based model and the fiber-beam element based model, respectively, and their accuracies were compared with each other. Numerical results showed that the proposed pushover method, employing the amended bilinear kinematic material model for the fiber beam element, is of good accuracy. If the maximum strength is taken as the ultimate point, the bilinear material model, replacing the yield point by the buckling stress, is recommended. If 95 percent of the maximum strength after the peak is regarded as the ultimate point, the elastic-perfectly plastic material model is suggested.

Keywords: Steel Bridge, Seismic Evaluation Method, Stiffened Box Section, Fiber Element

1. INTRODUCTION

Cantilever-type steel columns of thin-walled box sections are widely used as bridge piers in urban area. Up to now, investigations on the strength and ductility of thin-walled steel bridge piers under cyclic and dynamic loading have been extensively carried out for evaluating their seismic performance, and a great deal of knowledge has been achieved (e.g. Usami and Ge [1], Ge et al. [2], Usami et al. [3], Susantha et al. [4]). The local and overall interaction buckling of the thin-walled stiffened steel piers is regarded as one reason for the failure during the earthquake (Galambos [5]). Many researchers used the finite-element (FE) based analysis to predict the hysteretic behavior and failure modes of the thin-walled steel members under cyclic loading (e.g. Gao et al. [6], Goto et al. [7]). Although the FE numerical approaches, employing the shell elements, can accurately simulate the buckling of the thin-walled box member, as given in the literature (Ge et al. [2]), the FE models included the complex element grids, whose sizes remarkably affected the results. Besides, the FE model building is a complicated and time-consuming process, which cannot be accepted and popular for normal designers in engineering practice.

A relatively simplified evaluation method, instead of the time-consuming shell element based simulation, is very urgent in the case that the thin-walled box members are applied in the structural design. Sakimoto et al. [8] proposed a new stress-strain relation for the fiber-beam based simulation of the thin-walled box member. This average stress-strain relationship was obtained from the shell element based simulation and included the effect of the stiffened plate's local buckling. Therefore, it exhibited a strain softening behavior and can be described as a function of a slenderness parameter of the stiffened plate. However, numerical results were susceptible to the size of the element because of its strain-softening behavior. Afterwards, a buckling element with a finite length was introduced in order to avoid the strain concentration in the small softening element by Ozawa

et al. [9]. Numerical examples confirmed that the pushover analysis with the new nonlinear beam element can predict the ultimate behavior of the steel piers. However, it is not easy for engineers to use in practical design because the proposed model equation has 36 coefficients without giving their values in the paper and the applicable range is limited (e.g., the width-thickness ratio parameter as shown later in Eq .1 is from 0.3-0.5).

In this paper, taking into account the local buckling of the thin-walled steel stiffened plate, the characteristics of the bilinear material model was modified. First, the comparison of a shell element based simulation with an experiment showed the effectiveness of the shell element based model. Second, a simplified pushover method based on the fiber-beam element in which the material model included the effect of the stiffened plate's local buckling was proposed. Furthermore, the predicted ultimate load-carrying capacities of the thin-walled steel box piers were compared between the proposed method and the shell element based simulation.

2. VERIFICATION OF SHELL-ELEMENT BENCHMARK MODEL

2.1 Specimen Configuration

A cantilever steel column with uniform square cross section, subjected to a constant axial force and cyclic lateral loading, was given in the literature (Nishikawa et al. [10]). As shown in Figure 1, this column was stiffened by both longitudinal stiffeners and diaphragms. In the present study, the test results of the No.4 specimen (Nishikawa et al. [10]) are employed to calibrate the shell element based simulation. Its geometrical dimensions and material properties are listed in Tables 1 and 2.

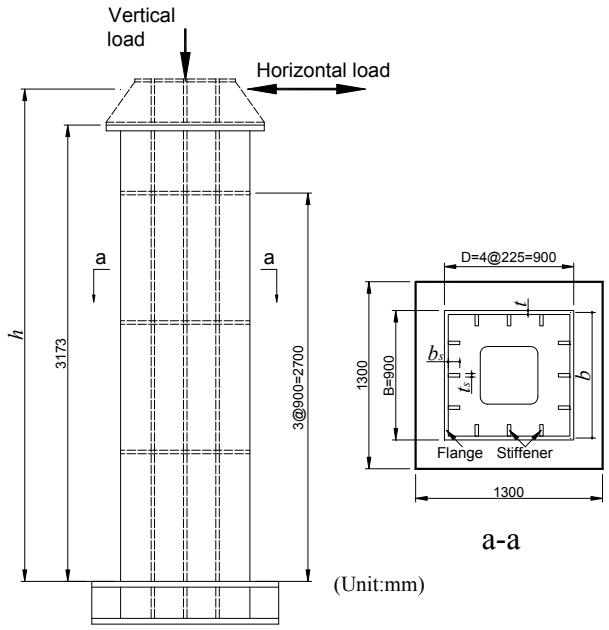

Figure 1. Test Specimen with Box Cross Section (Nishikawa et al. [10])

Table 1. Geometrical Parameters of Specimen

h(mm)	b(mm)	t(mm)	b_s(mm)	t_s(mm)	R_f	$\bar{\lambda}$	γ/γ^*	α	$\overline{\lambda_s}$	P/P_y
3403	891	9.1	80	6.2	0.56	0.26	0.89	1.0	0.63	0.122

Table 2. Material Properties of Specimen

σ_y (MPa)	E (GPa)	ν	E/E_{st}
379	206	0.3	100

In Table 1, the flange plate width-thickness ratio (R_f) and the column slenderness ratio parameter ($\bar{\lambda}$) are the two important parameters, which control the inelastic cyclic behavior of the steel box columns. The former parameter inhibits the local buckling of the flange plate, while the latter determines the global instability. They are given as,

$$R_f = \frac{b}{t}\sqrt{\frac{12(1-\nu^2)}{\pi^2 k}}\sqrt{\frac{\sigma_y}{E}} \tag{1}$$

$$\bar{\lambda} = \frac{2h}{r}\frac{1}{\pi}\sqrt{\frac{\sigma_y}{E}} \tag{2}$$

where, t is the plate thickness, b the flange plate width = B-t (B is the width of the cross section), σ_y the yield stress, ν the Poisson's ratio, E the Young's modulus, k the buckling coefficient of a stiffened plate = $4n^2$ (n is the number of subpanels in each stiffened plate), h the column height and r the radius of gyration of cross section.

The stiffener's slenderness ratio, $\bar{\lambda}_s$, affects the deformation capacity of stiffeners and local buckling mode. It can be given as (Ge et al. [2]),

$$\bar{\lambda}_s = \frac{1}{\sqrt{Q}}\frac{L_d}{r_s}\frac{1}{\pi}\sqrt{\frac{\sigma_y}{E}} \tag{3}$$

$$Q = \frac{1}{2R_f}(\beta - \sqrt{\beta^2 - 4R_f}) \le 1.0 \tag{4}$$

$$\beta = 1.33R_f + 0.868 \tag{5}$$

where L_d is the distance between two adjacent diaphragms, r_s the radius of gyration of T-shape cross-section centered on one longitudinal stiffener with its width of b/n; and Q the local buckling strength of a plate enclosed by two adjacent diaphragms and stiffeners. Moreover, in Table 1, γ is the relative flexural rigidity of one stiffener and γ^* is the optimum value of γ obtained from the linear buckling theory; α (=L_d/B) is the aspect ratio of the flange plate between two diaphragms; P/P_y is the magnitude of axial load; b_s the width of stiffener; and t_s the thickness of the stiffener.

2.2 Shell Element-based Model

During the 1995 Hyogoken-Nanbu earthquake, for such thin-walled steel columns, the local buckling occurred near the base of the columns. Therefore, as shown in Figure 2, the beam element is employed for the upper portion of the column, while the shell element, which can consider the effect of the local buckling, is used for the lower portion of the column. For the part of shell elements, the length from the base to the first diaphragm is divided into 9 segments and the subsequent same lengths are divided into 5 segments along the column length. The length and width of the cross section are divided into 12 segments, respectively. The longitudinal stiffener and

the diaphragm are also simulated with the shell elements. On the other hand, 10 beam elements are adopted to model the upper part of the column. Taking advantage of the symmetry of the geometry, the loading and the boundary of the specimen within the test plane, only half of the column is simulated. Besides, a stiff plate with infinite bending stiffness is assumed in the interface between the beam-element part and the shell-element part, where the third diaphragm is located.

In this simulation, both material and geometrical nonlinearities are considered. As shown in Figure 3(a), the bilinear elastic-plastic material model is employed to model the plastic deformation. As the name suggests this model used two lines to represent the stress-strain curve: the slope of the first line is the initial Young's modulus, E; and the slope of the second line is the post-yield modulus, E_{st}, which is set as $E/100$ in this study. Furthermore, the bilinear kinematic hardening is used as the hardening rule, as shown in Figure 3(b).

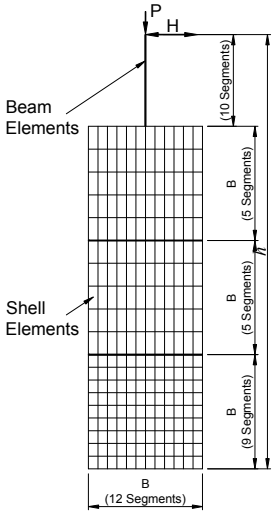

Figure 2. Analytical Model of Steel Box Bridge Pier

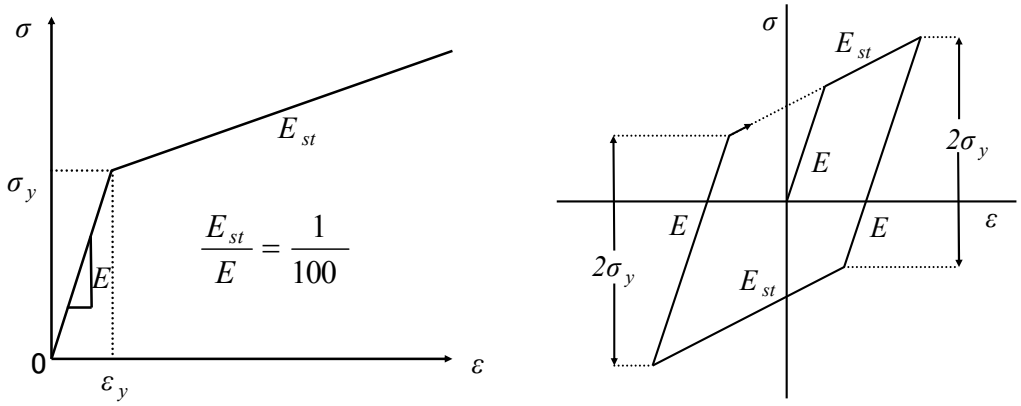

Figure 3. Stress-strain Behavior of Steel Material

2.3 Comparison between Simulation and Experiment

At the beginning of the test, a constant force, P, was applied on the top of the steel column. Subsequently, a cyclic loading pattern controlled by the imposed lateral displacement was used to conduct this experiment. As shown in Figure 4, the lateral displacement history consists of

sequence of full reversed displacement cycles and the peak displacements are increased stepwise with the increment, δ_y, after one cycle at each displacement level.

The lateral load versus lateral displacement hysteretic curve of the column obtained from the simulation is plotted with the test results (see Figure 5). After obtaining the load-displacement curve, the yield lateral load, H_y, and the yield lateral displacement, δ_y, will be employed to non-dimensionalize the curves. Here, H_y is taken as the smaller one from the following two equations (Usami et al. [11]),

$$H_y = \frac{M_y}{0.85h}\left(1-\frac{P}{P_E}\right)\left(1-\frac{P}{P_u}\right) \tag{6}$$

$$H_y = \frac{M_y}{h}\left(1-\frac{P}{P_y}\right) \tag{7}$$

where M_y is the yield moment of cross section, P_E the Euler's buckling loading of a cantilever column and P_u the ultimate strength of a centrally loaded column, which is determined from the following equation adopted in the Japanese specification for road bridges [12].

$$\frac{P_u}{P_y} = \begin{cases} 1.0 & (\bar{\lambda} \le 0.2) \\ 1.109 - 0.545\bar{\lambda} & (0.2 \le \bar{\lambda} \le 1.0) \\ 1/(0.773+\bar{\lambda}^2) & (\bar{\lambda} \ge 1.0) \end{cases} \tag{8}$$

The yield displacement, δ_y, is then calculated from the following equation neglecting transverse shear deformation:

$$\delta_y = \frac{H_y h^3}{3EI} \tag{9}$$

It can be seen that the strengths predicted by the shell element based model at each reversal point are quite close to the test results, that is to say, this model can excellently reflect the steel pier with the thin-walled stiffened box cross section. Therefore, this shell element based approach is used as the benchmark model to validate the proposed fiber-beam element based method in the following sections.

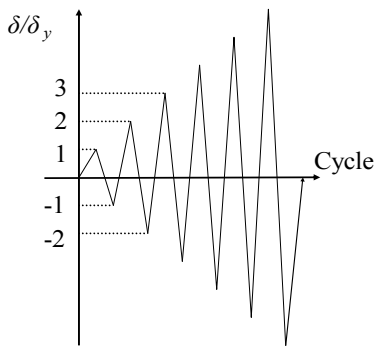

Figure 4. Lateral Displacement History

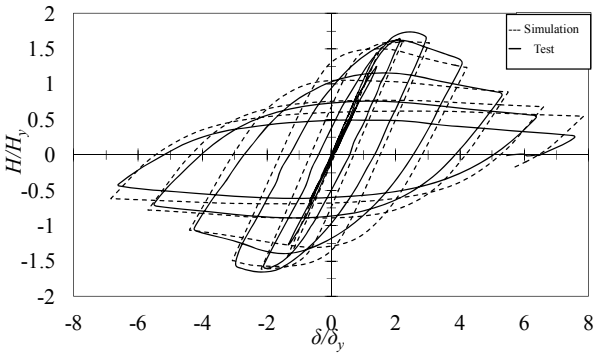

Figure 5. Comparison of Hysteretic Curves

2.4 Numerical Cases

In order to compare the shell element based model with the beam element based model (i.e., the fiber model), twelve numerical cases of the thin-walled stiffened box piers were analyzed. The main parameters considered are: flange plate width-thickness ratio R_f, column slenderness ratio $\bar{\lambda}$, stiffener's slenderness ratio $\bar{\lambda}_s$. The scope of these parameters are R_f=0.5~0.8, $\bar{\lambda}$=0.3~0.5 and $\bar{\lambda}_s$=0.534~0.935, respectively. Table 2 lists geometrical properties of numerical cases and Figure 6(a) plotted their cross sections. The material properties of these cases are σ_y=314MPa, E=206GPa and v=0.3. As shown in Figure 6(b), the same shell element based analysis method and loading pattern were employed in this simulation.

Figure 7 shows hysteretic curves of non-dimensionalized lateral load, H/H_y, versus lateral displacement, δ/δ_y. It can be concluded that both the strength and ductility slightly decrease with the increase in $\bar{\lambda}$. On the other hand, the maximum strength obviously decreases with the increase in R_f.

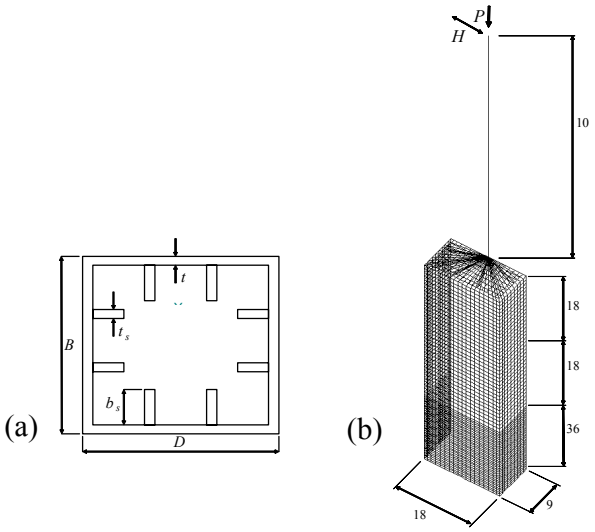

Figure 6. Shell Element Based Model of Numerical Cases

Table 3 Geometrical Dimensions and Parameters of Numerical Cases

No.	h (mm)	b (mm)	t (mm)	b_s (mm)	t_s (mm)	R_f	$\bar{\lambda}$	γ/γ^*	α	$\bar{\lambda}_s$	P/P_y	H_y (kN)	δ_y (mm)
S1	7025	1461	20	133	20	0.5	0.3	1.0	1.0	0.53	0.17	2242	30.2
S2	9366	1461	20	133	20	0.5	0.4	1.0	1.0	0.53	0.13	1760	53.4
S3	11708	1461	20	133	20	0.5	0.5	1.0	1.0	0.53	0.11	1449	83.9
S4	8463	1753	20	140	20	0.6	0.3	1.0	1.0	0.65	0.16	2506	34.5
S5	11284	1753	20	140	20	0.6	0.4	1.0	1.0	0.65	0.13	1967	61.1
S6	14105	1753	20	140	20	0.6	0.5	1.0	1.0	0.65	0.10	1619	96.0
S7	9901	2045	20	146	20	0.7	0.3	1.0	1.0	0.78	0.15	2721	38.1
S8	13201	2045	20	146	20	0.7	0.4	1.0	1.0	0.78	0.12	2136	67.5
S9	16501	2045	20	146	20	0.7	0.5	1.0	1.0	0.78	0.10	1759	106.1
S10	11338	2338	20	152	20	0.8	0.3	1.0	1.0	0.93	0.14	2890	41.0
S11	15118	2338	20	152	20	0.8	0.4	1.0	1.0	0.93	0.11	2269	72.7
S12	18897	2338	20	152	20	0.8	0.5	1.0	1.0	0.93	0.09	1869	114.2

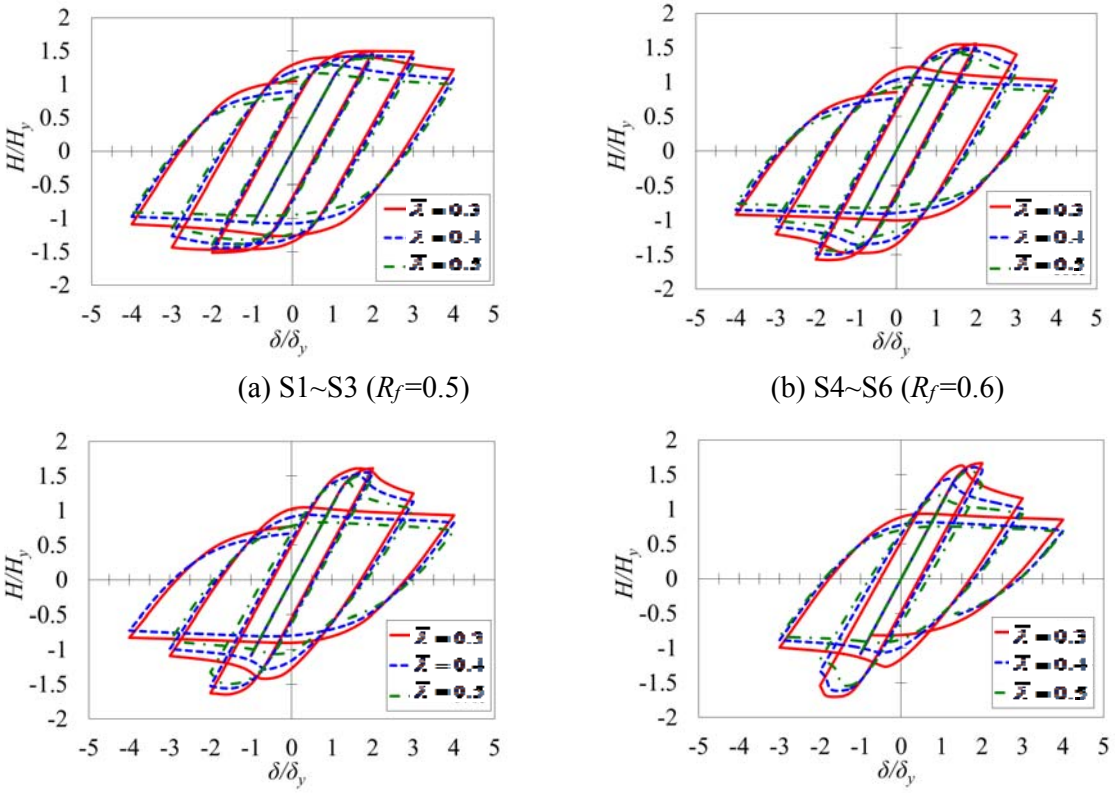

(a) S1~S3 (R_f=0.5) (b) S4~S6 (R_f=0.6)

(c) S7~S9 (R_f=0.7) (d) S10~S12 (R_f=0.8)

Figure 7. Lateral Load versus Lateral Displacement Curves

3. SIMPLIFIED SEISMIC EVALUATION METHOD

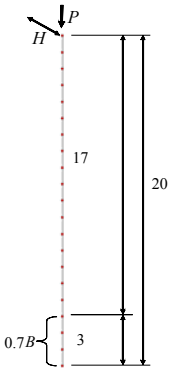

Figure 8. Beam Element Based Model

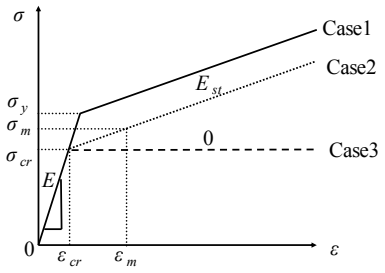

Figure 9. Modified Stress-strain Relationship

The pushover analysis method based on the fiber-beam element is proposed to evaluate the hysteretic behavior of the thin-walled stiffened box piers. As shown in Figure 8, this model has 20 elements and the part with the height of 0.7*B* from the base, where the local buckling occurred, was divided by 3. As mentioned above, the effect of the local buckling cannot be considered in the beam element. Therefore, further modification of the bilinear material model is suggested.

As shown in Figure 9, two additional stress-strain relationships are given. Case 1 is a bilinear stress-strain relationship employed in the previous shell element based simulation. In case 2, the yield stress, σ_y, was replaced by the buckling stress, σ_{cr} [12], which can be determined by,

$$\frac{\sigma_{cr}}{\sigma_y}=\begin{cases}1.5-R_f & (R_f>0.5)\\ 1 & (R_f\le 0.5)\end{cases} \tag{10}$$

Because of the same initial Young's modulus, the buckling strain, ε_{cr}, can be calculated from σ_{cr}/E. Furthermore, the post-yield modulus, E_{st}, can be given by,

$$E_{st}=\frac{\sigma_m-\sigma_{cr}}{\varepsilon_m-\varepsilon_{cr}} \tag{11}$$

where σ_m and ε_m are the local buckling stress and strain, respectively. The local buckling stress, σ_m, can be obtained from the following empirical formula [1],

$$\frac{\sigma_m}{\sigma_y}=1.24-0.54R_f\le 1.0 \tag{12}$$

and the local buckling strain, ε_m, is defined in this study as,

$$\varepsilon_m=2\cdot\frac{\sigma_{cr}}{\sigma_y}\cdot\varepsilon_y \tag{13}$$

According to the above-mentioned equations, the material parameters of Case 2 for the different R_f are listed in Table 4. It should be noted that in the case of R_f=0.5, calculated value from Eq. 12 is σ_m = 304.58 < σ_y =314 MPa. In such a case, it is assumed to be the same as Case 1. Moreover, In Case 3, after the buckling stress point, it yields under the constant stress.

Table 4. Material Parameters of Case 2

R_f	σ_{cr}(MPa)	ε_{cr}($\times10^{-3}$)	σ_m(MPa)	ε_m($\times10^{-3}$)	E/E_{st}
0.5	314	1.52	—	—	100
0.6	282.6	1.37	287.6	2.74	56.25
0.7	251.2	1.22	270.7	2.44	12.90
0.8	219.8	1.07	253.7	2.13	6.48

4. NUMERICAL COMPARISON

As described before, three bilinear stress-strain relationships were employed for the fiber-beam elements in the pushover analysis method. Figure 10 compared the horizontal force versus the horizontal displacement relationships of some numerical cases. The yield lateral load, H_y, and the yield lateral displacement, δ_y, were employed to make these curves dimensionless. Besides, the skeletons of the hysteretic relationships of the shell element-based simulation were given together. It can be seen that, from Case 1 to Case 2 and then to Case 3, the force-displacement curve moved downward.

The ultimate points were assumed as the maximum strength and 95 percent of the maximum strength after the peak, respectively. Moreover, the authors suggested Eqs. 14 and 15 for calculating the ultimate compression strain ε_m (strain corresponding to the maximum bending moment M_{max}) and ε_u (strain corresponding to 95%M_{max} after peak) achieved by the simulation of the stiffened box section under the compression and bending (Zheng et al. [13]).

$$\frac{\varepsilon_m}{\varepsilon_y} = \frac{1.41}{\left(R_f \overline{\lambda}_s^{0.18} - 0.21\right)^{0.462}} + 0.38 \le 20.0 \tag{14}$$

$$\frac{\varepsilon_u}{\varepsilon_y} = \frac{0.7}{\left(R_f \overline{\lambda}_s^{0.18} - 0.18\right)^{1.3}\left(1 + P/P_y\right)^{2.2}} + \frac{3.2}{\left(1 + P/P_y\right)} \le 20.0 \tag{15}$$

$$\left(0.3 \le R_f \le 0.8,\ \ \gamma/\gamma^* \ge 1.0,\ \ 0.0 \le P/P_y \le 0.5\right)$$

The average strain of the outmost brink center of the three elements at the base, located on the effective failure length, is defined as ε_{avg}. When ε_{avg} reaches ε_m and ε_u, the corresponding displacements are defined as the ultimate displacements, δ_m and δ_u, respectively. In terms of the force-displacement curve, the corresponding forces are defined as the ultimate strengths, H_m and H_u, respectively. The required ultimate points (δ_m, H_m) and (δ_u, H_u) are shown in Figure 10. The comparisons of the ultimate points between the fiber-beam based model and the shell based model are shown in Figures 11 and 12.

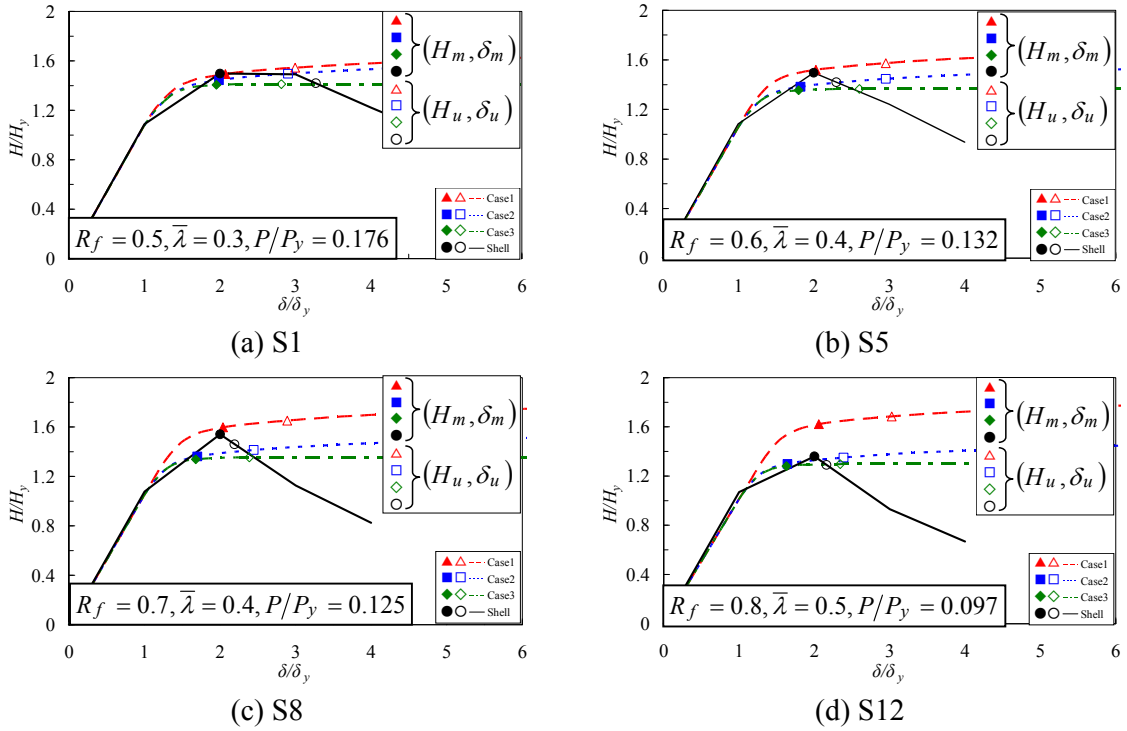

(a) S1 (b) S5

(c) S8 (d) S12

Figure 10. Comparison of Ultimate Values

Figures 11(a), 11(c) and 11(e) compare H_m. When Case 1 is used as the fiber-beam's material model, the deviations of eleven cases are below 10%, but the results of the fiber-beam based model are relatively larger than those of the shell based model (in the dangerous side). When Case 2 is employed, the deviations of all cases are below 20% and the results of the fiber-beam based model are in the safe side. Furthermore, Case 3 seems safe in comparison with Case 2, but the deviations of two cases are over 20%. Figures 11(b), 11(d) and 11(f) compare δ_m. The deviations of twelve cases employing Case 1 are all below 10%. On the other hand, although the deviations exceed 20% for the cases using either Case 2 or Case 3, both are confirmed safe.

Figures 12(a), 12(c) and 12(e) compare H_u. When Case 1 is used, the deviation of one case exceeds 20% and the others approach the 10% line, but the results of the fiber-beam based model are

relatively large and locate in the dangerous side. When Case 2 is used, the deviations of all the cases are below 20% and the results are slightly large. When Case 3 is used, although the deviations of the two models exceed 20%, the results are in the safe side. Figures 12(b), 12(d) and 12(f) compare δ_u. When Case 1 is used, the deviations of six models exceed 20% and the results are relatively large. When Case 2 is used, the estimation accuracy was improved and the deviations were below 20% for all models. The accuracy of estimation is further improved for Case 3.

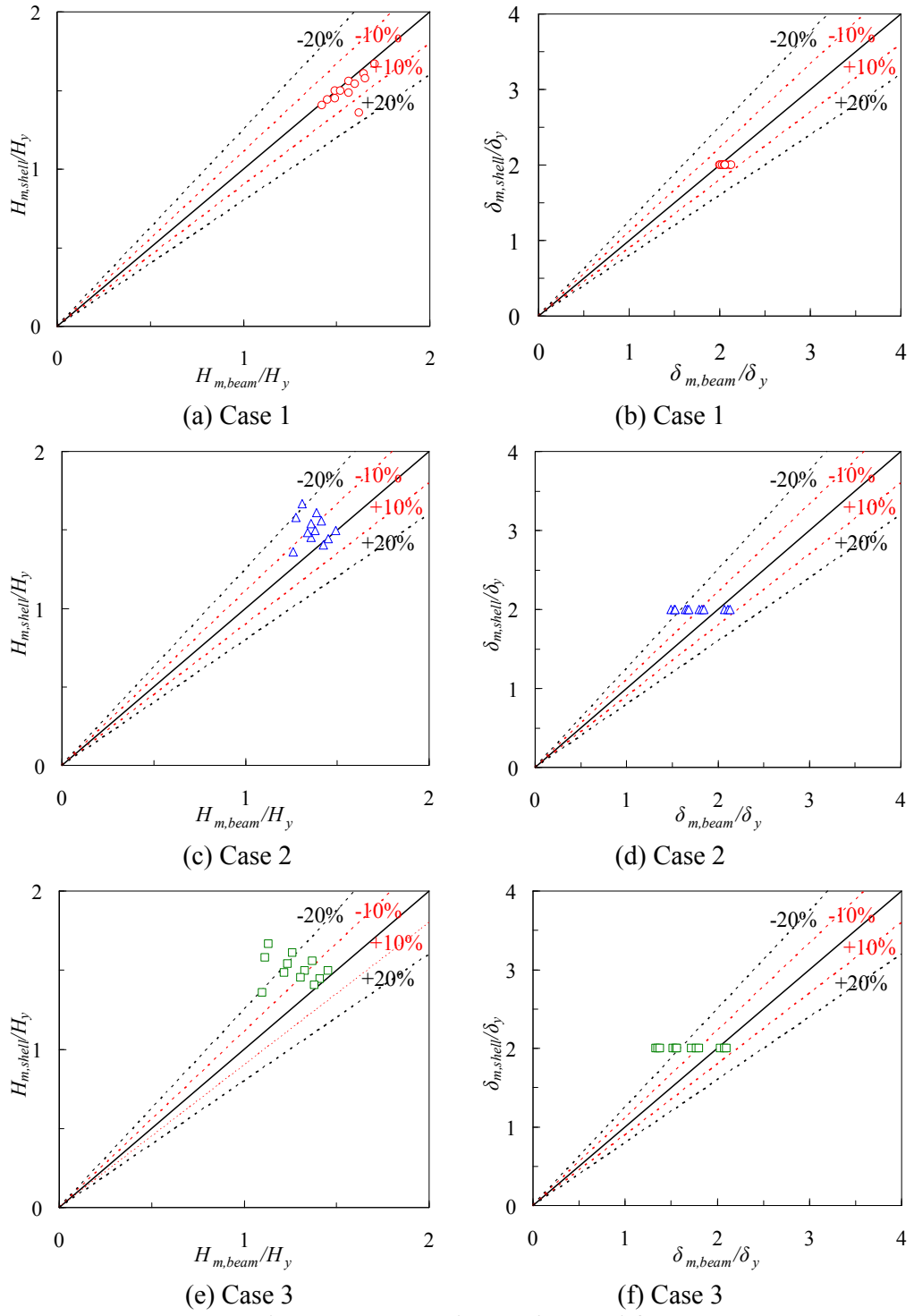

(a) Case 1 (b) Case 1

(c) Case 2 (d) Case 2

(e) Case 3 (f) Case 3

Figure 11. Comparisons of H_m and δ_m

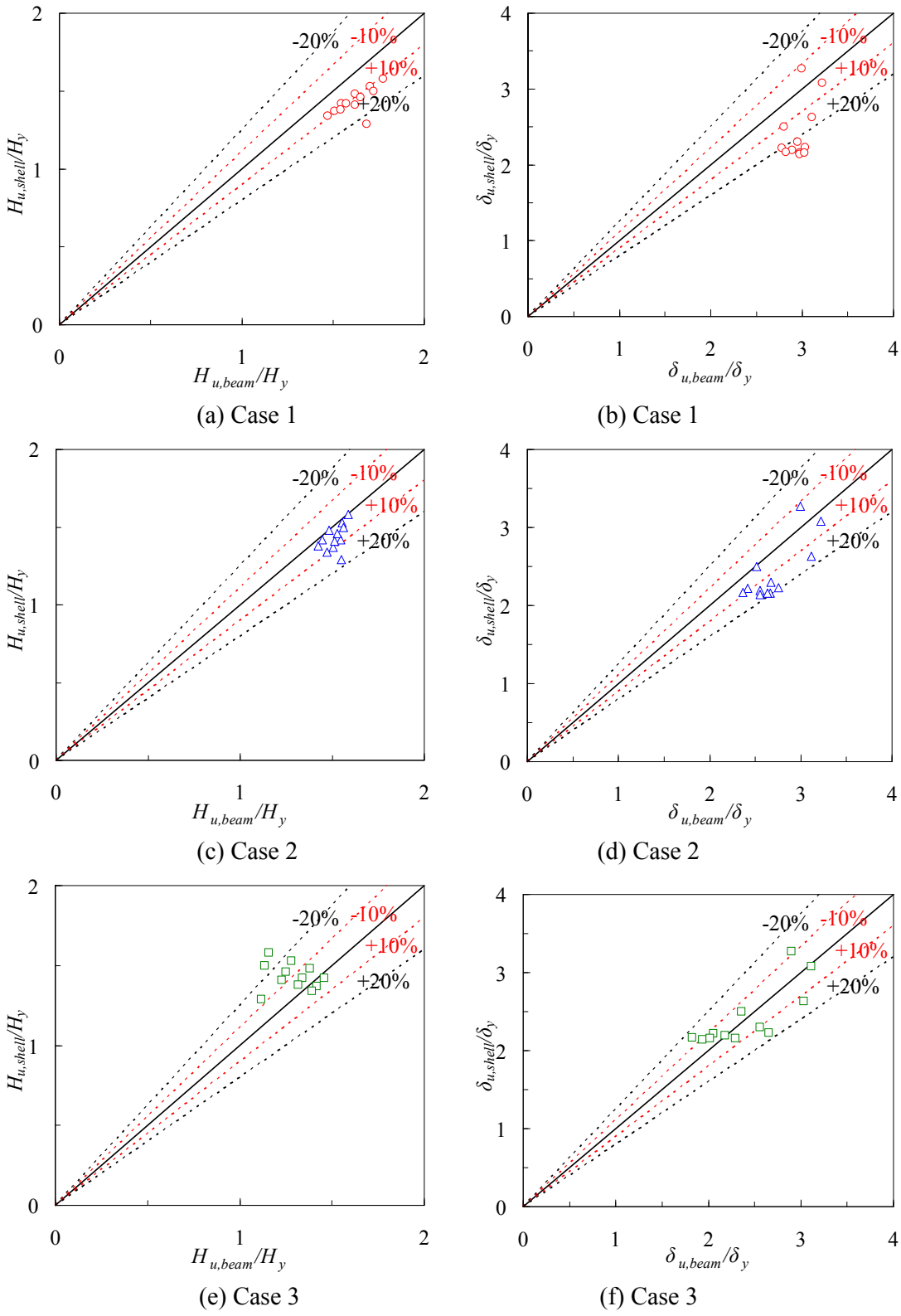

(a) Case 1 (b) Case 1

(c) Case 2 (d) Case 2

(e) Case 3 (f) Case 3

Figure 12. Comparisons of H_u and δ_u

From Figures 11 and 12, the results achieved by using Case 2 are optimal when the maximum strength is taken as the ultimate point. On the other hand, the results achieved by using Case 3 are optimal when the 95% of the maximum strength after peak is regarded as the ultimate point.

5. CONCLUSIONS

The conclusions of this study can be given: (1) it's confirmed that the shell element based model employing the bilinear kinematic hardening relation can effectively reflect the thin-walled stiffened box steel piers; (2) Strength and ductility of thin-walled stiffened box sectional steel bridge piers can be accurately predicted using the proposed pushover method based on the fiber-beam element. it is advised to adopt the modified bilinear material model (Case 2), in which the yield point is replaced by the buckling stress, when the maximum strength is taken as the ultimate point; and (3) in addition, it is advised to adopt the elastic-perfectly plastic material model (Case 3) when the 95% of the maximum strength after the peak is regarded as the ultimate point in the proposed method.

ACKNOWLEDGEMENTS

The study was supported by Science and Technology Research Project of Ministry of Transport, PRC (No.2011 318 775 680) and the Transportation Foundation of Henan Province, PRC (No.2011GF11).

REFERENCES

[1] Usami, T. and Ge, H.B., "Cyclic Behavior of Thin-Walled Steel Structures - Numerical Analysis", Thin-Walled Structures, 1998, Vol. 32, pp. 41-80.

[2] Ge, H.B., Gao, S. and Usami, T. "Stiffened Steel Box Columns. Part 1: Cyclic Behavior", Earthquake Engineering and Structural Dynamics, 2000, Vol. 29, No. 11, pp. 1691-1706.

[3] Usami, T., Gao, S. and Ge, H.B., "Stiffened Steel Box Columns. Part 2: Ductility Evaluation", Earthquake Engineering and Structural Dynamics, 2000, Vol. 29, No. 11, pp. 1707-1722.

[4] Susantha, K.A.S., Aoki, T., Kumano, T., Yamamoto, K., "Applicability of Low-yield-strength Steel for Ductility Improvement of Steel Bridge Piers", Engineering Structures, 2005, Vol. 27, No. 7, pp. 1064-1073.

[5] Galambos, T.V., "Guide to Stability Design Criteria for Metal Structures (5th edn)", Wiley, 1998.

[6] Gao, S., Usami, T. and Ge, H.B., "Ductility evaluation of steel bridge piers with pipe-sections", Journal of Engineering Mechanics, ASCE, 1998, Vol.124, No.3, pp.260-267.

[7] Goto, Y., Wang, Q. and Obata, M., "FEM Analysis for Hysteretic Behavior of Thin-Walled Steel Columns", Journal of Structural Engineering, ASCE, 1998, Vol. 124, No. 11, pp. 1290-1301.

[8] Sakimoto, T., Watanabe, H. and Nakashima, K., "Hysteretic Models of Steel Box Members with Local Buckling Damage", Journal of Structural Mechanics and Earthquake Engineering, JSCE, 2000, Vol. 647, No. I-51, pp. 343-355. (in Japanese)

[9] Ozawa K., Wang Q. and Goto Y., "A Pushover Analysis of Steel Piers Based on a Beam Element with a Softening Constitutive Relation Considering the Localization of Buckling Patterns in Stiffened Plate Components", Journal of Structural Mechanics and Earthquake Engineering, JSCE, 2001, Vol. 689, No. I-57, pp. 225-237. (in Japanese)

[10] Nishikawa, K., Yamamoto, S., Natori T., Terao, O., Yasunami, H. and Terada, M., "An Experimental Study on Improvement of Seismic Performance of Existing Steel Bridge Piers", Journal of Structural Engineering, JSCE, 1996, Vol. 42A, pp. 975-986.

[11] Usami, T., Mizutani, S., Aoki, T. and Itoh, Y., “Steel and Concrete-filled Steel Compression Members under Cyclic Loading.” In: “Stability and Ductility of Steel Structures under Cyclic Loading.” CRC Press, 1992, pp. 123-138.

[12] JRA, “Specifications for Highway Bridges, Part I: Common and Part II: Steel Bridges”, Japan Road Association, Tokyo, Japan, 2012. (in Japanese)

[13] Zheng, Y., Usami, T. and Ge, H.B., “A Seismic Design Methology for Thin-Walled Steel Structures through the Pushover Analysis.” NUCE Research Report, No.2000-01, Nagoya University, 2000.

FLEXURAL BEHAVIOR OF LIGHTWEIGHT AGGREGATE CONCRETE FILLED STEEL TUBE

Fu Zhongqiu, Ji Bohai*, Maeno Hirofumi, Eizien A. and Chen Jiashu

College of Civil and Transportation Engineering, Hohai University, Nanjing 210098, China
**(Corresponding author: E-mail: hhbhji@163.com)*

Received: 28 September 2012; Revised: 24 March 2013; Accepted: 18 October 2013

ABSTRACT: To study the flexural behaviour of lightweight aggregate concrete filled steel tubes (LACFST), 21 LACFST specimens and 8 steel tubes without filling concrete were tested under pure bending load. The parameters considered are: steel tube diameter and thickness, lightweight aggregate concrete (LAC) strength and shear span ratio. According to the test results, the failure mode, deflection and failure process were studied and their influence on the flexural behaviour of LACFST was analyzed. Several codes were used to calculate the stiffness and moment capacity. Based on the mechanical equilibrium and combined strength, two methods were provided to calculate the moment capacity in this paper. The calculated results were verified with the test ones. The constitutive model of confined LAC in compressive region was also proposed and used in the FEM to analyze the flexural behaviour of LACFST. This study showed the strain distribution agreed with the Bernoulli-Euler's theory. The deflection along the length distributed as half sine wave curve during the test. The moment capacity of LACFST increased as the steel ratio and LAC strength increased. But the shear span ratio had almost no influence on the flexural behaviour of LACFST. The comparison between the calculation and the test showed the results of AIJ (1997) for stiffness and DL/T5085 for moment capacity fitted with the test ones well. But the results using the two proposed methods had a better accuracy to calculate the moment capacity. The FEM analysis showed the constitutive model of confined LAC in compressive region was also proved having a good accuracy.

Keywords: Lightweight aggregate concrete filled steel tube, flexural behaviour, stiffness, moment capacity, calculation method

1. INTRODUCTION

Recently concrete filled steel tube (CFST) has wide applications in structures because of its high bearing capacity, lightweight, small cross section, good seismic performance and so on [1-4]. Under compressive loading, steel casing in CFST provides potential confinement to the concrete core which boosts the capacity and ductility of the concrete. Also concrete core can delay steel tube local buckling appearance. Therefore, CFST is always used as compression members. But because of the high bearing capacity and small cross-sectional area, it is application as a beam structure has advantages too.

Many researchers have focused their studies on the behavior of CFST at the practical application [5-7]. Therefore, a flexural performance of CFST needs to be studied more deep theoretically [8-10]. In fact, CFST has already been used as flexural member of bridges, such as the composite beam of Shinkansen bridge in Japan [11]. In China, there are 5 CFST space truss beam bridges already which are Zidong Bridge in Guangdong, Xiangjiaba Bridge in Hubei, Wanzhou Bridge in Chongqing, Wan`ang Bridge in Chongqing, Ganhaizi Bridge in Sichuan.

According to the beam, especially the large span ones, their self-weight has a significant impact on their structural behavior. Thus, as the lightweight aggregate concrete has lighter weight than the normal concrete it may replace the second one to fill the steel tubes. Previous researches [12-13] show that LACFST has excellent mechanical performance which is similar to that of CFST. Also, they confirmed that LACFST can be used in structures instead of CFST. In addition, if LACFST applied in beams, the height of the beam section and the cost of the basis will obviously reduced.

In 2003, Assi IM studied 34 square and rectangular steel tubes (1000mm length) filled with foamed and lightweight aggregate concrete experimentally to evaluate the ultimate moment of these beams [14]. But till now, there is a few researches concern the flexural performance of LACFST beams. Although, there are some flexural performance conclusions about normal CFST, it is not decided yet whether these conclusions are applicable to LACFST or not till now. Thus, there is a need for more studies in this concern. Based on the previous studies carried by the authors [15-16] on the compressive performance of LACFST, the behavior of circular LACFST under pure bending was studied.

2. EXPERIMENTAL INVESTIGATIONS

2.1 Material

The coarse aggregate of lightweight aggregate concrete is haydite. The bulk density is 814 kg/m^3, the cylindrical compressive strength is 8.5MPa, and the ratio of water absorption ratio is 6% an hour. Ordinary Portland cement was used for the concrete. According to the relevant Chinese standards, compression tests were carried out on a number of standard cubes ([150×150×150] mm) to determine the concrete grade and prisms [150×150×300] mm in order to determine the compressive strength (f_{ck}) and elastic modulus (E_c) of the unconfined concrete. The cubes and prisms were cured at room temperature. The concrete mix proportion and mechanical properties are given in Table 1 and Table 2 respectively.

Table 1. Mixture Mass per Cubic Meter LAC Concrete (kg)

Item	Cement	Haydite	Sand	Water	Mineral powder	Water reducer
Mix 1	460	670	650	170	0	0
Mix 2	450	650	650	125	50	3

Table 2. Mechanical Properties of LAC Concrete

Item	Cubic strength 28d f_{cu} (MPa)	Cubic strength 105d f_{cu} (MPa)	Prism strength 105d f_{ck} (MPa)	Elastic Modulus E_c (GPa)	Bulk density (kg/m^3)
Mix 1	44.8	49.9	31.3	24.0	1810
Mix 2	53.6	59.2	41.2	26.8	1910

Straight welded steel tube Q235 was used in the test. A group of three standard specimens tested to determine the tensile strength of the steel where the thickness of each section of steel tube made into the interception of the standard specimen. The test method followed the regulations of Chinese standard "Metallic materials at ambient temperature tensile test method" (GB/T228-2002) (2002). The data was collected by TS3890 pseudo-dynamic strain instrument during the test process. The stress and strain relationship of specimen is shown in Figure 1. The Yield strength is 298.5 MPa and 274.7MPa for the steel with 2.5mm thickness and 3.8mm thickness respectively. The yield strain can be taken as $\varepsilon = 2000\times10^{-6}$ from Figure 1.

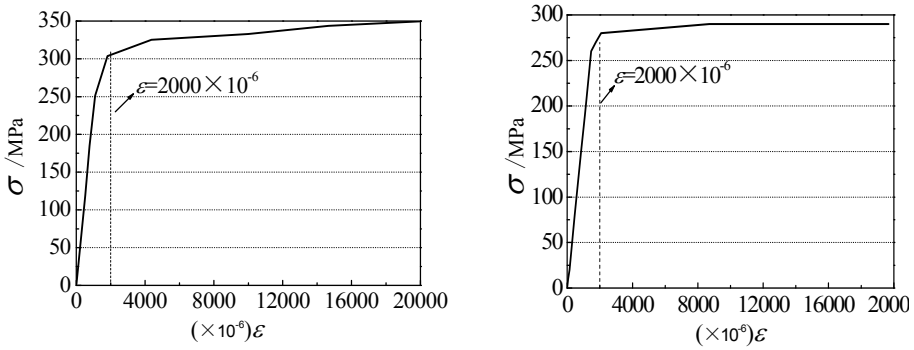

(a) t=2.5mm (b) t=3.8mm

Figure 1. Stress versus Strain Curve of Steel

2.2 Specimen

In this study, 21 LACFST specimens and 8 steel tube specimens without filling concrete were tested. Two types of steel tube used with diameters of 114mm and 165mm. The total length L of steel tube was 1400mm and 1700mm with effective span L_o =1200mm and 1500mm respectively. The two ends of the steel tube were flatted then, before concrete pouring, a circular plate with 8mm thickness welded on one end of each tube. During concrete pouring, the angle between the steel tube and the ground was larger than 70°. Then, a concrete shaking table used to vibrate it and to ensure its density. Two weeks later, surface hollows due to shrinkage filled up with grout to confirm the specimen side smoothness. To observe the slip between the steel tube and LAC, two identical circular plates welded on both ends of some of the test specimens, while the rest of the specimens welded on one end only. The specimens cured by natural conditions. The details of the test specimens are shown in Table 3.

Table 3. Details of the Test Specimens

Specimens	Pipe size (mm)			L_o (mm)	L_a (mm)	λ	α	f_y (MPa)	f_{ck} (MPa)	M_u (kN • m)
	D	t	L							
CS114-2.5-30-A	114	2.5	1400	1200	300	2.6				11.47
CS114-2.5-30-B	114	2.5	1400	1200	300	2.6	0.09	298.5	31.3	11.75
CS114-2.5-30-C	114	2.5	1400	1200	300	2.6				12.02
CS114-2.5-50-A	114	2.5	1400	1200	300	2.6				13.17
CS114-2.5-50-B	114	2.5	1400	1200	300	2.6	0.09	298.5	41.2	11.94
CS114-2.5-50-C	114	2.5	1400	1200	300	2.6				12.3
CS114-3.8-30-A	114	3.8	1400	1200	300	2.6				14.72
CS114-3.8-30-B	114	3.8	1400	1200	300	2.6	0.14	274.7	31.3	15.88
CS114-3.8-30-C	114	3.8	1400	1200	300	2.6				15.08
CS114-3.8-50-A	114	3.8	1400	1200	300	2.6				17.56
CS114-3.8-50-B	114	3.8	1400	1200	300	2.6	0.14	274.7	41.2	16.13
CS114-3.8-50-C	114	3.8	1400	1200	300	2.6				16.56
CS165-2.5-30-A	165	2.5	1400	1200	300	1.8				20.72
CS165-2.5-30-B	165	2.5	1400	1200	400	2.4	0.06	298.5	31.3	22.96
CS165-2.5-30-C	165	2.5	1700	1500	500	3.0				21.48
CS165-3.8-30-A	165	3.8	1400	1200	300	1.8				37.81

CS165-3.8-30-B	165	3.8	1400	1200	400	2.4	0.09	274.7	31.3	36.93
CS165-3.8-30-C	165	3.8	1700	1500	500	3.0				37.9
CS165-3.8-50-A	165	3.8	1400	1200	300	1.8				37.8
CS165-3.8-50-B	165	3.8	1400	1200	400	2.4	0.09	274.7	41.2	40.08
CS165-3.8-50-C	165	3.8	1700	1500	500	3.0				38.7
ST114-2.5-A	114	2.5	1400	1200	300			298.5		9.73
ST114-2.5-B	114	2.5	1400	1200	300					9.78
ST114-3.8-A	114	2.5	1400	1200	300			274.7		12.57
ST114-3.8-B	114	3.8	1400	1200	300					12.48
ST165-2.5-A	165	2.5	1400	1200	300			298.5		16.38
ST165-2.5-B	165	2.5	1400	1200	300					16.00
ST165-3.8-A	165	3.8	1400	1200	300			274.7		31.45
ST168-3.8-B	165	38	1400	1200	300					30.64

Note: 1. D is the external diameter, t is the thickness, L, L_o, L_a stand for the length in Figure 2;
2. f_y is the yield strength of steel, f_{ck} is the prism strength at 105d;
3. α is steel ratio, $\alpha=A_s/A_c$, here A_s is the area of steel, A_c is the area of concrete;
4. λ is the shear span ratio, $\lambda=L_a/D$;
5. M_u is test ultimate moment corresponding to the load when the steel strain is 0.01.

2.3 Test Instruments and Procedure

This experiment performed in the structural engineering laboratory of Hohai University. The details of the test instruments sketched in Figure 2. The load applied on a rigid beam by a hydraulic jack and measured by a pressure sensor. A four-point bending rig used to apply the moment (see Figure 2a). 4 groups and 8 groups of strain gauges set at midspan of each specimen and spread eventually through the beam diameter (114mm and 165mm) respectively. Each group had a longitudinal strain gauge and a hoop strain gauge. There were 5 displacement transducers set to measure the deflection along the span, 3 of them set at one–quarter point and 2 of them set at the supports positions.

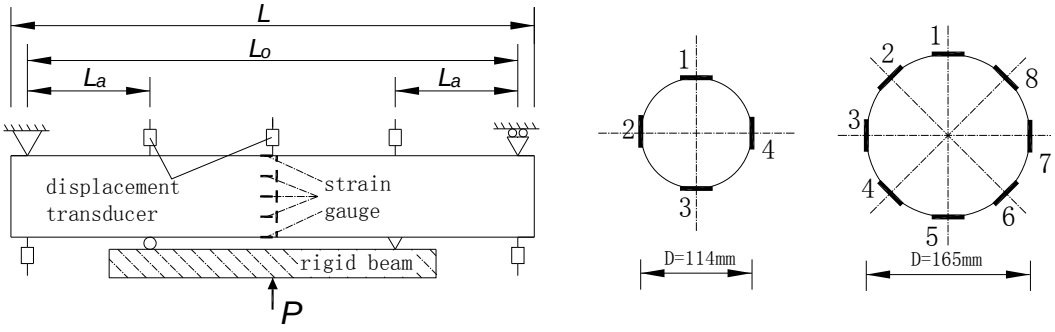

(a) Loading installations (b) Distribution of strain gauges

Figure 2. Loading and Measurement System

The specimens loaded at rate of 1/10 and 1/15 of the predicted ultimate load in the elastic phase and in the yielding phase respectively. Each load maintained about 2-3 minutes to enable the full deformation development. When approaching the predicted ultimate load, the load added slowly. All the gauges used in this experiment connected to a computer data acquisition system to record their values in the whole test phases (See Figure 3).

Figure 3. General View of the Test Setup

Figure 4. Specimen Failure Modes

3. EXPERIMENTAL RESULTS

3.1 Failure Mode

Figure 4 shows typical failure modes of LACFST beam. Although, most specimens failed without local buckling but a few of the specimens show unobvious local bucking at the rigid beam supports due to stress concentration caused by supports. Specimens welded on one end only show no slip between steel tube and LAC core. The cracked concrete took the shape of the deformed steel section. Besides, the cracks penetrated the whole section from tension area to compression area and spread evenly as was noticed after removing the steel wall as can be seen in Figure 4. This proved the section acted as a composite one, and the concrete confined by the steel tube. For the steel tube without filling, all specimens failed due to local buckling at the supports locations and mid-span.

3.2 Deflection of Specimen

Figure 5 shows a typically measured bending moment versus deflection curves of a group of specimens. From these curves noticed the defection increased slowly as the moment increased before the steel tube reach to the yield strain where, it is almost a straight line. After the steel tube yielding, the deflection increased rapidly. Moreover, all the curves showed no downward tendency when the test was stopped.

Figure 6 shows deflection curve along one of a typical tested specimen length under flexure. From this figure it is observed the curves are not symmetrical at the beginning of the test because of the discontinuity of materials. As the load increased, specimen deflection increased and distributed symmetrically due to stress redistribution between the concrete core and steel tube. Also it seemed the deflection curves coincided with half sine wave curves. And this had been improved in Figure 7 which showed the moment versus curvature curves of some specimens.

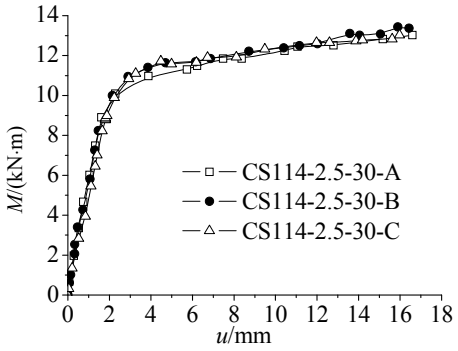

Figure 5. Moment Versus Deflection Curves

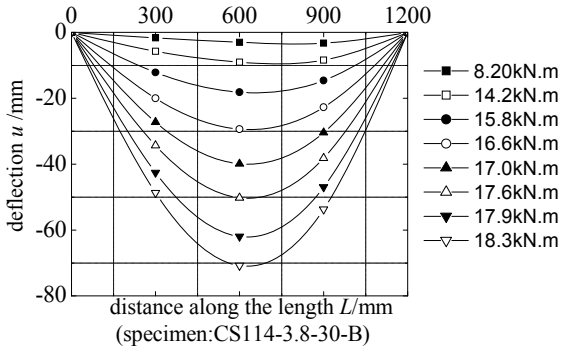

Figure 6. Deflection Distribution along the Length

For the flexural member, the curvature can be calculated with deflection and moment. And if the equation of deflection curve is known, it also can be calculated with the strain. Figure 7 displays the curves calculated by the two methods mentioned above. All the deflection and strain data were gained from the test. One of the curves was calculated by strain which was supposed that the deflection distributed as half sine wave curves. From the figures, it is possible to notice the clear convergence between the curves. So, it can be stated the deflection curve along the specimen length coincide with a half sine wave curve.

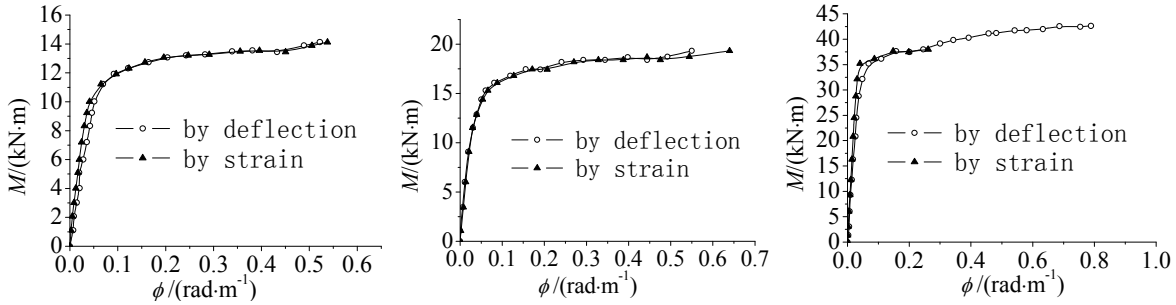

(a) CS114-2.5-50-A (c) CS114-3.8-50-A (e) CS165-3.8-30-B

Figure 7. Moment Versus Curvature Curves

3.3 Failure Process

Figure 8 shows the typical curves of moment versus steel longitudinal strain at the tension zone. All the curves of strain and deflection show there has no downward phase. So, the moment corresponding to the maximum fiber strain of 0.01 was defined as the moment capacity (M_u) of the specimen in this paper (refer to Figure 8) where its values listed in Table 3.

Figure 9 shows steel tube strain. At the beginning of the test, the axis of symmetry considered as the neutral axis of the section. Accordingly, strain 3 had almost no value before the tension side strain (strain 1) reach to yield strain (Strain numbers refer to the positions sketched in Figure 2(b)). All strains increased slowly in accordance to the moment increasing. After yield strain of tension side was reached, all strains increased rapidly. The neutral axis of the section moved, and the symmetry axis positioned in the original tensile zone thus, strain 3 increased as a tension strain.

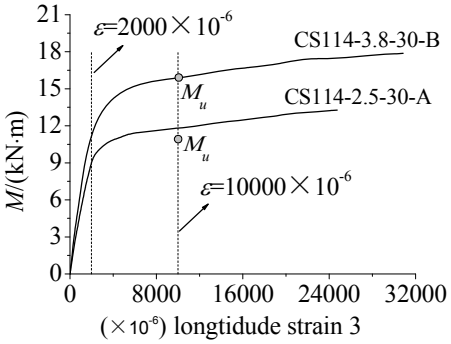

Figure 8. Demonstration of Moment Capacity

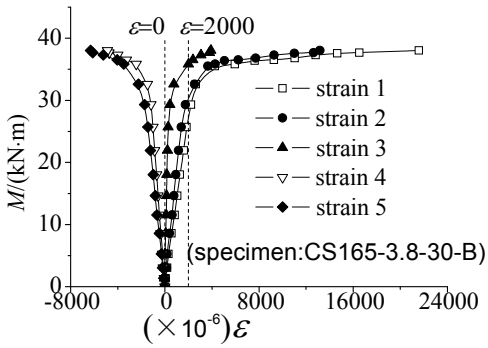

Figure 9. Longitudinal Strain of Steel Tube

Figure 10 describes the distribution curves of the longitudinal strains along the beam height. From the Figure it is noticed the section deformation of specimen's agree with the Bernoulli-Euler's theory at various loading stages. Neutral axis movement pointed out by the change of intersection point between connection line and symmetry axis.

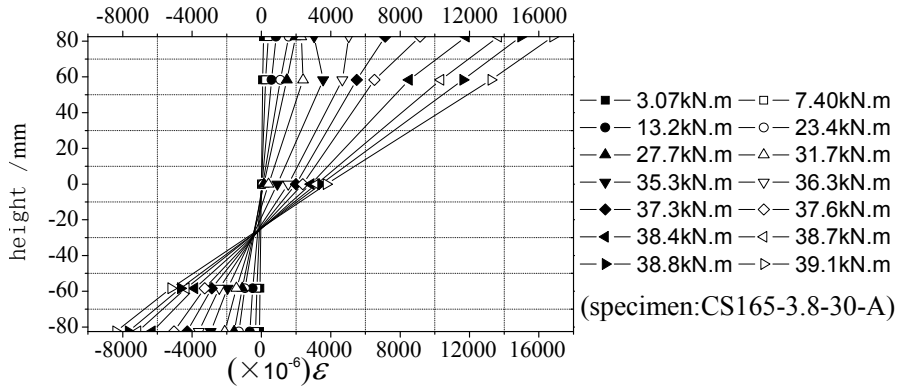

Figure 10. Distribution Curves of the Longitudinal Strain along the Beam Height

4. BEARING CAPACITY ANALYSIS

4.1 Influencing Factor

Figure 11(a) presents the moment - curvature curves of a specimen with different steel ratios. From the figure, it can be seen the initial stiffness of the specimen and the moment capacity increased as the steel ratio enlarged. In this test, specimens with t=3.8mm showed almost 30% moment capacity higher than the ones with t=2.5mm. As the steel has a higher bearing capacity; higher steel ratio will lead to more effective restrain to the concrete core. So, the higher steel ratio is the larger moment capacity and initial stiffness obtained.

From Figure 11(b) it is observed that specimen with higher LAC strength has a larger moment capacity. But, as it is known the moment mainly resisted by the steel tube, therefore; moment capacity increment was unobvious in compare with LAC strength improvement. Figure 11(c) shows the flexural behavior of LACFST and steel tube without concrete filling. From the figure it can be stated that LACFST has a better ductility and bearing capacity than the steel tube without concrete filling. Also, it can be concluded that filling steel tube with LAC can improve its flexural behavior well.

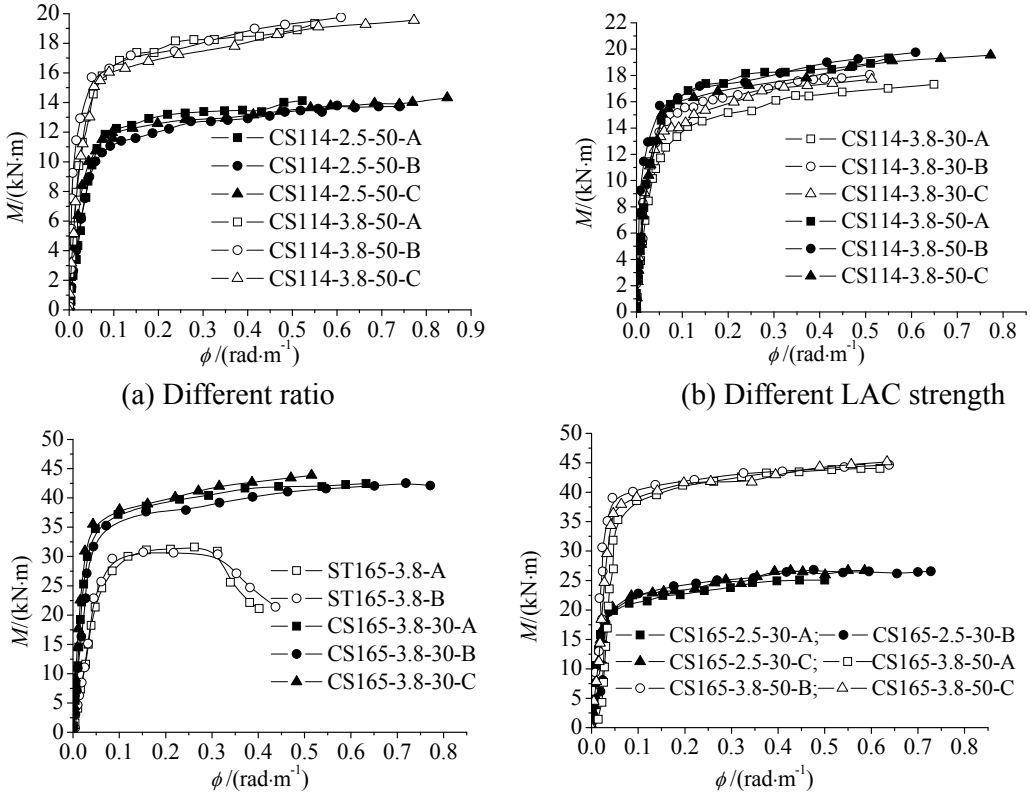

(a) Different ratio (b) Different LAC strength

(c) Comparison with steel tube (d) Different shear span ratio

Figure 11. Moment Versus Curvature Curves with Different Influencing Factor

Figure 11(d) displays the moment-curvature curves of specimens with different shear span ratio. From the figure it is possible to say the shear span ratio has almost no influence on the flexural behavior of LACFST.

4.2 Stiffness Calculation from the Codes

The stiffness of LACFST is a contribution of steel tube and LAC and not only the superposition of the two materials. When the specimen was flexural, the concrete would crack. The concrete could not provide enough stiffness to the composite beam and concrete core contribution to stiffness was reduced. A comparison between calculation formulas from different design codes carried out to study the stiffness of CFST, including AIJ (1997) [17], BS 5400 (1979) [18], EC4(1994) [19], AISC-LRFD (1999)[20] and DBJ13-15(2003)[21]. It was found that all the formulas can be described by expression (1).

$$K = E_s I_s + mE_c I_c \tag{1}$$

where E_s and E_c are the elastic modulus of steel and concrete; I_s and I_c are the moment of inertia of steel and concrete; m is concrete contribution reduction factor.

In different codes, E_s, E_c are defined different ways and determined from the constituent's materials. The reduction coefficient m takes various values in the different design codes as following: m=0.2 in AIJ (1997); m=1 in BS5400 (1979); m=0.26 in EC4 (1994); m=0.8 in AISC-LRFD (1999) and DBJ13-15(2003).

Table 4 Calculation and Test Results of Stiffness

Specimen	Test value		AIJ (1997)		BS5400 (1979)		EC4 (1994)		AISC-LRFD (1999)		DBJ13-51 (2003)	
	$K_{0.2}$	$K_{0.6}$	$\frac{K^C}{K_{0.2}}$	$\frac{K^C}{K_{0.6}}$	$\frac{K^C}{K_{0.2}}$	$\frac{K^C}{K_{0.6}}$	$\frac{K^C}{K_{0.2}}$	$\frac{K^C}{K_{0.6}}$	$\frac{K^C}{K_{0.2}}$	$\frac{K^C}{K_{0.6}}$	$\frac{K^C}{K_{0.2}}$	$\frac{K^C}{K_{0.6}}$
CS114-2.5-30	318.1	268.5	0.98	1.16	1.17	1.39	1.28	1.51	1.26	1.49	1.22	1.45
CS114-2.5-50	309.8	261.1	1.04	1.23	1.39	1.64	1.36	1.62	1.40	1.66	1.29	1.53
CS114-3.8-30	433.3	335.8	1.02	1.31	1.15	1.48	1.21	1.57	1.19	1.53	1.18	1.52
CS114-3.8-50	414.0	347.6	1.08	1.29	1.32	1.57	1.31	1.56	1.32	1.57	1.26	1.50
CS165-2.5-30	960.3	875.6	1.05	1.16	1.35	1.48	1.51	1.66	1.49	1.64	1.42	1.56
CS165-3.8-30	1313.0	1157.6	1.09	1.23	1.29	1.46	1.40	1.58	1.37	1.56	1.34	1.52
CS165-3.8-50	1292.1	1174.3	1.13	1.25	1.50	1.65	1.47	1.62	1.51	1.66	1.40	1.54
MEAN			1.06	1.23	1.31	1.53	1.36	1.59	1.36	1.59	1.30	1.52
STDEV			0.046	0.053	0.113	0.091	0.099	0.045	0.110	0.063	0.085	0.034

Different moments gained from the test due to the different stiffness. So, two stiffness values adopted to check the calculation results. The stiffness corresponding to $0.2M_u$ and $0.6M_u$ were defined as initial stiffness ($K_{0.2}$) and serviceability-level stiffness ($K_{0.6}$) respectively. Table 4 lists a comparison between the calculation and test results where, the test values are the average ones, and K^C is the value calculated by the codes.

From Table 4, AIJ code gave the best precision among the other codes compared in this paper. A mean value = 1.06 and a standard deviation (STDEV) = 0.046 for $K_{0.2}$ gained by AIJ code, while the other codes gave mean values with almost 30% more than the test results. For $K_{0.6}$, although AIJ gave a mean value =1.23 and STDEV = 0.053 which is not perfect result, the other codes gave mean values with 50% more the test results. So, it is possible to judge that AIJ code is the best predictor for LACFST beam stiffness and can be used to calculate it. Referring to Han Linhai [6], it can be decided the calculation results of LACFST are similar to those of normal concrete (CFST). Therefore, a value equal to 0.2 adopted for m in expression (1). And AIJ code is also suggested to calculate stiffness of LACFST.

4.3 Moment Capacity Calculation of Codes

Several expressions in different design codes for normal CFST used to calculate the moment capacity of the specimens. These expressions may be described as follows:
For AIJ (1997) [17]

$$M_u = Zf_y = \frac{D^3 - (D-2t)^3}{6} f_y \tag{2}$$

where f_y is the yield strength of steel; D is the diameter ; t is the thickness of steel tube.
For AISC-LRFD(1999)[20]

$$M_u = \phi_b Z f_y = \phi_b \frac{D^3 - (D-2t)^3}{6} f_y \tag{3}$$

where φ_b=0.9, the other parameters have similar definitions as it is described in Eq. 3.

For EC4 (1994) [19]

$$M_u = W_{pa} f_y / \gamma_s + \frac{1}{2} W_{pc} f_c^{'} / \gamma_c - W_{pan} f_y / \gamma_s - \frac{1}{2} W_{pcn} f_c^{'} / \gamma_c \tag{4}$$

$$W_{pc} = (D-2t)^3 / 4 - 2r^3 / 3 - r^2 (4-\pi)(0.5D - t - r) \tag{5}$$

$$W_{pa} = D^3 / 4 - 2(r+t)^3 / 3 - (r+t)^2 (4-\pi)(0.5D - t - r) - W_{pc} \tag{6}$$

$$W_{pcn} = (D-2t) h_n^2 \tag{7}$$

$$W_{pan} = D h_n^2 - W_{pcn} \tag{8}$$

$$hn = \frac{A_c f_c^{'} / \gamma_c}{2D f_c^{'} / \gamma_c + 4t(2 f_y / \gamma_s - f_c^{'} / \gamma_{c)}} \tag{9}$$

where γ_c=1.5; γ_s=1.1; f_c' is the cylindrical compressive strength of concrete; r is the internal radius; A_c is the area of concrete; the other parameters have similar definitions as description in Eq. 3.

For DLT5085 (1999) [22]

$$M_u = \gamma_m W_{sc} f_{sc} \tag{10}$$

$$\gamma_m = -0.4047\xi + 1.7629\sqrt{\xi} \tag{11}$$

$$f_{sc} = (1.212 + B_1 \xi + C_1 \xi^2) f_{ck} \tag{12}$$

$$B_1 = 0.1759 f_y / 235 + 0.974 \tag{13}$$

$$C_1 = -0.1038 f_{ck} / 20 + 0.0309 \tag{14}$$

where $\xi = A_s f_y / (A_c f_{ck})$; $W_{sc} = \pi D^4 / 32$; f_{ck} is the concrete strength; A_s and A_c is the area of steel and concrete respectively.

For DBJ13-51(2003) [21]

$$M_u = \gamma_m W_{sc} f_{sc} \tag{15}$$

$$\gamma_m = 1.1 + 0.48 \ln(\xi + 0.1) \tag{16}$$

$$f_{sc} = (1.14 + 1.02\xi) f_{ck} \tag{17}$$

where all the parameters have the same meanings as it is described in DLT5085 (1999) code above.

The results gained from different codes are listed in Table 4. M_u is the average moment capacity value of a group of specimens, M_u^T is the calculated value. Referring to AIJ, BS5400, EC4, AISC-LRFD and DBJ13-15, the mean values for CS-165-2.5-30 group are 0.907, 0.817, 1.007, 1.352 and 1.041 which are larger and abnormal in compare with the other group's results. So, (CS-165-2.5-30) group is not included in Table 5 because it can't describe the real condition.

Table 5. Calculated Flexural Capacity Results

Specimen	M_u/ kN·m	AIJ $\frac{M_u^C}{M_u}$	AISC-LRFD $\frac{M_u^C}{M_u}$	EC4 $\frac{M_u^C}{M_u}$	DL/T5085 $\frac{M_u^C}{M_u}$	DBJ13-51 $\frac{M_u^C}{M_u}$	Method 1 $\frac{M_u^C}{M_u}$	Method 2 $\frac{M_u^C}{M_u}$
CS-114-2.5-30	11.75	0.790	0.711	0.846	1.101	0.873	1.046	0.997
CS-114-2.5-50	12.47	0.744	0.670	0.808	1.099	0.864	1.000	1.095
CS-114-3.8-30	15.23	0.833	0.749	0.863	1.118	0.929	1.077	0.888
CS-114-3.8-50	16.75	0.757	0.681	0.795	1.062	0.875	0.993	0.919
CS-165-3.8-30	37.55	0.723	0.650	0.775	1.014	0.807	0.958	0.928
CS-165-3.8-50	38.86	0.698	0.628	0.760	1.040	0.820	0.940	1.049
MEAN		0.757	0.682	0.808	1.072	0.861	1. 002	0.979
STDEV		0.048	0.043	0.040	0.041	0.044	0. 052	0.093

By comparing the mean values and standard deviations (STDEV) that listed in table5; it can be recognized; DL/T5085 code gave the best accuracy among the codes consulted in this paper which, gave conservative results and moment capacity with more than 10% deviation from the test results. The results calculated by AIJ and AICS-LRFD are obviously small with deviation ratios more than 24% and 30% respectively and that may attributed to AIJ and AICS-LRFD calculation methods which ignore concrete contribution. Besides, in AICS-LRFD an extra reduction coefficient for the steel tube capacity have been considered.

5. FLEXURAL CAPACITY CALCULATION METHOD

5.1 Method of Mechanical Equilibrium

The stress distribution of steel apparently influences the capacity of specimen. So, the strain of steel tube corresponding to moment capacity is listed in Table 6. In this test, the moment capacity took the value when the maximum steel fiber strain was 0.01. Because strain 1 in Figure 2 is the maximum steel fiber strain, all the strains in Table 6 took the values when strain 1 is 0.01.

Table 6. The longitudinal strains of steel tube corresponding to the moment capacity

Specimen	Strain 1 ($\times10^{-6}$)	Strain 2 ($\times10^{-6}$)	Strain 3 ($\times10^{-6}$)	Strain 4 ($\times10^{-6}$)	Strain 5 ($\times10^{-6}$)
CFST114-2.5-30-A	10000	2195	-8408	2884	
CFST114-2.5-30-B	10012	2987	-7927	2650	
CFST114-2.5-30-C	10003	1806	-7350	2940	
CFST114-2.5-50-A	10029	2669	-8284	1909	
CFST114-2.5-50-B	10051	2791	-3790	2689	
CFST114-2.5-50-C	9994	3163	-8256	2445	
CFST114-3.8-30-A	10034	1381	-7373	2130	
CFST114-3.8-30-B	10024	2445	-7408	-	
CFST114-3.8-30-C	10001	1517	-7416	2423	
CFST114-3.8-50-A	10033	2793	-9585	2479	
CFST114-3.8-50-B	9966	1216	-8032	1603	
CFST114-3.8-50-C	10107	464	-8683	1361	
CFST165-2.5-30-A	10010	7144	3043	-5542	-5976
CFST165-2.5-30-B	10093	9238	4193	-1962	-3886

CFST165-2.5-30-C	9995	7626	2342	-1326	-3040
CFST165-3.8-30-A	10031	7065	2528	-3475	-5494
CFST165-3.8-30-B	10056	6194	2526	-3429	-4309
CFST165-3.8-30-C	10061	7442	2846	-2663	-4246
CFST165-3.8-50-A	9981	9047	1805	-1715	-5824
CFST165-3.8-50-B	10003	7869	3528	-5346	-4892
CFST165-3.8-50-C	10000	7600	2849	-1814	-3685

Referring to table 6, almost all the strain values are larger than 2000×10^{-6} in response to the beam moment capacity. As the yield strain of steel in this test is about 2000×10^{-6}; the whole steel section yielded corresponding to the moment capacity. If the strain of concrete assumed to reach to the concrete strength corresponding to the moment capacity, then stress distribution and calculation chart may describe as it can be seen in Figure 12.

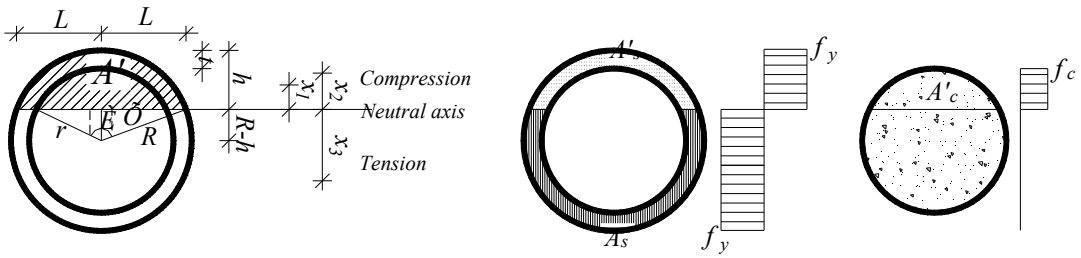

(a) Whole section (b) Steel tube (c) Concrete

Figure 12. Cross-Sectional Stress Distribution Corresponding to Moment Capacity

Due to the concrete weakness in tension its impact in the tension zone was ignored. Based on the mechanical equilibrium on the whole section, an equilibrium equation can be expressed in Eq. 18.

$$A_s f_y = A_c' f_c + A_s' f_y' \tag{18}$$

where, A_s is the tension area of steel; A_s' is the compression area of steel; A_c' is the compression area of concrete; $f_y' = f_y$ is the compressive strength of steel; f_c is the constrained concrete strength. All the area can be calculated with the size of the section.

From the previous study carried [23], the strength of constrained concrete of steel may calculated by expression (19).

$$f_c = f_{ck} + k \bullet p \tag{19}$$

where, k is an enhancing coefficient and according to this study result for LACFST can take a value equal to 3.4 and P is the confining force.

$$p = 2t\sigma_{sh} / D = 2t\upsilon\sigma_l / D \tag{20}$$

where, σ_{sh} is the circumferential stress; σ_l is the longitudinal stress; υ is the lateral deformation coefficient. When reaching to the beam moment capacity, $\sigma_l = f_y$ and υ can take the Poisson's ratio of steel. So, the following expression can be got.

$$f_c = f_{ck} + 2k\upsilon f_y / D \tag{21}$$

After calculating the height of the compression area (h) the moment capacity of the section can be found from expression (22).

$$M_u = A_c' f_c x_1 + A_s' f_y' x_2 + A_s f_y x_3 \tag{22}$$

where, x_1, x_2 and x_3 are the distances between the centroid of compression concrete, compression steel and tension steel area to the neutral axis respectively.

5.2 Method of Combined Strength

The method of mechanical equilibrium seems complex. So, an attempt to find a simple method similar to that one proposed by Han Linhai [6] was carried out. Accordingly; the moment capacity M_u can be calculated by using expression (23).

$$M_u = \gamma_m W_{sc} f_{sc} \tag{23}$$

$$f_{sc} = N_u / A_{sc} \tag{24}$$

where, γ_m is an enhancement coefficient considering the contribution of steel after yielded; N_u is the compressive capacity of a stub LACFST specimen. If the concrete increment strength Considered; N_u can be following expressed according to previous study [24].

$$N_u = f_y A_s + \beta f_{ck} A_c \tag{25}$$

Where β is the concrete strength increment coefficient and expressed by the following form according to previous study [24]:

$$\beta = 1.36 + 0.3\ \xi \tag{26}$$

Therefore, the capacity of LACFST short stub may calculate by expression (17), and can simplify as shown in Eq. 28. The two expressions (27) and (28) have showed good accuracy to calculate the bearing capacity. The results of expression (27) had a mean of 1.011 with STDEV of 0.045, while the results of expression of (28) had a mean of 0.997 with STDEV of 0.045[24] hence, they are reliable to use.

$$N_u = 1.3 f_y A_s + 1.36 f_{ck} A_c \tag{27}$$

$$N_u = 1.35(f_y A_s + f_{ck} A_c) \tag{28}$$

So, the two Eqs 29 and 30 can be used to calculate the strength of LACFST and the moment capacity respectively. Steel tube yielded when the section reached to its moment capacity, thus, the enhancement coefficient γ_m can take a value of 1.1.

$$f_{sc} = \frac{N_u}{A_{sc}} = \frac{1.35(f_y A_s + f_{ck} A_c)}{A_s + A_c} = \frac{1.35(1+\xi) f_{ck} A_c}{A_s + A_c} \tag{29}$$

$$M_u = 0.17 \gamma_m D(1+\xi) f_{ck} A_c \tag{30}$$

5.3 Comparison of the Results

Table 5 shows the results of the two methods used in this paper to calculate the moment capacity. Besides, Figure 13 was drawn to compare the calculated results and the test ones (Method 1 and Method 2 referred to the method of mechanical equilibrium and the method of combined strength respectively). From the figure, it can be seen that method 1 and method 2 has a mean of 1.002 and 0.979 with STDEV of 0.052 and 0.081 respectively where these figures reflect the good accuracy of the two methods. Because of the simplicity of method 2; the relation between the concrete strength increment coefficient and the confinement coefficient (ξ) expressed linearly. But it is proposed that this linear relation subject to further studies to get a more reliable expression. As a result of this comparison it is suggested to use method 1 to calculate the moment capacity.

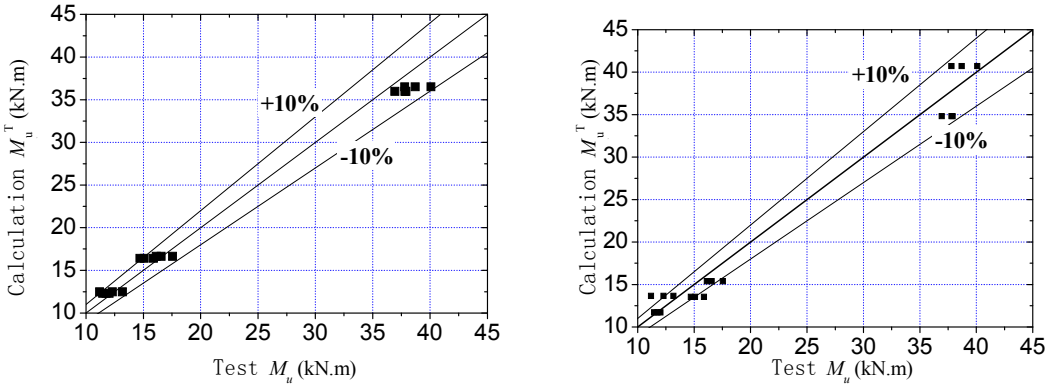

(a)Method 1 (b) Method 2

Figure 13. Comparison of Calculation and Test Results

6. NUMERICAL ANALYSIS

6.1 Constitutive Model of LAC

Formula of $\varepsilon_c = 1788 + 17.58 f_c$ was proposed to calculation the strain peak value of LAC without constraint [25]. It was used to establish the numerical mode of confined concrete in compressive region. Based on the model of confined normal concrete by Han Linhai [26], the model of confined LAC was proposed. In the model of this paper, the boundary value of confinement coefficient ξ was higher than the one in the model of confined normal concrete. This is because the enhanced strength by the restrain of steel tube for LAC is lower than the one of normal concrete. The relationship between strain and material strength was also fitted based on the previous experimental results [23].

The model of confined LAC in compressive region was proposed as following.

$$\sigma = \begin{cases} \sigma_o[A\dfrac{\varepsilon}{\varepsilon_o} - B(\dfrac{\varepsilon}{\varepsilon_o})^2] & (\varepsilon \le \varepsilon_o) \\ \sigma_0(1-q) + \sigma_0 q(\dfrac{\varepsilon}{\varepsilon_0})^{0.1\xi} & (\varepsilon > \varepsilon_o, \xi \ge 1.22) \\ \sigma_0(\dfrac{\varepsilon}{\varepsilon_0})\dfrac{1}{\beta(\varepsilon/\varepsilon_0 - 1)^2 + \varepsilon/\varepsilon_0} & (\varepsilon > \varepsilon_o, \xi < 1.22) \end{cases} \quad (31)$$

where, $\sigma_o = f_{ck}[1.194 + (\frac{13}{f_{ck}})^{0.45}(-0.07485\xi^2 + 0.5789\xi)]$

$$\varepsilon_o = \varepsilon_c + [1000 + 800(\frac{f_{ck} - 24}{24})]\xi^{0.2}$$

$$\varepsilon_c = 1788 + 17.58 f_{ck}$$

$$A = 2.0 - k$$

$$B = 1.0 - k$$

$$k = 0.1\xi^{0.745}$$

$$q = \frac{k}{0.2 + 0.1\xi}$$

$$\beta = (2.36 \times 10^{-5})^{[0.25 + (\xi - 0.5)^7]} \times 5.0 \times f_{ck}^2 \times 10^{-4}$$

The above model was used to calculate the relationship between stress and strain for confined LAC. In Figure 14, the calculation result was compared to the previous experimental one. The detailed introduction about the experiment can be found in reference [23]. In the figure, the specimens were the same one in reference [23]. The load acted on the steel was eliminated and the experiment curves of concrete were gained. From the figures, it shows that the model calculation results were identical with the experiment ones as well. So, the proposed model for confined LAC in this paper was reasonable and can be used in the analysis.

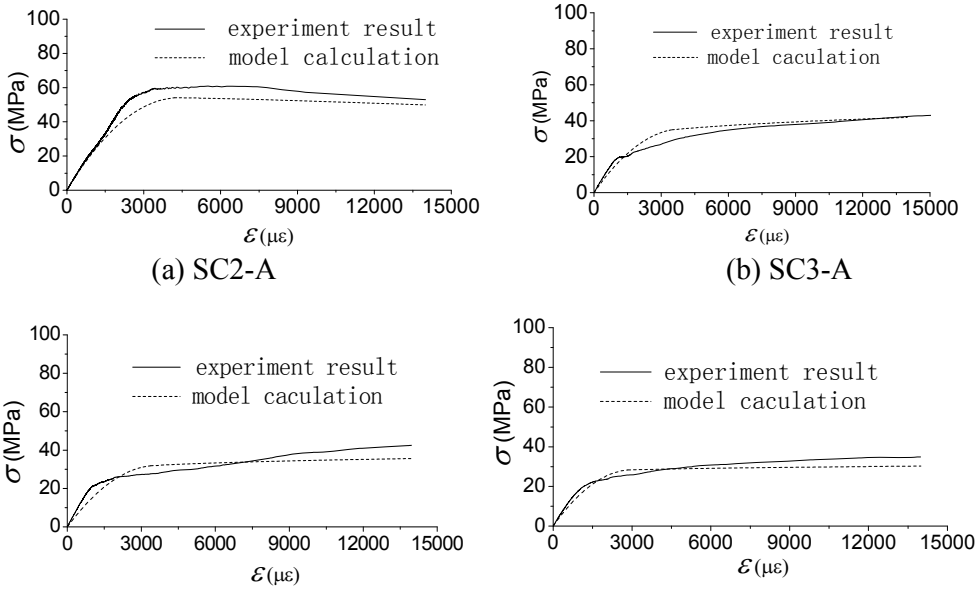

(a) SC2-A (b) SC3-A

(c) SC4-A (d) SC5-A

Figure 14. Comparison of Confined LAC Model and Experiment Result

The model of confined LAC in tensile region used the model proposed by Han Linhai [26] as following.

$$\sigma_c = \begin{cases} \sigma_p[1.2\varepsilon_c / \varepsilon_p - 0.2(\varepsilon_c / \varepsilon_p)^6] & \varepsilon_c \le \varepsilon_p \\ \sigma_p \dfrac{\varepsilon_c / \varepsilon_p}{0.31\sigma_p^2(\varepsilon_c / \varepsilon_p - 1)^{1.7} + \varepsilon_c / \varepsilon_p} & \varepsilon_c > \varepsilon_p \end{cases} \quad (32)$$

where, σ_p is the peak value of stress, it can be calculated as $\sigma_p = 0.26(1.25 f_{ck})^{2/3}$. ε_p is the strain corresponding to the peak value of stress, it can be calculated as $\varepsilon_p = 43.1\sigma_p \times 10^{-6}$.

6.2 The analysis model and result

In order to make FEM model, following assumptions were adopted. (1) The deformation of specimen's section agrees with the Bernoulli-Euler's theory at various loading stages. (2) There was no slip between the steel tube and LAC. (3) The deflection along the length distributed as half sine wave. All of the above three assumptions were proved by the experimental results.

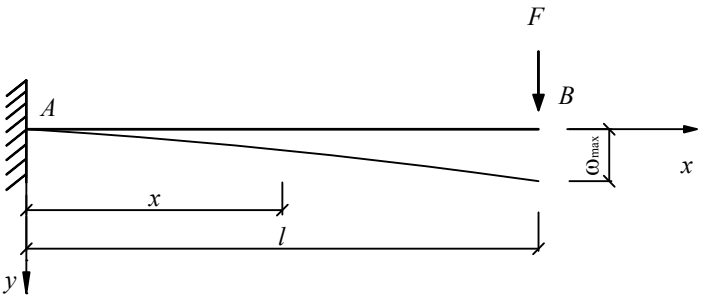

Figure 15. The Simplified Calculation Model for Flexural Behavior of LACFST

The calculation model was simplified to be a cantilever beam model which could reflect the same behavior of the test process. The simplified calculation model is shown in Figure 15. In ANSYS program, SOLID65 was used for LAC and SOLID186 was used for steel tube. Element of TARGE170 and CONTA173 were used for the contact relationship between steel tube and LAC. The mechanical properties of LAC and steel were the same to the results from the test. Von Mises kinematic hardening rule was adopted for steel material. In the stage of plastic hardening, the tangent modulus of steel took $0.01E_s$ (E_s is Elastic modulus of steel). In this analysis, the displacement loading method was used.

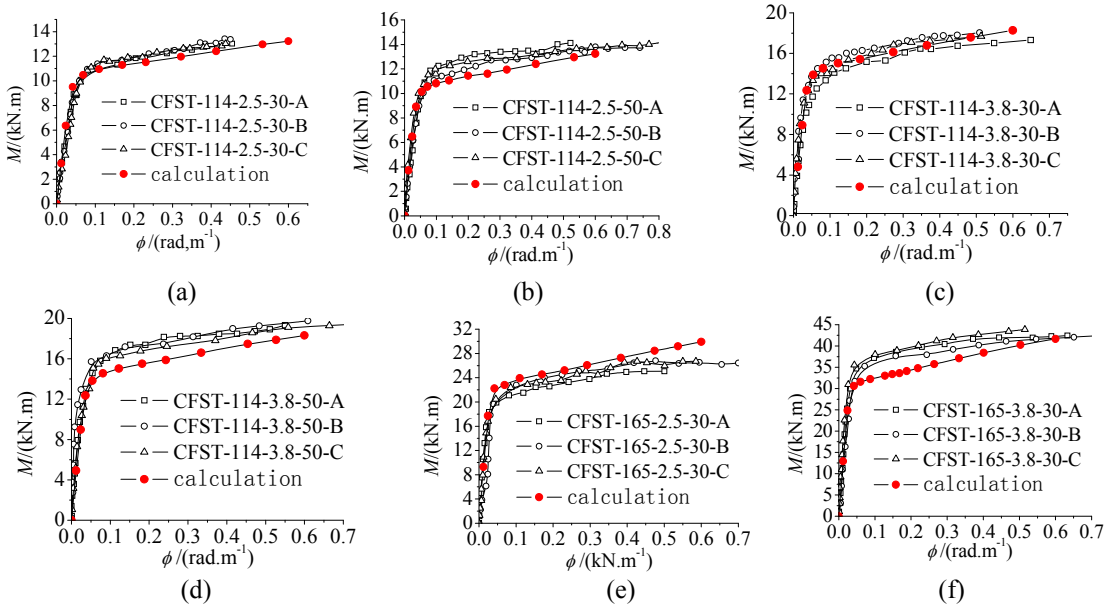

Figure 16. Comparison of Test and Calculation Results

The calculation results are shown in Figure 16. As the figure shows, the calculation results fit with the experiment results well. So, it can be got that the constitutive model of LAC established in this paper can be used for the analysis of LACFST with good accuracy.

7. CONCLUSIONS

(1) From the test noticed the strain distribution and the deflection distribution along the length at various loading stages agrees with the Bernoulli-Euler's theory and half sine wave curve respectively.

(2) Filling with LAC can obviously improve the flexural behavior of steel tube. The moment capacity of LACFST increased as the steel ratio and LAC concrete strength increased. The shear span ratio almost has no influence on the flexural behavior of LACFST. The increment of moment capacity was not obvious when the high strength LAC used.

(3) Compared to other codes mentioned in this paper, the method of AIJ (1997) has a good accuracy for calculation the stiffness. And the results using DL/T5085 to calculate moment capacity are closest to the test ones with a mean of 1.072 and STDEV of 0.041. Besides, the deviation of moment capacity calculation using other codes is 10% more or less than the test one.

(4) Two methods were provided in this paper; the method of mechanical equilibrium and the method of combined strength which has a mean of 1.002 and 0.979 with STDEV of 0.052 and 0.081 respectively. Therefore, from this study it is possible to suggest that both methods can be used to calculate the moment capacity.

(5) The constitutive model of confined LAC in compressive region was established. And it was proved to be accuracy enough. Based on some assumptions which were proved reasonable by the test, the constitutive model was used in the FEM to analyze the flexural behavior and the results fit with the experiment results well.

ACKNOWLEDGMENTS

The authors appreciate the support of The National Natural Science Fund (No.51208176); The authors appreciate the support of China Postdoctoral Science Foundation (2012M511187), The Fundamental Research Funds for the Central Universities (2012B02914).

REFERENCES

[1] Ge, H.B., Susantha, K.A.S., Satake, Y., et al., "Seismic Demand Predictions of Cconcrete-filled Steel Box Columns", Engineering Structures, 2003,Vol. 25, No. 3, pp. 337-345.

[2] Gao, S.B. and Ge, H.B., "Numerical Simulation of Hollow and Concrete-filled Steel Columns", Advanced Steel Construction, 2007, Vol. 3, No. 3, pp. 668-678.

[3] Montejo, L.A., Gonzalez-Roman, L.A. and Kowalsky, M.J., "Seismic Performance Evaluation of Reinforced Concrete-Filled Steel Tube Pile/Column Bridge Bents", Journal of Earthquake Engineering, 2012, Vol. 16, No. 3, pp. 401-424.

[4] Morcous, G., Hanna, K., Deng, Y., et al., "Concrete-Filled Steel Tubular Tied Arch Bridge System: Application to Columbus Viaduct ", Journal of Bridge Engineering, 2012, Vol. 17, No. 1, pp. 107-116.
[5] Kang, J.Y., Choi, E.S., Chin, W.J., et al, "Flexural Behavior of Concrete-filled Steel Tube Members and its Application", International Journal of Steel Structures, 2007, Vol. 7, No. 4, pp.319-324.
[6] Mossahebi, N., Yakel, A. and Azizinamini, A., "Experimental Investigation of a Bridge Girder made of Steel Tube Filled with Concrete", Journal of Constructional Steel Research, 2005, Vol. 61, No. 3, pp. 371-386.
[7] Mohamed, H.M. and Masmoudi, R., "Flexural Strength and Behavior of Steel and FRP-reinforced Concrete-filled FRP Tube Beams", Engineering Structures, 2010, Vol. 32, No. 11, pp. 3789-3800.
[8] Soundararajan, A. and Shanmugasundaram, K., "Flexural Behaviour of Concrete-Filled Steel Hollow Sections Beams", Journal of Civil Engineering and Management, 2008, Vol.14, No. 2, pp. 107-114.
[9] Han, LH, "Flexural Behaviour of Concrete-filled Steel Tubes", Journal of Constructional Steel Research, 2004, Vol. 60, No. 2, pp. 313-337.
[10] Deng, Y., Tuan, C.Y. and Xiao, Y., "Flexural Behavior of Concrete-Filled Circular Steel Tubes under High-Strain Rate Impact Loading", Journal of Structural Engineering-ASCE, 2012, Vol. 138, No. 3, pp. 449-456.
[11] Nakamura, S., Momiyama, Y., Hosaka, T., et al., "New Technologies of Steel/Concrete Composite Bridges", Journal of Constructional Steel Research, 2002, Vol. 58, No. 1, pp. 99-130.
[12] Ghannam, S, Jawad, Y.A. and Hunaiti, Y., "Failure of Lightweight Aggregate Concrete-Filled Steel tTubular Columns", Steel and Composite Structures, 2004, Vol. 4, No. 1, pp. 1-8.
[13] Mouli, M. and Khelafi, H., "Strength of Short Composite Rectangular Hollow Section Columns Filled with Lightweight Aggregate Concrete", Engineering Structures, 2007, Vol. 29, No. 8, pp. 1791-1797.
[14] Assi, I.M., Qudeimat, E.M. and Hunaiti, Y., "Ultimate Moment Capacity of Foamed and Lightweight Aggregate Concrete-filled Steel Tubes", Steel and Composite Structures, 2003, Vol. 3, No. 3, pp. 199-212.
[15] Fu, Z.Q., Ji B.H, Lv, L. and Zhou, W.J., "The Behavior of Lightweight Aggregate Concrete Filled Steel Tube Slender Columns under Axial Compression", Advanced Steel Construction, 2011, Vol. 7, No. 2, pp. 144-156.
[16] Elzien, A., Ji, B.H., Fu, Z.Q. and Hu, Z.Q, "The Behavior of Lightweight Aggregate Concrete Filled Steel Tube Columns under Eccentric Loading", Steel and Composite Structures, 2011, Vol. 11, No. 6, pp. 469-488.
[17] Architectural Institute of Japan (AIJ), "Recommendations for Design and Construction of Concrete Filled Steel Tubular Structures", 1997.
[18] British Standard Institute, "BS5400, Part 5, Concrete and Composite Bridges", 1979.
[19] Eurocode 4, "Design of Composite Steel and Concrete Structures", 1994.
[20] AISC, "Load and Resistance Factor Design Specification for Structural Steel Buildings", 1999.
[21] Engineering Construction Standard of Fujian Province of China, "Technical Specification for Concrete-Filled Steel Tubular Structures", 2003. (In Chinese)
[22] Electric Power Industry Standard of China, "Code for Design of Steel-Concrete Composite Structures", 1999. (In Chinese)
[23] Fu, Z.Q., Ji B.H., Lv, L. and Yang M., "The Mechanical Properties of Lightweight Aggregate Concrete Constrained by Steel Tube", Geotechnical Special Publication ASCE, 2011, No. 219, pp. 33-39.

[24] Fu, Z.Q., Ji B.H., Zhou, Y. and Wang X.L., "An Experimental Behavior of Lightweight Aggregate Concrete Filled Steel Tubular Stub under Axial Compression", Geotechnical Special Publication ASCE, 2011, No. 219, pp. 24-32.
[25] Wang, P. T., Shah, S. P. and Naaman, A.E., "Stress-Strain Curves of Normal and Lightweight Concrete in Compression", Journal of American Concrete Institute, 1978, Vol. 75, No. 11, pp. 603-611.
[26] Han, L.H., "Concrete Filled Steel Tube Structure - Theory and Application (Second Edition)", Science Press, 2007. (In Chinese)

PRECISION CONTROL METHOD FOR PRE-STRESSING CONSTRUCTION OF SUSPEN-DOME STRUCTURES

Hongbo Liu [1,2], Qinghua Han[2], Zhihua Chen [1,2], Xiaodun Wang[2,*], Ren-Zhang Yan[2] and Bo Zhao[2]

[1] *State Key Laboratory Of Hydraulic Engineering Simulation And Safety, Tianjin University, Tianjin 300072, China*
[2] *Tianjin Key Laboratory of Civil Engineering Structure & New Materials, Tianjin University, Tianjin 300072, China*
**(Corresponding author: E-mail: maodun2004@126.com)*

Received: 15 October 2012; Revised: 30 September 2013; Accepted: 19 December 2013

ABSTRACT: A significant pre-stressing deviation from the pre-stressing target force is induced by the temperature change and sliding friction between hoop cables and cable-strut joints during the pre-stressing construction of suspen-dome structures. The deviation not only induces a considerable increase in member stress and nodal displacement but also reduces the load-bearing capacity of suspen-dome structures. To reduce this pre-stressing deviation, construction measures such as the use of a sufficient number of pre-stressing points, over pre-stressing construction, adoption of rolling cable-strut joints, and modification of the pre-stressing control value with temperature change were developed. A suspen-dome specimen with a diameter of 10.8 m was designed to clarify the aforementioned construction measures. Six schemes were designed and implemented based on this specimen. Finite element analysis was then conducted. Experimental and numerical results indicated that the construction measures presented in this paper could effectively reduce pre-stressing force deviation.

Keywords: Suspen-dome structures, Pre-stressing construction, Pre-stressing force deviation, Temperature change, sliding friction, Cable-strut joints, Experimental study, Numerical analysis

1. INTRODUCTION

A suspen-dome structure is a typical cable-strut structure that was first proposed by Kawaguchi [1]. A typical suspen-dome structure comprises an upper single-layer lattice shell and a low cable-strut system (Figure 1). The cable-strut system consists of hoop cables, radial cables, and struts. During the construction process, pre-stressing is introduced into the hoop cables to offset member stresses and nodal displacement under dead and live loads to increase the span of the suspen-dome structure. The suspen-dome structure has been widely applied in sports facilities and convention and exhibition centers in Japan and China [2–3].

Studies have been conducted to investigate the structural behavior of suspen-dome structures through both experimental and numerical analyses [4–19]. Previous research results provide many constructive suggestions and guidelines for the construction of suspen-dome structures. However, most studies have ignored the pre-stressing deviation induced by both temperature change and sliding friction between the hoop cables and cable-strut joints; pre-stressing deviations significantly affect the structural behavior of suspen-dome structures [4–5]. The aforementioned factors can increase the member stress and nodal displacement by 43.2% and 53.3%, respectively, under dead and live loads based on previous studies [6–7].

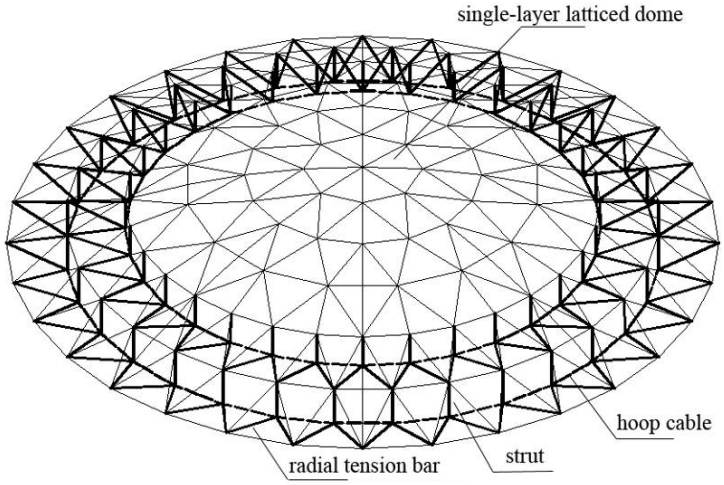

Figure 1. Structure Sketch Draw of Suspen-dome Structure

Therefore, this study aimed to find a solution for the aforementioned problems. Several construction measures were presented to reduce the effects of sliding friction and temperature change during construction. Thereafter, both numerical analysis and experimental study were conducted to verify the effects of construction measures on pre-stressing deviation reduction.

2. CONSTRUCTION MEASURES

Five construction measures, one of which simplifies the construction, are proposed in this section to reduce the pre-stressing deviation induced by sliding friction and temperature change during pre-stressing construction. These construction measures are described in detail as follows.

2.1 Setting a Sufficient Number of Pre-stressing Points

The pre-stressing deviation for each hoop decreases with increasing number of pre-stressing points. However, the construction cost will be high if the number of pre-stressing points is large. Therefore, an optimal number of pre-stressing points can obtain not only a low pre-stressing deviation but also an adequate construction cost.

Figure 2 shows that *n* cable-strut joints are located between two pre-stressing points. *n* can be either an odd (Figure 2(a)) or even number (Figure 2(b)). S-i denotes the *i*-th cable-strut joint, and C-i denotes the *i*-th hoop cable element (Figure 2).

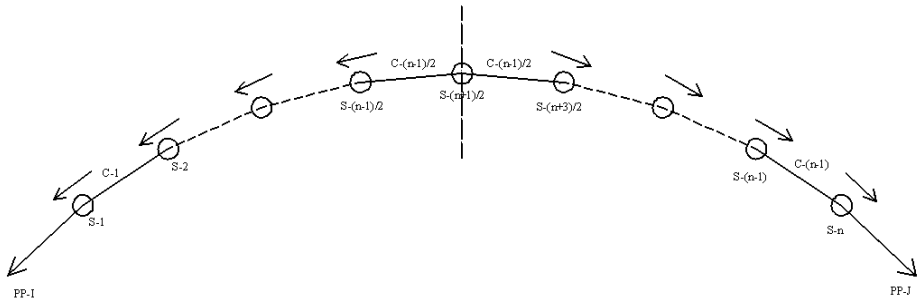

(a) Odd number of cable-strut joints

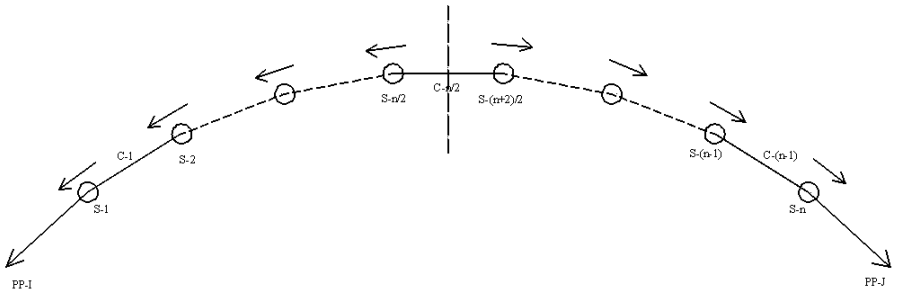

(b) Even number of cable-strut joints

Figure 2. Schematic of Cable Sliding between Two Pre-stressing Points

Figure 3 shows the tensions in the two hoop cables around a cable-strut joint with slip. The inertial effect of the joint is neglected. The relationship between the tensions at two sides on the slipping edge is expressed by Euler's equation:

$$T_2 = \alpha T_1, \tag{1}$$

where the tension ratio α is

$$\alpha = e^{\mu\theta}. \tag{2}$$

μ is the friction coefficient, and θ is the contact angle (Figure 3). Eq. 1 was applied to build the relationship between the tensions in the two adjacent hoop cable elements in suspen-dome structures.

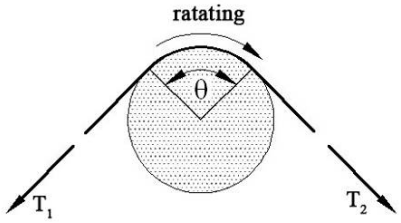

Figure 3. Hoop Cable Passing through a Cable-strut Joint

On the basis of the aforementioned mechanical principle and given that no other construction measures are implemented, the relationship between the maximum pre-stressing loss ω and number of cable-strut joints n (Figure 2) can be expressed as follows:

$$\omega = 1 - \frac{1}{\alpha^{\text{nint}(n/2)}}. \tag{3}$$

The optimal number *n* of cable-strut joints between two pre-stressing points was calculated by using Eq. 3. Furthermore, the optimal number of pre-stressing points could be obtained based on *n*.

2.2 Over pre-stressing Construction

During the pre-stressing construction of suspen-dome structures, over pre-stressing construction could reduce the pre-stressing loss induced by the sliding friction between the hoop cables and cable-strut joints. The best scheme for over pre-stressing construction included two steps. First, the

pre-stressing construction was conducted by using a pre-stressing construction control value T_{01} ($T_{01} > T$, where T denotes the design pre-stressing value). Second, the tensions at the pre-stressing points were relaxed to T_{02} ($T_{02} < T$). The key point for this construction measure was to determine the values of T_{01} and T_{02} to minimize the pre-stressing deviation from the target value in the hoop cables.

In the first step, the tension force T_{min} of hoop cable element *S-(n-1)/2* (Figure 2(a)) or *S-n/2* (Figure 2(b)) could be calculated by using the following equation:

$$T_{\min} = T_{01} \frac{1}{\alpha^{\text{nint}(n/2)}} . \tag{4}$$

In the second step, the sliding direction at the *m*-th cable-strut joint changed when the tensions at the pre-stressing points were relaxed to T_{02} (Figure 4). Assuming that the tension of the *m*-th hoop cable element is T_m, the tension T_{mid} of hoop cable element *S-(n-1)/2* (Figure 2(a)) or *S-n/2* (Figure 2(b)) could be calculated by Eq. 5. The tension T_{02} at the pre-stressing point could be calculated as follows:

$$T_{\text{mid}} = T_{\min} = T_m \frac{1}{\alpha^{\text{nint}(n/2)-\text{m}}}, \tag{5}$$

$$T_{02} = T_m \frac{1}{\alpha^{\text{m}}}, \tag{6}$$

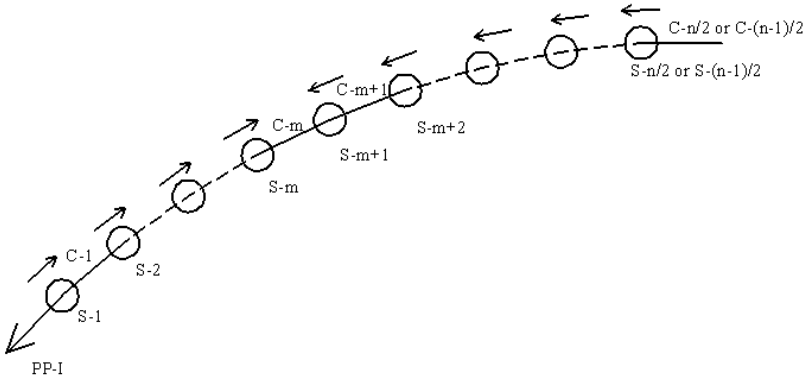

Figure 4. Schematic of Cable sliding in the Second Step

The error β (calculated by Eq. 7) must be minimized to obtain a minimum deviation. On the basis of advanced mathematics theory, Eqs. 8 and 9 must be satisfied by minimizing β. Therefore, Eq. 8 was obtained. *m* could be determined to be $\text{nint}(n/2)/2$ by Eq. 8. T_m could be calculated in Eq. 10 by Eq. 9, and T_{02} could be determined by Eq. 11. T_{01} could be determined in Eq. 12 by Eqs. 4 and 5.

$$\beta = \max(T - T_{mid}, T - T_{02}, T_m - T), \tag{7}$$

$$T - T_m \frac{1}{\alpha^{\text{nint}(n/2)-\text{m}}} = T - T_m \frac{1}{\alpha^{\text{m}}}, \tag{8}$$

$$T - T_m \frac{1}{\alpha^{\text{m}}} = T_m - T, \tag{9}$$

$$T_m = \frac{2T}{1+\frac{1}{\alpha^m}}, \tag{10}$$

$$T_{02} = \frac{2T}{1+\alpha^m}, \tag{11}$$

$$T_{01} = \frac{2T}{1+\alpha^m} \times \alpha^{\text{nint}(n/2)}. \tag{12}$$

2.3 Adoption of Rolling Cable-strut Joints

A continuous cable-strut joint has two types. One type is the sliding cable-strut joint, wherein cable forces are transferred by sliding around the joints. The other type is the rolling cable-strut joint, wherein cable forces are transferred by rolling around the joints [8–9]. Rolling friction is less than the sliding friction. Therefore, the rolling cable-strut joint was suggested for the pre-stressing construction of suspend-dome structures.

2.4 Adjustment of Control Pre-stressing Value According to Temperature Change

The temperature of suspen-dome structures changes significantly during construction because of the long pre-stressing construction period (e.g., one month) of large suspen-dome structures. Furthermore, the construction schedule might be arranged within a year. Therefore, the construction temperature will deviate from the design temperature during the pre-stressing construction. Consequently, the design pre-stressing had to be corrected based on the construction site temperature. Otherwise, the pre-stressing forces in the cables would significantly deviate from the target value. The corrected formula can be expressed as follows by using the linear assumption:

$$T_{mi} = T_i - (t_i - t_0)T_{i\Delta T}^{dome} - (t_i - t_0)T_{i\Delta T}^{cable}, \tag{13}$$

where $T_i\left(i = 1, 2, \cdots, n\right)$ is the control value of the pre-stressing construction of the *i*-th hoop cable elements in suspen-dome structures. $T_i\left(i = 1, 2, \cdots, n\right)$ could be obtained by a tensile force compensation analysis without considering the temperature change during construction. $T_{i\Delta T}^{dome}(i = 1, 2\cdots, n)$ is the variation value of the internal force for hoop cables and could be obtained by applying a temperature change with a value of 1 °C on the upper dome and strut members. $T_{i\Delta T}^{cable}(i = 1, 2\cdots, n)$ is the variation value of the internal force for hoop cables and could be obtained by applying a temperature change with a value of 1 °C on the low cable element. t_0 is the design construction temperature, t_i is the construction temperature when the *i*-th hoop cables are pre-tensioned, and T_{mi} is the control value of the pre-stressing construction for the *i*-th hoop cables based on the temperature correction.

2.5 Choosing the Proper Pre-stressing Time

On the basis of the analysis and formula correction of the pre-stressing construction of suspen-dome structures, the pre-stressing cable force would be reduced if the temperature of the construction site was higher than the design temperature during pre-stressing construction. Therefore, the pre-stressing construction should be conducted at the hottest time during the construction period.

3. EXPERIMENTAL PROGRAM

3.1 Specimen Configuration

A scaled specimen of a suspen-dome structure was designed and tested to verify the rationality of the construction measures presented in Section 2. Furthermore, the experiment results not only provided insights into the changes of hoop cable forces but also generated data to compare and verify the numerical results obtained by the method presented in Reference [12].

The span and height of this scaled specimen are 10.8 and 2.6 m, respectively. The specimen consisted of a single-layer latticed shell (Figure 5) and one-loop cable-strut system (Figure 6). Four types of steel tubes, namely, $\phi 12 \times 3$, $\phi 14 \times 3$, $\phi 16 \times 3$, and $\phi 18 \times 3$, were adopted as the members of the single-layer lattice dome. The members are connected to each other by welded hollow spherical joints, which could be considered rigid joints. Steel tube $\phi 13 \times 3$ is adopted for the struts. The diameters of the hoop cables and radial steel bars are 12 and 11.5 mm, respectively. Figure 7 shows that the entire scaled suspen-dome specimen was supported by 48 steel columns. The 48 steel columns were arranged in two rings.

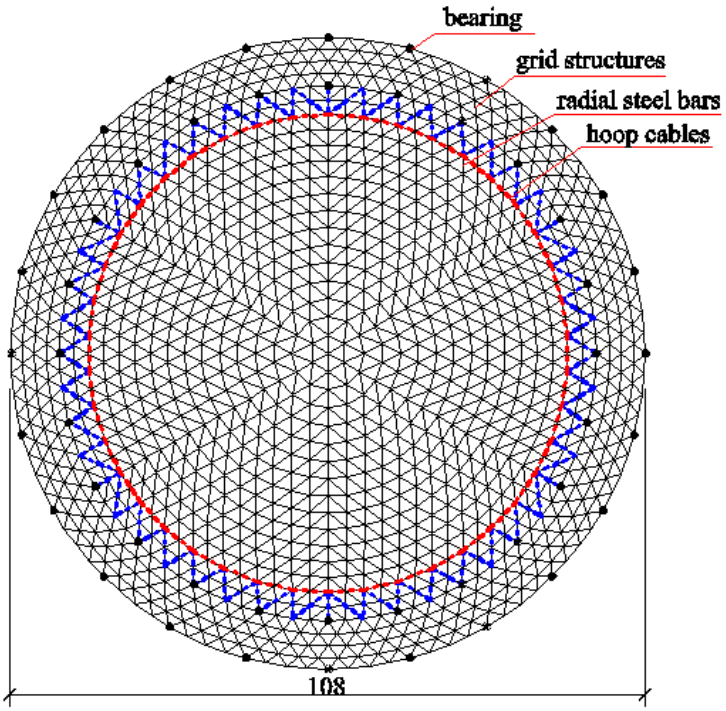

Figure 5. Top View of the Suspen-dome Structure

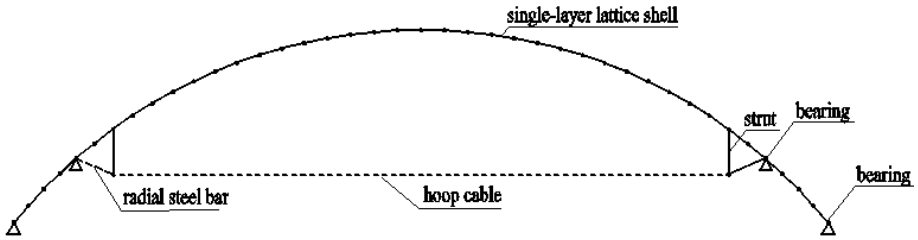

Figure 6. Sectional View of the Suspen-dome Structure

Figure 7. Tested Suspen-dome Model

A new cable-strut joint called the rolling cable-strut joint was adopted in the scaled specimen. Figures 8 and 9 show the assembly drawing and photo, respectively. Compared with the past continuous cable joint, the friction between the cable and joint was replaced with rolling friction because rolling friction was significantly smaller than the sliding friction. Therefore, this joint could reduce the pre-stressing loss induced by friction during pre-stressing construction.

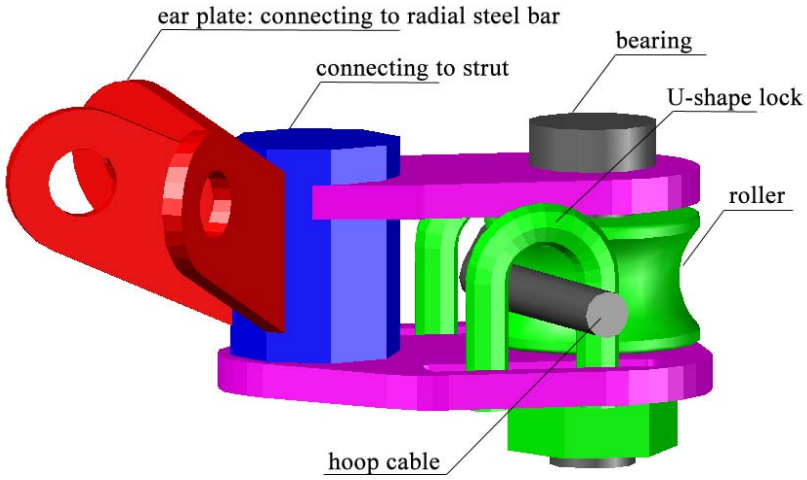

Figure 8. Assembly Drawing of the Rolling Cable-strut Joint

Figure 9. Photo of the Rolling Cable-strut Joint

In this specimen, screw bolts were used in the radial steel bars to adjust the length. The strain gauge could not be glued directly to the cable surface to measure the cable strain because of a large measurement error. In this test, the steel tubes were connected to the cables, and the strain gauge was glued to the steel tube surfaces to measure the cable strain (Figure 10). Figure 11 shows the tensioning device used in the experiment. For this device, tension was applied on the cable by bolt tightening.

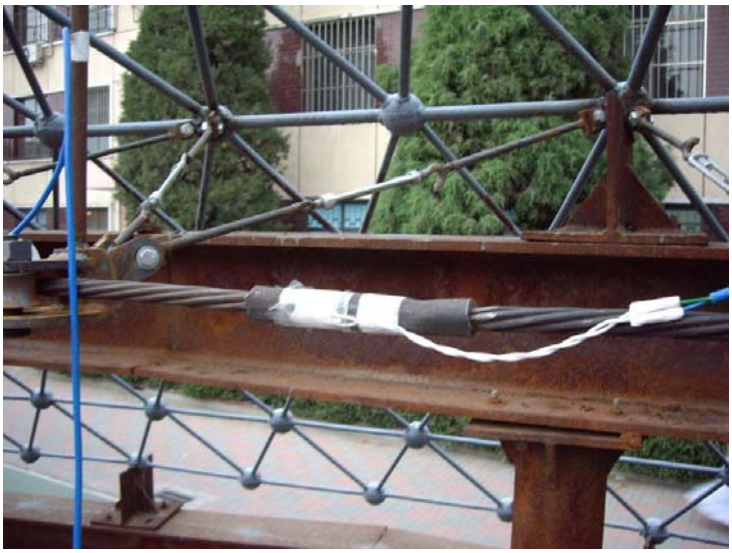

Figure 10. Steel Tube Connected in the Cables

Figure 11. Tensioning Device used in the Experiment

3.2 Experimental Scheme

In this test, 4 tensioning devices were designed, and 16 steel tubes were included in the hoop cables. Figure 12 shows the number of tensioning devices and hoop cables, including steel tubes.

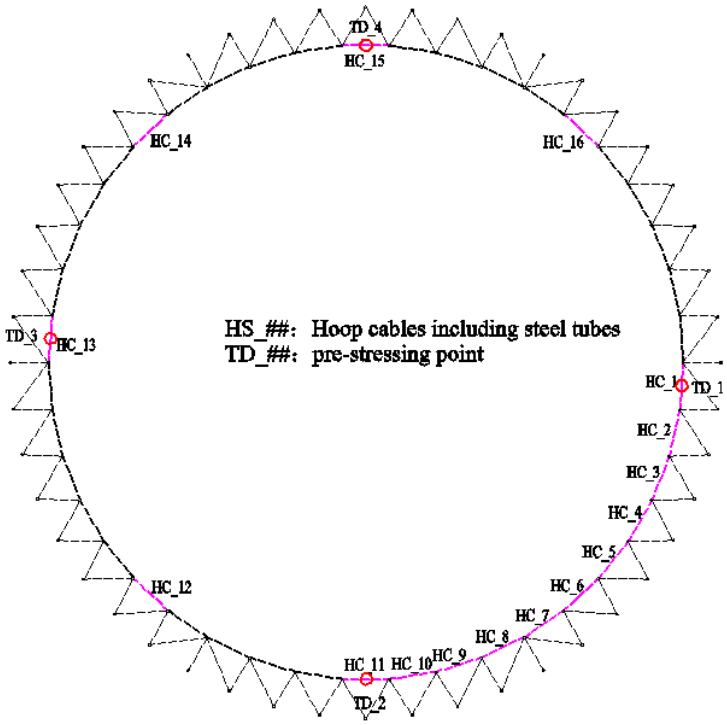

Figure 12. Arrangement of tensioning devices and hoop cables, including steel tubes

Six pre-stressing experimental schemes were designed through scheme optimization to verify the rationality of the five construction measures presented in Section 2. The detailed descriptions of the five schemes are as follows:

Scheme 1: One tensioning device (TD-1) was used, and over pre-stressing construction was not considered. The pre-stressing control value was 10420 N.

Scheme 2: Four pre-stressing points were used, and over pre-stressing construction was not considered. The pre-stressing control value was 10420 N.

Scheme 3: Four pre-stressing points were used, and over pre-stressing construction was considered. The pre-stressing control values T_{01} and T_{02} for the first and second steps were 11532 and 10155 N, respectively (Eqs. (11) and (12)).

Scheme 4: Four pre-stressing points were used, and over pre-stressing construction was not considered. The pre-stressing control value was 10420 N, and the effect of daily temperature change was considered.

Scheme 5: Four pre-stressing points were used with the following assumptions: 1) the design temperature for pre-stressing construction was 25.5 °C; 2) the practical pre-stressing temperature was 55.5 °C; 3) the pre-stressing control value is 7520 N (Eq. (13)).

Scheme 6: Four pre-stressing points were used and both super-pre-stressing and temperature correction were considered. The following assumptions were made: 1) the design temperature for pre-stressing construction was 25.5 °C; 2) the practical pre-stressing temperature was 55.5 °C; 3) the pre-stressing control values T_{01} and T_{02} for the first and second steps were 8631 and 7255 N, respectively.

3.3 Determination of the Friction Coefficient Value

Three cases for the sliding cable-strut joint were tested to determine the friction coefficient value between the cables and cable-strut joints by Wu [20]. The descriptions for the three cases are as follows:

Case 1: The roller axle and the roller were directly in contact with each other.

Case 2: Tetrafluoroethylene (Figure 13) was added between the roller axle and the roller.

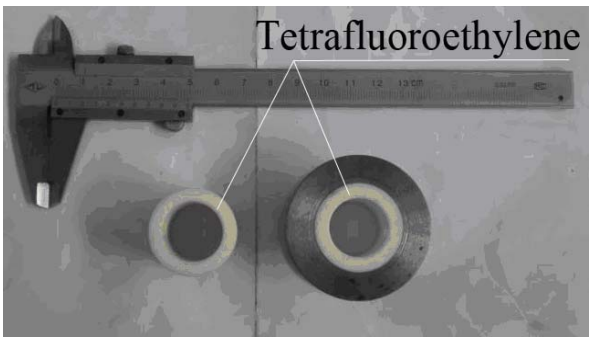

Figure 13. Tetrafluoroethylene was added in the Rolling Cable-strut Joint in Case 2

Case 3: The roller was welded to the joint body. Thus, the roller could not rotate around the roller axle, and the joint was equivalent to a traditional sliding cable-strut joint.

A galvanized fiber-cored wire rope with a diameter of 14 mm was used as the cable in this test. The angle between the two cables at both ends of the cable-strut joint was 135° (Figure 14). One side of the cable-strut joint was the loading end, and the other end was the fixed end. A hydraulic jack was adopted in this test to apply tension on the cables. The tension sensors were adopted to obtain the tension force on both sides of the cables.

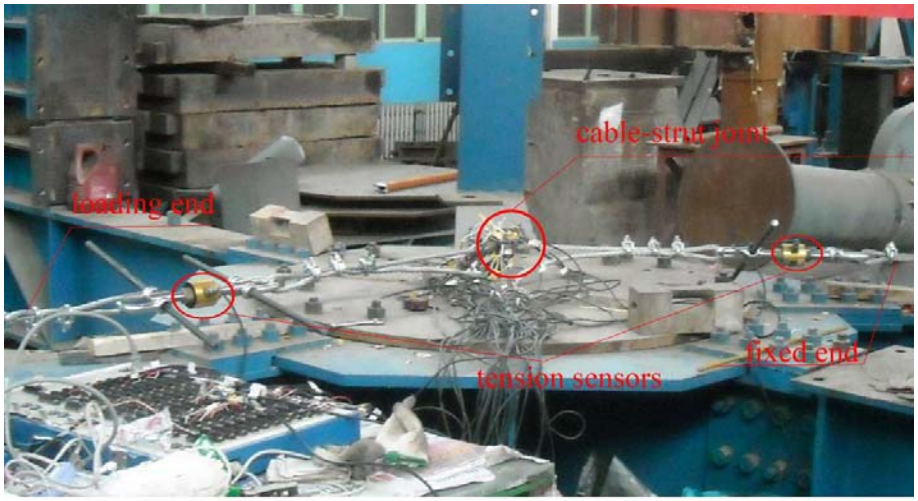

Figure 14. Test Plan

The mechanical equilibrium equation between the cable force T_1 of the fixed end and the cable force T_2 of the loading end could be written as follows:

$$T_2 = T_1 + (T_1 + T_2)\cos(\alpha/2)\mu, \tag{14}$$

where α is the angle between the two cables at both sides of the cable-strut joints, and μ is the friction coefficient between the cables and cable-strut joint. In this equation, α, T_1, and T_2 could be obtained in the test. Therefore, the friction coefficient μ could be calculated by the following equation:

$$\mu = \frac{T_2 - T_1}{(T_1 + T_2)\cos(\alpha/2)}. \tag{15}$$

Figure 15 shows the friction coefficient-cable force at the loading end curves for the three cases. The following conclusions were obtained based on Figure 15:

1) The friction coefficient of the rolling cable joint with Tetrafluoroethylene was the minimum friction coefficient.

2) The friction coefficient of the sliding cable joint was the maximum friction coefficient.

3) The overall friction coefficient increased with increasing cable forces.

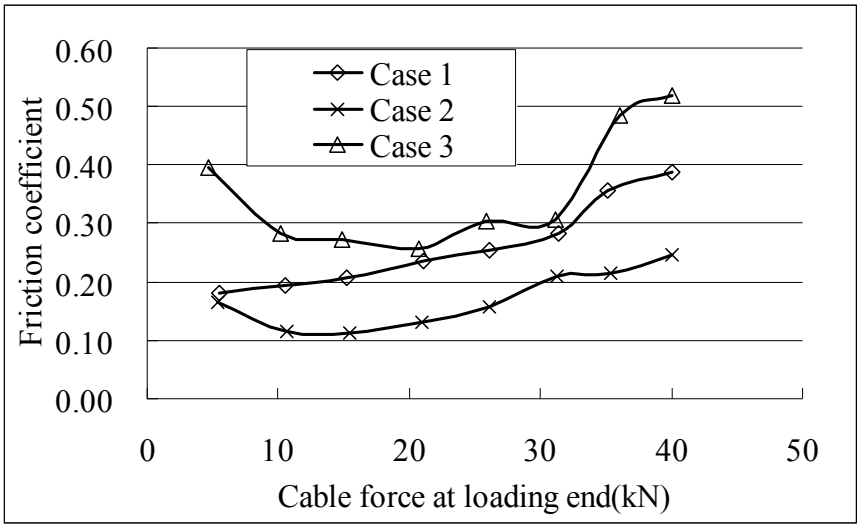

Figure 15. Friction Coefficient-cable Force at Loading End Curves

4. NUMERICAL ANALYSIS

To verify the cable-sliding criterion equation presented by author [12] and compare the results for the cable-strut joint with or without rollers, commercial finite element (FE) analysis software ANSYS was used to simulate the pre-stressing construction process of suspen-dome structures. The cable-sliding criterion equation [12], which is based on thermal expansion and contraction, is adopted to simulate cable sliding. This method required only a few APDL codes. The following presents the general procedure to simulate a pre-stressing construction that considers the sliding friction in ANSYS:

Step 1: An FE model was first established in ANSYS. Two-node LINK10 elements are adopted to simulate the hoop cable members; two-node LINK8 elements were then adopted to simulate the radial steel bars and strut members. A 3D beam element (BEAM188) was used to model members of the upper single-layer latticed shell, ring beams, and columns. The bottom of the columns was considered for pinning (Figure 16).

Step 2: Hoop cable pre-stressing were introduced by applying temperature load. A nonlinear FE analysis was then conducted to obtain the tensions of all hoop cable elements.

Step 3: If the tensions of both sides of the hoop cables of a cable-strut joint were not in equilibrium, the cable might slide around the joint. The sliding lengths around each joint could be obtained by solving the cable-sliding criterion equations [12]. On the basis of the sliding lengths around each joint, the virtual temperature of both sides of each joint could be evaluated by using the theory of thermal expansion and contraction.

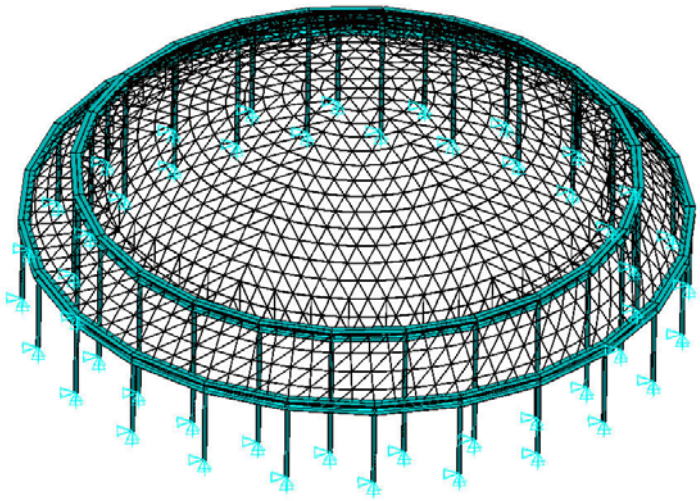

Figure 16. FE Model of the Tested Specimen

Step 4: A virtual temperature was then applied to the corresponding hoop cable elements. A re-analysis of the suspen-dome structure was conducted to obtain the tensions of all cable elements.

Step 5: Finally, the tensions of both sides of the cable-strut joint were verified. If the cable-strut joints were in equilibrium, the analysis was completed. Otherwise, Steps 3 to 5 were repeated until equilibrium was achieved.

5. RESULTS ANALYSIS

5.1 Verification of the Numerical Analysis Method

The maximum errors between the FE method and test results were calculated to verify the cable-sliding criterion equation presented in [12]. Table 1 shows the calculation results. The maximum error for Schemes 1 to 6 was 7.21%. Therefore, the numerical method was reasonable and effective for simulating a construction process that considers the sliding friction.

Table 1. Maximum Error between the Numerical and Experimental Results

Test NUM	Scheme 1	Scheme 2	Scheme 3
Maximum error	7.21%	3.88%	3.30%
Test NUM	Scheme 4	Scheme 5	Scheme 6
Maximum error	5.62%	3.30%	3.26%

5.2 Results of Schemes 1 to 3

Figures 16(a) and 16(b) provides the states of tensioning device before and after pre-stressing construction under Scheme 1, respectively. These two figures verified that the tensioning device worked well in this experiment. Figures 17(a) and 17(b) presents the states of the rolling cable-strut joint before and after pre-stressing construction under Scheme 1, respectively. These two figures verified that the rolling cable-strut joint worked well in this experiment.

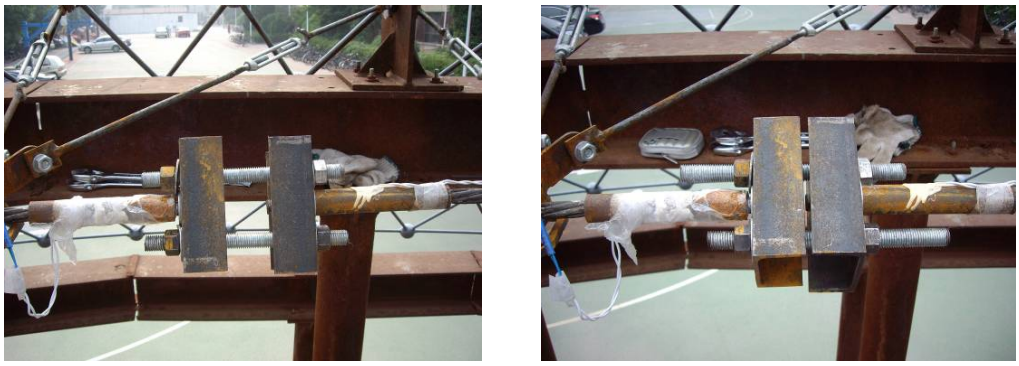

(a) Before pre-stressing construction (b) After pre-stressing construction

Figure 16. States of the tensioning device before and after pre-stressing construction.

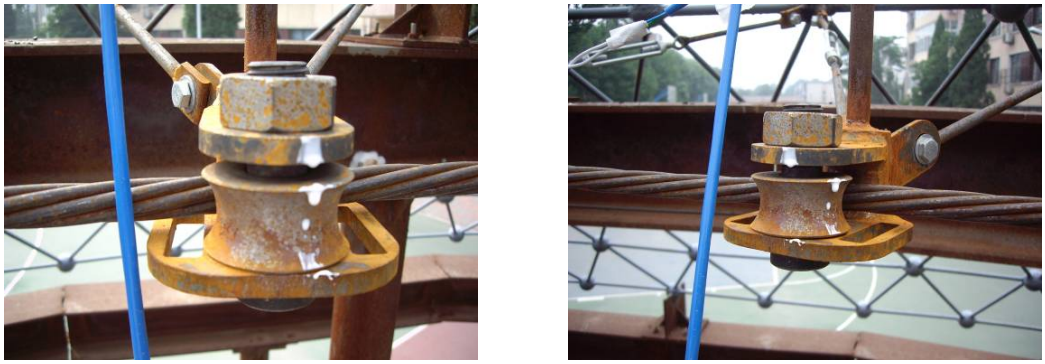

(a) Before pre-stressing construction (b) After pre-stressing construction

Figure 17. States of the Rolling Cable-strut Joint before and after Pre-stressing Construction

Figures 18 to 24 show the theoretical and experimental results from Schemes 1 to 3. The following conclusions were drawn based on the numerical and experimental results:

1) The maximum deviations from the design pre-stressing values for Schemes 1 and 2 were 55.46% and 20.90%, respectively, when the sliding cable-strut joints were adopted. When the rolling cable-strut joint were adopted, the maximum deviations from the design pre-stressing values for Schemes 1 and 2 were 38.19% and 13.44%, respectively. Compared with the sliding cable-strut joints, the maximum deviations for Schemes 1 and 2 were reduced by 31.14% and 35.69%, respectively. The average pre-stressing losses of the cable-strut joint for Schemes 2 and 3 were 2.5% and 4.2%, respectively. Therefore, the rolling cable-strut joint could effectively reduce the pre-stressing losses induced by friction.

2) The maximum deviations from the design pre-stressing values for Schemes 1 and 2 were 38.19% and 13.44%, respectively. Therefore, increasing the pre-stressing points could effectively reduce the pre-stressing losses induced by friction.

3) The maximum deviations from the design pre-stressing values for Schemes 2 and 3 were 13.44% and 2.6%, respectively. Therefore, super-tensioning could effectively reduce the pre-stressing losses induced by friction.

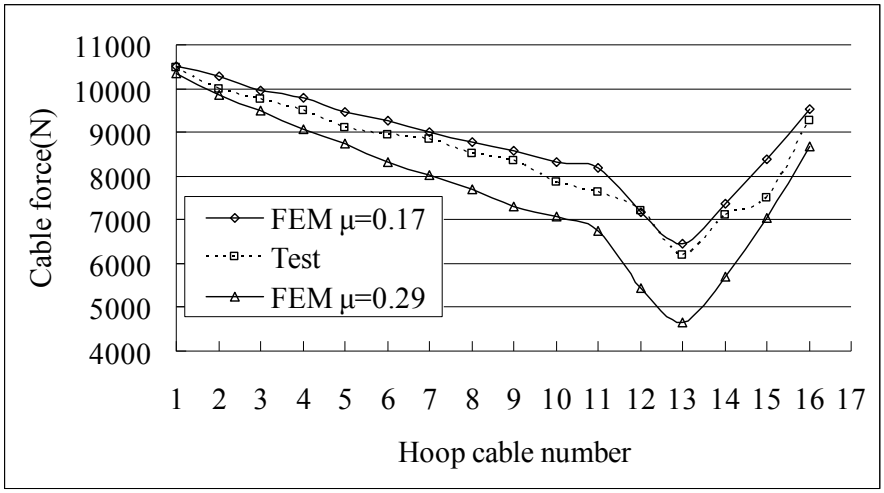

Figure 18. Hoop Cable Forces in Scheme 1

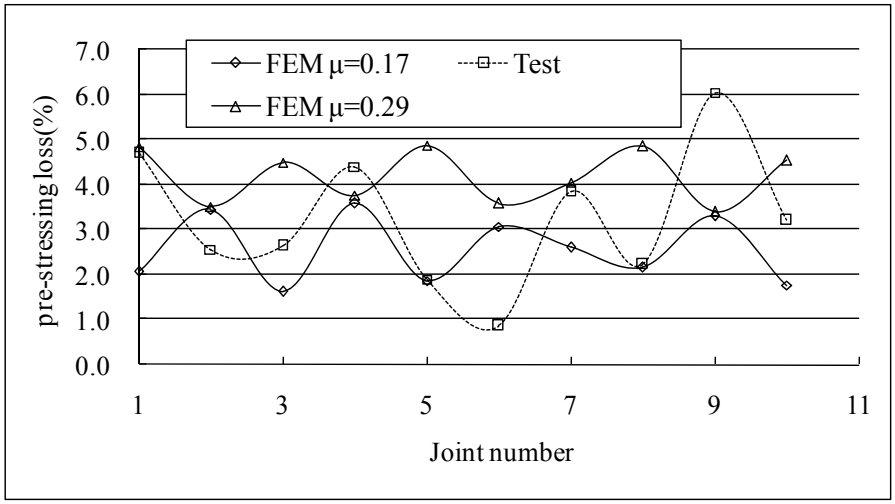

Figure 19. Pre-stressing Losses for the Cable-strut Joint in Scheme 1

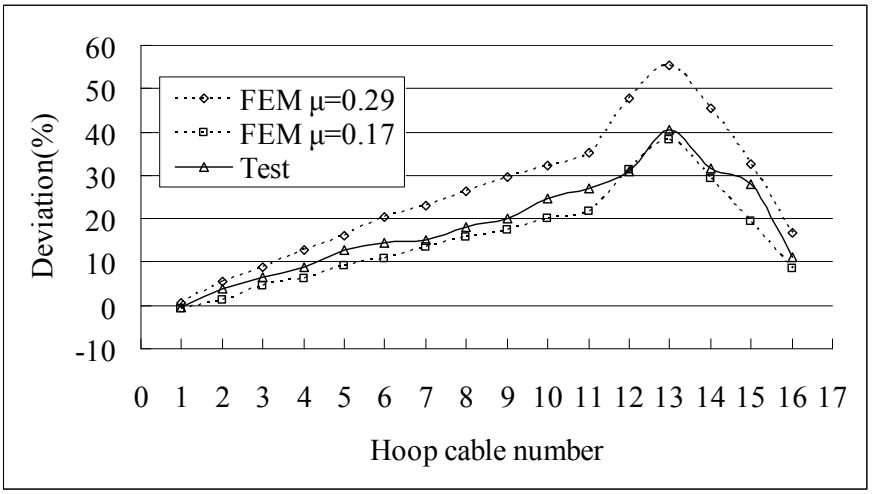

Figure 20. Deviations from the Design Pre-stressing Force in Scheme 1

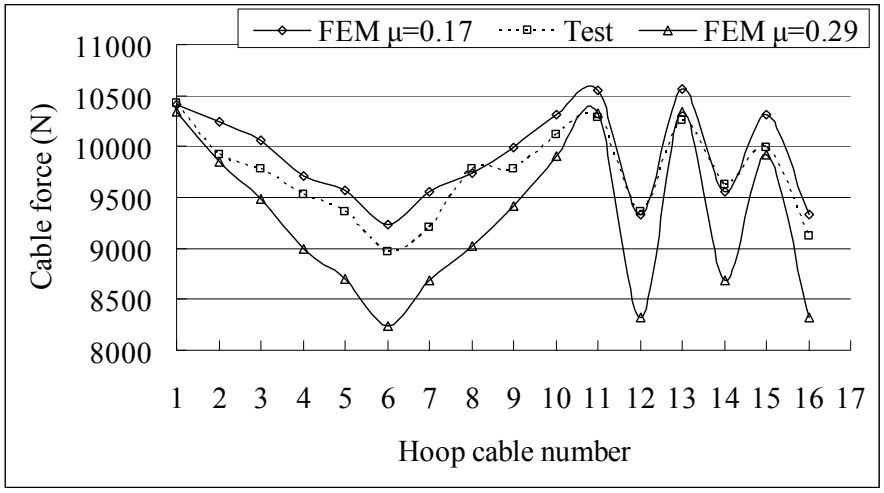

Figure 21. Hoop Cable Forces in Scheme 2

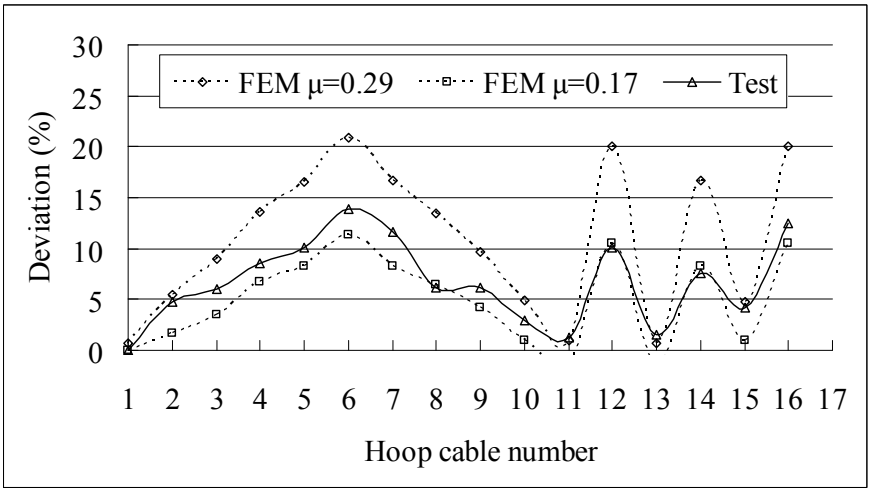

Figure 22. Deviations from the Design Pre-stressing Force in Scheme 2

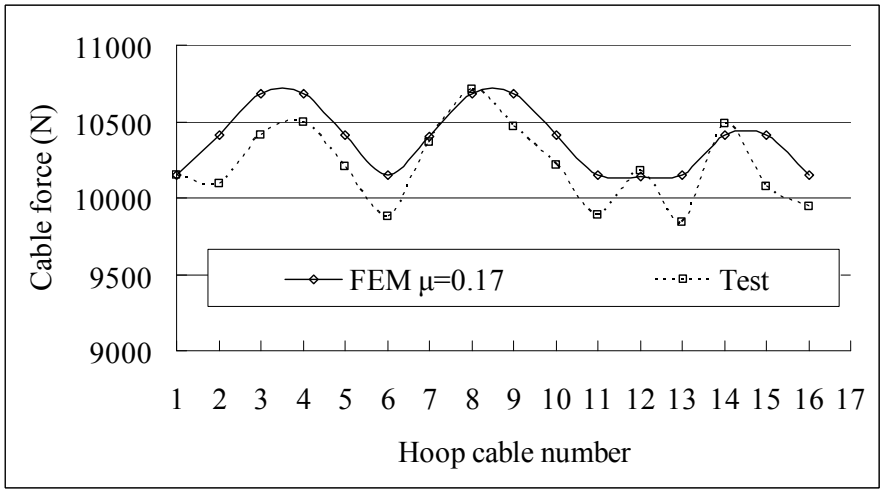

Figure 23. Hoop Cable Forces in Scheme 3

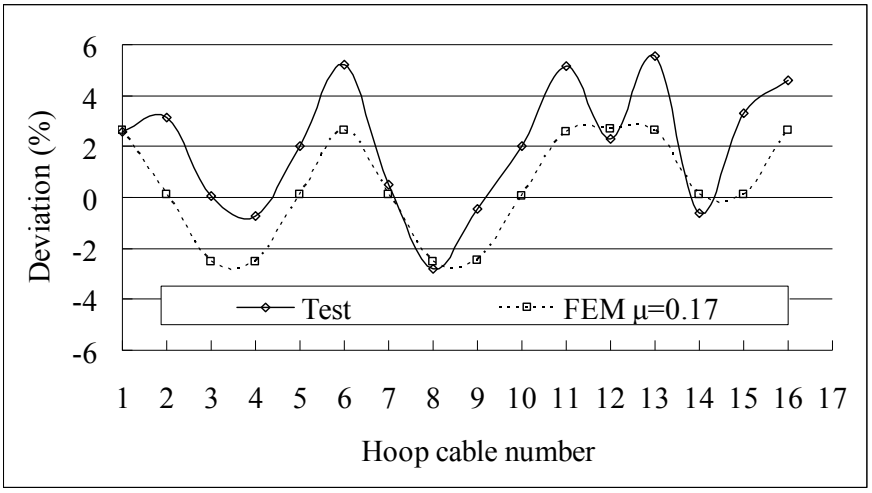

Figure 24. Deviations from the Design Pre-stressing Force in Scheme 3

5.3 Results of Scheme 4

Experimental Scheme 4 was conducted on 11 June 2011 to investigate the temperature change on the pre-stressing construction. The test specimen in this study was located outdoors and exposed to solar radiation. Therefore, the temperature of the tested model would significantly change under solar radiation during summer. The temperatures of steel tubes and cables were measured by using an infrared thermometer to provide temperature data for the numerical analysis. Ambient air temperature was also measured by using an air temperature gauge. Figure 25 shows the temperatures of the steel tube, cable, and air. The variation amplitudes of the ambient air temperature was 9 °C from 8:30 to 19:00 (Figure 25). The variation amplitudes of the steel tube and cable were 22.81 and 20.4 °C, respectively. Therefore, the temperature variation amplitude of the steel structure was significantly larger than that of the corresponding air temperature and solar radiation had a remarkable effect on steel temperature.

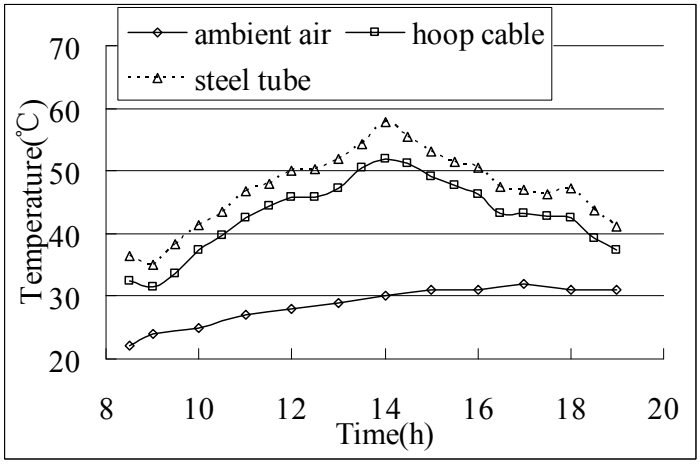

Figure 25. Temperatures of Steel Tube, Cable, and Air

In Experimental Scheme 4, the pre-stressing construction was conducted at 8:27 by using four pre-stressing points. Figure 26 shows the hoop cable forces, which were measured every 10 min after the pre-stressing construction. Based on the temperature data, maximum temperature clearly occurred at approximately 14:00. Figures 27 and 28 show the hoop cable forces at 14:00 and 19:00, respectively. The hoop cable force distribution characteristics were similar at 8:27, 14:00, and 19:00. Therefore, the hoop cable force variations for all hoop cables were similar under temperature change that considers solar radiation.

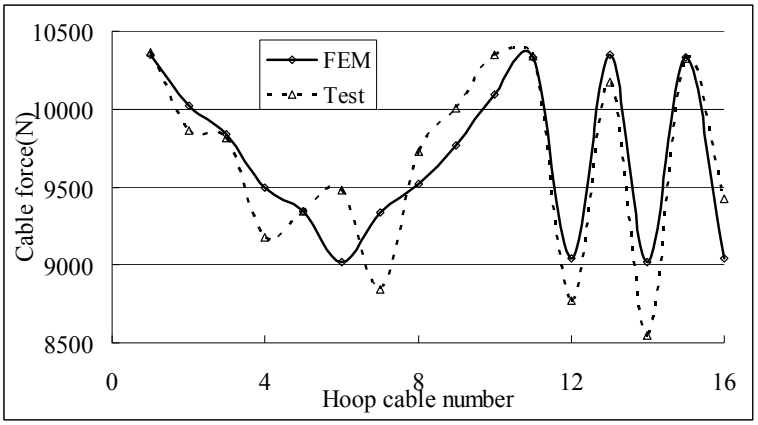

Figure 26. Hoop Cable Force at 8:27

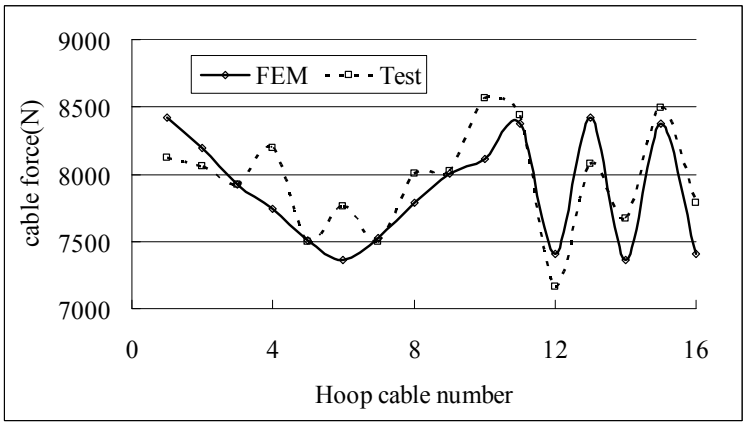

Figure 27. Hoop Cable Force at 14:00

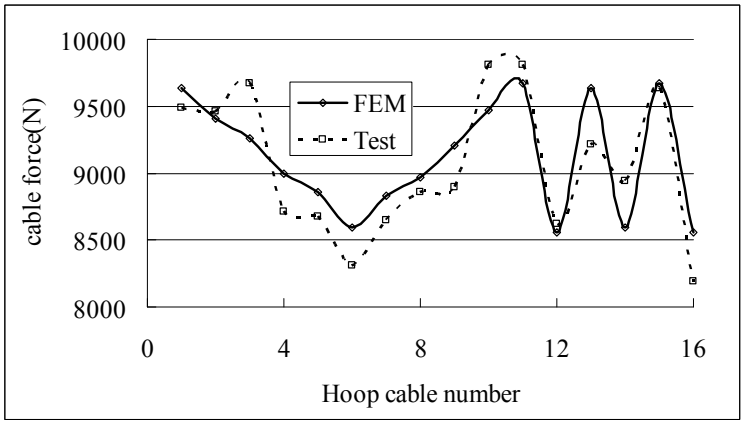

Figure 28. Hoop Cable Force at 19:00

Figures 29 and 30 show the Cable Force-time Curves for Cable Elements 1 and 6, respectively. The hoop cable force clearly increased with decreasing structural temperature or vice versa. Compared with the hoop cable forces at 8:27, the cable forces at 14:00 for Cables 1 and 6 were reduced by 21.66% and 26.75%, respectively. The aforementioned hoop cable force variations occurred within one day. The structural temperature variation during construction would be significantly larger considering the seasonal and weather changes (in terms of warm and cold current). Consequently, the hoop cable force variation would also be significantly larger. Therefore, the structural temperature change must be considered during construction.

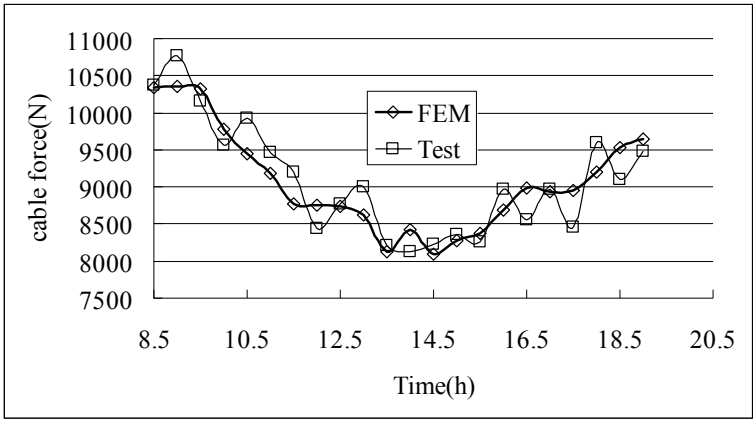

Figure 29. Cable Force-time Curve of Hoop Cable 1

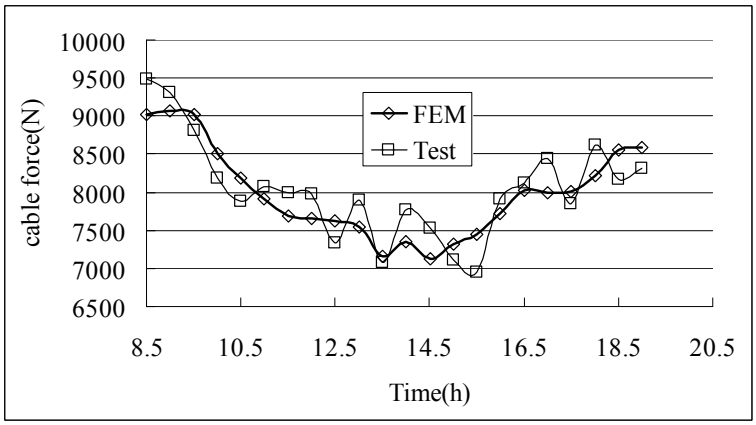

Figure 30. Cable Force-time Curve of Hoop Cable 6

5.4 Results of Scheme 5

Figure 31 shows the deviation from the design pre-stressing force in Scheme 5. Figure 31 shows that the maximum deviation from the design pre-stressing value for Scheme 5 was 11.37%. Compared with that of Scheme 2, the modified calculation presented in this paper was clearly rational.

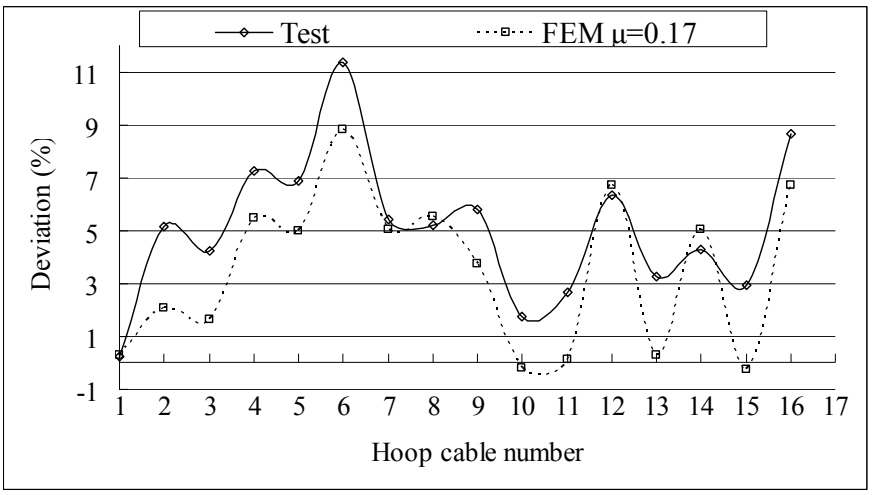

Figure 31. Deviation from the Design Pre-stressing Force in Scheme 5

5.6 Results of Scheme 6

Figure 32 shows the deviation from the design pre-stressing force in Scheme 6. Figure 32 shows that the maximum deviation from the design pre-stressing value for Scheme 6 was 5.77% by using both the temperature modified calculation and over pre-stressing construction measure. Therefore, the modified calculation presented in this paper was rational.

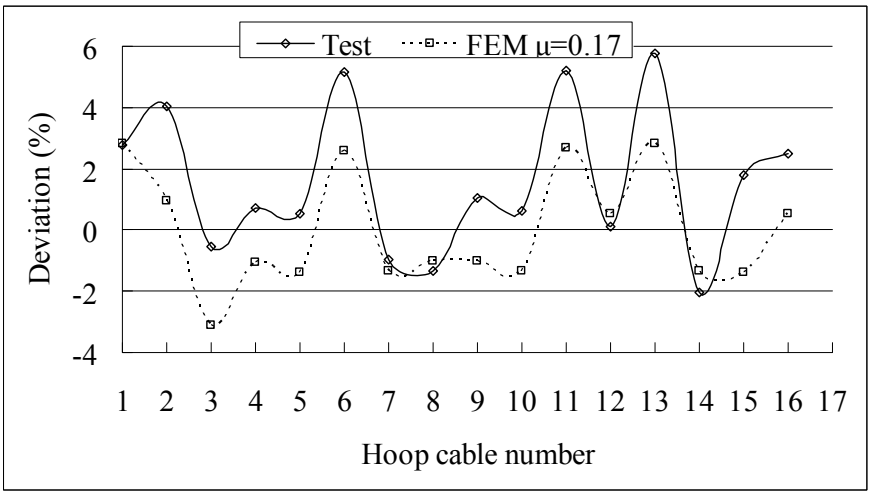

Figure 32. Deviation from the Design Pre-stressing Force in Scheme 6

6. CONCLUSIONS

This paper investigated the pre-stressing force deviation induced by sliding friction and temperature during pre-stressing construction. Five construction measurements were presented and verified by experimental study and numerical analysis to reduce the deviation and construction difficulty. The following conclusions were obtained based on the results of the experimental and numerical analysis:

1) A remarkable pre-stressing deviation from the target value was induced by temperature change and the sliding friction between hoop cables and cable-strut joints.

2) Five advanced pre-stressing construction measurements were presented to reduce the pre-stressing deviation. These measurements included increasing the pre-stressing points, over pre-stressing the construction, adoption of rolling cable-strut joints, modification of the pre-stressing construction control value that consider temperature change, and selection of the hottest time for pre-stressing construction.

3) Several critical calculation formulas were derived for the over pre-stressing construction and the modification of the pre-stressing construction control value that considers temperature change during construction.

4) A suspen-dome specimen was designed and constructed. By using this specimen, six pre-stressing construction schemes were conducted to clarify five pre-stressing construction measures. A corresponding numerical analysis was also conducted.

5) The experimental and numerical results showed that the five construction measures could effectively reduce the pre-stressing deviation.

ACKNOWLEDGEMENTS

This work was supported by the National Natural Science Foundation of China (No. 51208355), China Postdoctoral Science Foundation Funded Project (No. 2012M510751 and 2013T60253), and Tianjin Natural Science Foundation(11JCZDJC24000).

REFERENCES

[1] Mamoru Kawaguchi, Masaru Abe and Ikuo Tatemichi, "Design, Tests and Realization of ‘suspen-dome’ System", Journal of the IAAS, 1999, Vol. 40, No. 131, pp. 179-192.

[2] Chen, Z.H., Liu, H.B. and Niu, B., "Application of Suspen-dome Structures in Engineering", Industrial Construction, 2010, Vol. 40, No. 8, pp. 42-48. (In Chinese)

[3] Zhang, Z.H., Cao, Q.S., Dong, S.L. and Fu, X.Y., "Structural Design of a Practical Suspendome", Advanced Steel Construction, 2008, Vol. 4, No. 4, pp. 323-340.

[4] Liu, H.B., Chen, Z.H. and Zhou, T., "Pre-stress Loss induced by Friction in Suspen-dome Construction", Journal of Tianjin University, 2009, Vol. 42, No. 12, pp.1055-1060. (In Chinese)

[5] Liu, H.B., Chen, Z.H. and Zhou, T., "Research on the Process of Pre-stressing Construction of Suspen-dome Considering Temperature Effect", Advances in Structural Engineering, 2013, Vol. 16, No. 6, pp. 1001-1009.

[6] Liu, H.B. and Chen, Z.H., "Research on the Effect of Construction Process on the Structural Behavior of Suspen-dome Structures", Advanced Steel Construction (accepted)

[7] Wang, Y.Q., Guo, Z.X., Wang, Y.F., et al., "Structural Performance Analysis of Long Span Suspen-dome Considering Construction Factors", Building Structures, 2010, Vol. 40, No. 2, pp. 59-62. (In Chinese)

[8] Cui, X.Q. and Guo, Y.L., “Influence of Gliding Cable Joint on Mechanical Behavior of Suspend-dome Structures”, J. International Journal of Space Structures, 2004, Vol. 19, No. 3, pp. 149-154.

[9] Chen, Z.H. and Wu, Y.J., "Design of Roll Cable-strut Joint in Suspen-dome and Analysis of its Application in Whole Structure System", J. Journal of Building Structures, 2010, Supplementary Issue 1, pp. 234-240. (In Chinese)

[10] Wang, S., Zhang, G.J., Zhang, A.L., et al., "The Prestress Loss Analysis of Cable-strut Joint of the Badminton Gymnasium for 2008 Olympic Games", J. Journal of Building Structures, 2007, Vol. 28, No. 6, pp. 39-44. (In Chinese)

[11] Zhang, G.F., Dong, S.L., et al., "Research on Sliding Cable in Construction of Suspend-dome Structures", J. Journal of Zhejiang University, 2008; Vol. 42, No. 6, pp.1051-1057. (In Chinese)

[12] Liu, H.B., Chen, Z.H., Wang, X.D. and Zhou, T., "Establishing and Application of Cable-sliding Criterion Equation", J. Advanced Steel Construction, 2011, Vol. 7, No. 2, pp. 131-143.

[13] Kitipornchai, S., Kang, W.J., Lam, H.F., et al., "Factors Affecting the Design and Construction of Lamella Suspen-dome Systems", J. Journal of Constructional Steel Research, 2005, Vol. 61, No. 6, 764-785.

[14] Kang, W.J., Chen, Z.H., Lam, H.F., et al, "Analysis and Design of the General and Outmost-ring Stiffed Suspen-dome Structures", J. Engineering Structures, 2003, Vol. 25, No. 13, pp. 1685-1695.

[15] Cao, Q.S. and Zhang, Z.H., "A Simplified Strategy for Force Finding Analysis of Suspendomes", J. Engineering Structures, 2010, Vol. 32, No. 1, pp. 306-310.

[16] Liu, H.J., Luo, Y.F. and Yang, L.F., "Construction Parameters and Process Simulation Method of Suspen-domes", J. Journal of Civil, Architectural & Environmental Engineering, 2010, Vol. 32, No. 5, pp. 142-148. (In Chinese)

[17] Zhang, A.L., Liu, X.C., Wang, D.M., et al., "Static Experimental Study on the Model of the Suspend-dome of the Badminton Gymnasium for 2008 Olympic Games", Journal of Building Structures, 2007, Vol. 28, No. 6, pp. 58-67. (In Chinese)

[18] Li, K.N. and Huang, D.H., "Static Behavior of Kiewitt6 Suspendome" J. Structural Engineering and Mechanics, 2011, Vol. 37, No. 3, pp. 309-320.

[19] Liu, H.B. and Chen, Z.H., "Structural Behavior of the Suspen-dome Structures and the Cable Dome Structures with Sliding Cable Joints", J. Structural Engineering and Mechanics, 2012, Vol. 43, No. 1, pp. 53-70.

[20] Wu, Y.J., "Analysis of Sliding Cable Element and Node", D. Tianjin, Tianjin University, 2010.

RESEARCH ON STATIC PROPERTIES AND STABILITY OF HIGH-RISE TUBULAR 3D PARKING STRUCTURE WITH HOOP STORIES

Yongjun He [1, *], Xiaohua Liu [1, 2] and Xuhong Zhou [1, 3]

[1] *College of Civil Engineering, Hunan University, Changsha, 410082, PR China*
[2] *Xi'an Architectural Design-research Institute, Xi'an, 710043, China*
[3] *Chongqing University, Chongqing 400044, China*
**(Corresponding author: E-mail: hyj0087@163.com)*

Received: 23 January 2013; Revised: 28 October 2013; Accepted: 20 December 2013

ABSTRACT: A new structural arrangement style of high-rise tubular 3D parking structure is presented, which is to set hoop stories like bamboo knots at the proper levels along the height, and the optimal arrangement principle of hoop stories is analyzed. The static properties and stability of the structures with different arrangement schemes of hoop stories are compared. Results indicate that, the lateral stiffness of the structure with hoop stories set according to the equal stability and equal drift principle is remarkably improved; the storey drift becomes more uniform, which benefits the stable operation of hoisting machines; also, the sudden change of the internal forces of columns is relatively moderate and the structural overturning resistance is enhanced. Finally, the parametric analyses on static properties and stability of the structures with optimal arrangement of hoop stories are studied in detail.

Keywords: High-rise 3D parking structure, Hoop stories, Optimal arrangement, Static properties, Stability

1. INTRODUCTION

The limited urban land resource determines that the simple plane parking in city will inevitably evolve into modern three-dimensional (3D) parking. Among numerous 3D parking structures, the vertical lifting 3D parking structure has become the priority to solve the parking problem in metropolitan area. It fully utilizes limited space to bring the maximum benefits to the customers and strives for more parking spaces by small space. Moreover, it has high speed and low noise, which meets the city environmental protection requirements (Amott [1], Amélie and Bryan [2] and Eduardo et al. [3]).

The high-rise vertical lifting tubular 3D parking structure is very similar to bamboo in its macroscopic structure type, and both are tubular structure with large slenderness ratio. The distinction is that bamboo has bamboo knots with different intervals along its height. However, the existing tubular parking structures have not transverse reinforcing components like bamboo knots. Experiments (Yu and Chung [4], Tommy and Cui [5] and Khosrow [6]) show that natural bamboo has the excellent overall stability and local buckling hardly appears. Additionally, the bending, shearing and compression resistance of bamboo can be improved by 23%, 19%, and 7%, respectively, for the existence of bamboo knots. The main reason is that bamboo knots can strengthen the integrity of bamboo, which is beneficial to resisting the shear. On the other hand, bamboo knots are analogous to hinges, which divide 'long rod' into 'short rod' and dramatically decrease the slenderness ratio of bamboo. Therefore, the probability of buckling is effectively reduced. Since bionics was established as a new subject, the structural design in theory and practice has continuously obtained inspiration from biosphere (Ma et al. [7], Karthikeyan et al. [8] and Zhao et al. [9]). The 88-storey twin structure in Malaysia and the wings of large civil aircrafts are both typical examples about the successful practice of bamboo knot bionics in structural design.

Based on the superior behavior of bamboo, and considering the similarity of the vertical lifting 3D parking structures with bamboo in the aspects of structural type and load feature, a new structural arrangement style of 3D parking structure is presented in this paper, which is to set hoop stories like bamboo knots at its proper levels along the height. Then, the static properties and stability of the structures with different arrangement schemes of hoop stories are compared in detail. Finally, based on parametric analyses, the influences of the bracing stiffness in hoop stories, storey height, and the linear stiffness ratio of beam to column on static properties and stability of the structure with optimal hoop storey arrangement scheme are studied systematically.

2. ARRANGEMENT SCHEME OF HOOP STORIES OF THE VERTICAL LIFTING TUBULAR 3D PARKING STRUCTURE

2.1 Arrangement Principle of Hoop Stories

The parking function of vertical lifting 3D parking structure makes it be a new structural system different from the ordinary housing structure. Actually, it is a quadrilateral tubular structure consisting of four planar frames along the periphery with few internal horizontal members as shown in Figure 1 (He and Zhou [10]). There are not filled walls and floor slabs. And its storey height is relatively small. All these characters weaken the concept of 'structural storey'. The constraint of beam to column is also weakened, which results in the increase of slenderness ratio of columns. Some columns even can be regarded as long vertical cantilever throughout the structure on extreme condition. Hence, for this kind of tall and slender 3D parking structure, the overall stability may become the governing factor in design like the structural lateral displacement. Therefore, it is important to present a reasonable structural arrangement method to improve the structural behavior and meet its functional requirement.

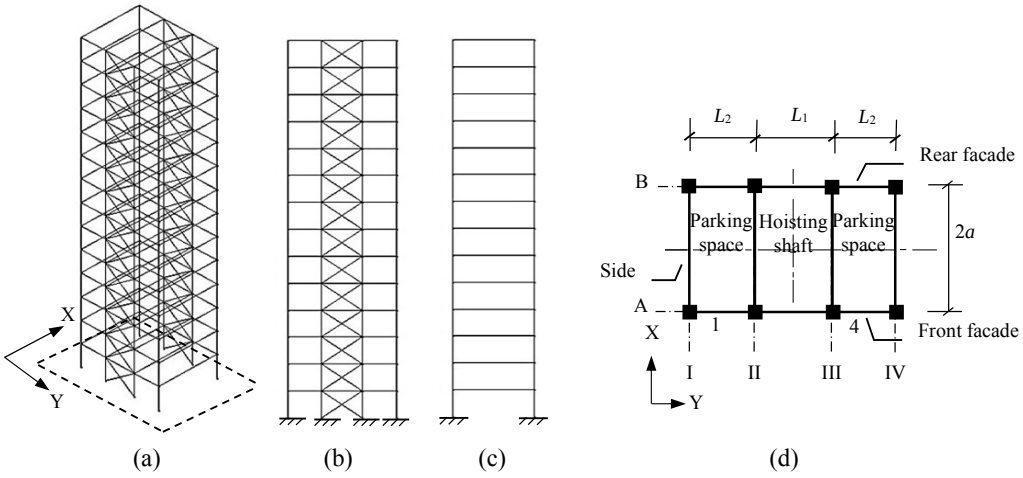

Figure 1. Conventional Highrise Vertical Lifting Tubular 3D Parking Structure:
(a) Three-dimensional Figure; (b) Front/Rear Frame; (c) Side Frame; (d) Planar Layout

Based on the inspiration from bamboo, the author presents a new structural arrangement style of 3D parking structure, which is to set hoop stories like bamboo knots at its proper levels along the height. As shown in Figure 2, X-shape braces with appropriate stiffness are arranged in the peripheral frames at a specific storey. Also, horizontal X-shape braces are set on the upper and lower parking levels except the hoisting shaft area. Therefore a hoop of the structure is formed, and thus this strengthened storey is named hoop storey. The hoop stories do not occupy inner space of the structure and have no influence on normal hoisting and parking function.

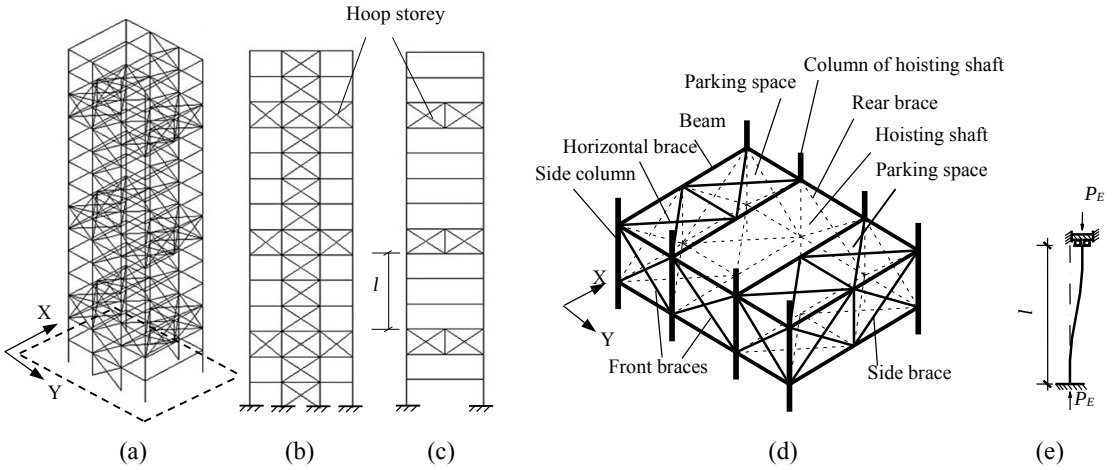

Figure 2. High-rise Vertical Lifting Tubular 3D Parking Structure with Hoop Stories: (a) Three-dimensional Figure; (b) Front/rear Frame; (c) Side Frame; (d) Schematic Diagram of a Hoop Storey; (e) Model of an Equivalent Short Column between Two Adjacent Hoop Stories

Obviously, the hoop stories in the tubular 3D parking structure essentially differ from the horizontal strengthened stories in traditional high-rise structure in the structural arrangement style and mechanism. The formation of traditional strengthened stories is usually setting horizontal outriggers with large stiffness between the inner tube and outer frame using the equipment, refuge or transfer stories. These outriggers will make the inner and outer tubes work cooperatively, and cause the redistribution of internal forces as well as the improvement of lateral stiffness finally. Generally, the arrangement of strengthened stories follows the principle of minimizing the top lateral displacement. However, the optimal layout of hoop stories in the tubular 3D parking is based on the equal stability and equal drift principle. That is, the stabilities of various columns between any two adjacent hoop stories are identical and the drifts between any two adjacent hoop stories are also identical. The purpose is to reduce the lateral displacement and improve overall stability simultaneously by strengthening the structural integrity and reducing the slenderness ratios of columns.

The mechanism as well as determination of the optimal arrangement intervals of hoop stories in the high-rise tubular 3D parking structure can be interpreted as follows. For convenience, the side planar frame in the structure as shown in Figure 2(c) is taken as the analytical model. Since the equivalent linear stiffness of hoop storey is greatly larger than that of a column, the hoop stories can be regarded as rigid beam, which completely constrains the rotation of ends of the columns connected with the hoop stories. Also, compared with columns, the linear stiffness of beams in the common stories is so small that their restraint to columns can be ignored. Considering the lateral displacement of the frame, columns between two adjacent hoop stories can be approximately regarded as strut that the lower end is fixed and the upper one can shift but not rotate. Economical and rational design for framework should ensure that all columns buckle simultaneously (Li [11]). Actually, the overall stability of framework has equivalence relationship with the stability of any column between two adjacent hoop stories in the framework on this condition. Therefore, the overall stability analysis of the structure can eventually be transformed into stability analysis of the equivalent short columns between two adjacent hoop stories.

Under vertical loads, the axial force of various columns in the *i*-th storey of the structure can be calculated as

$$N_i = \sum_{j=i+1}^{n} \mathrm{G}_j \Big/ m_i \tag{1}$$

where, $\sum_{j=i+1}^{n} \mathrm{G}_j$ is the sum of vertical gravitational loads above the *i*-th storey, including the self weight of structural components and vehicle loads; m_i is the number of columns in the *i*-th storey; and n is the number of stories.

The Euler critical load of one equivalent short column between two adjacent hoop stories as shown in Figures 2(c) and (e) can be expressed as

$$P_E = \pi^2 E I_e \Big/ (\eta l)^2 \tag{2}$$

in which, I_e, l, and η are the cross sectional moment of inertia, length, and calculated length coefficient of the equivalent short column, respectively. The length of the equivalent short column is the net height between two adjacent hoop stories (excluding the hoop stories) as shown in Figure 2(c). Also, since the columns between two adjacent hoop stories can be approximately regarded as strut that the lower end is fixed and the upper one can shift but not rotate as mentioned above, and the calculated length coefficient of this kind of strut as shown Figure 2(e) is apparently 1.0, so here $\eta = 1.0$.

Based on the equivalent axial forces on the tops of various equivalent short columns, various hoop-storey intervals, namely the lengths of equivalent short columns, are adjusted according to the equal stability principle, that is, all the equivalent short columns buckle simultaneously. The preliminary arrangement scheme of hoop stories can be obtained by tentative calculation.

To ensure various members be stressed as uniformly as possible, the optimal arrangement scheme of hoop stories should be selected from the preliminary ones according to the equal drift principle, that is, the drifts of any two adjacent hoop stories should be as identical as possible. Since various hoop stories are regarded as rigid beams and have no bending deformation, the drift of two adjacent hoop stories Δ_i completely comes from the deformation of columns for the horizontal loads applied on various stories. According to structural mechanics, Δ_i can be calculated as

$$\Delta_i = l^3 V_i \Big/ 12 E I_i \tag{3}$$

where, $V_i = \sum_{j=i}^{n} F_j$ is the sum of the horizontal loads above the hoop storey; $I_i = \sum_{1}^{m} I_e$ is the sum of the cross sectional moments of inertia of various equivalent short columns.

As above mentioned, the axial force and the Euler critical load of one equivalent short column can be obtained from Eqs. 1 and 2, respectively, and the drifts of equivalent short columns can be calculated by Eq. 3. Then we can adjust the intervals of the two adjacent hoop stories, namely, the lengths of the equivalent short columns, to meet the equal stability and equal drift requirement and get the optimal arrangement of hoop stories. However, it is difficult to find a scheme that can meet the equal stability and equal drift requirement at the same time due to the indivisibility of the number of stories. Therefore, we can just adjust the intervals of hoop stories to minimize the difference between the axial force and the Euler critical load, as well as that of their drifts as

possible. And a set of intervals most close to the accurate solution can be obtained. Based on this method, a Matlab program is developed in this paper to iterate and calculate the optimal arrangement scheme of hoop stories. And for the tubular 3D parking structures with different numbers of stories commonly used in practical engineering, the optimal intervals of hoop stories from bottom to top of the structures are obtained as shown in Table 1.

Table 1. The Optimal Arrangement Schemes of Hoop Stories of the Structures with Different Numbers of Stories

Total number of stories	11	12	13	14	15	16	17	18	19	20
Intervals of hoop stories	1, 2, 3	1, 2, 3	2, 3, 4	2, 3, 4	2, 3, 5	2, 3, 5	3, 4, 5	3, 4, 5	3, 4, 6	3, 5, 7

2.2 Comparison on Static Properties of the Structures with Different Arrangements of Hoop Stories

2.2.1 Analytical models

Taking the 14-storey structures as examples, the static properties of the 3D parking structures with different arrangement schemes of hoop stories such as K000, K234, K135, and K333, respectively, are compared. The intervals of hoop stories of various schemes are described in Table 2. The K234 is the optimal arrangement scheme as described in Table 1.

Table 2. Different Arrangement Schemes of Hoop Stories of the 14-storey Structures

Arrangement scheme	K000	K234	K135	K333
Intervals of hoop stories	Without hoop stories stories	2, 3, 4	1, 3, 5	3, 3, 3

The span along X direction of the structure is 6.0m and those of various bays along Y direction are 2.5, 3.0, and 2.5m, respectively. The storey height is taken as 2.2m. Additionally, the components are assumed to be made of Q235 steel (Yield Strength 235 MPa), and the modulus of elasticity of steel is 2.1×10^5N/m^2. The columns and beams are made of H-shaped sections H-250×300×8×10 (in which, 250, 300, 8, and 10 are the height of the cross section, width of the flange, thickness of the web, and the thickness of the flange, respectively; the unit is mm; and similarly hereinafter) and H-100×100×6×8, respectively. The strong axis of the H-section columns is parallel to the longitudinal direction(Y-axis) of the building. And the braces are circular steel tube $\phi 152\times5$. The horizontal concentrated loads of each 1kN are applied on nodes of the front facade of the structure to proximately simulate wind load. Meanwhile, the vertical concentrated loads of each 8kN are exerted on column nodes of the structure to denote the vehicle load and self weight of the structure, hoisting machines and other affiliated equipments (Hyo and Jong [12]).

Finite element models of the structures are established by APDL language based on ANSYS software. All the beams and columns are simulated by BEAM188 element, while the braces are simulated by LINK8 element (Salemi *et al*. [13]). The influence of geometric nonlinearity is taken into consideration in the analysis of this kind of tall and slender structures.

2.2.2 Lateral displacement and storey drift

The lateral displacement and storey drift (along the transversal direction) curves of various models are displayed in Figures 3 and 4, respectively. It can be seen from Figure 3 that the lateral displacements of the structures with hoop stories are only about 1/5 of that of the structure without hoop stories. This indicates that the effect of hoop stories on confining the structural lateral

displacement is remarkable. Additionally, the top lateral displacement of the model K234 with hoop stories arranged according to the equal stability and equal drift principle decreases by the greatest degree and the sudden change of the lateral displacement along the structural height is not notable. Although the lateral displacements of models K333 and K135 are also reduced effectively for the arrangement of hoop stories, but there exists sudden change at the lower and upper parts of the structures, respectively. It can be further seen from Figure 4 that, the storey drifts of the structures with hoop stories fluctuate within small range and the fluctuation amplitudes are greatly less than that of the structure without hoop stories. Also, the fluctuation amplitude of storey drift of the model K234 basically keeps constant and is less than those of the models K333 and K135. This is in conformity with the equal lateral displacement principle and beneficial to the stable operation of hosting machine in the vertical lifting 3D parking structure.

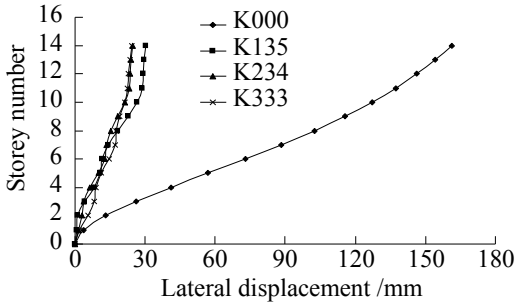

Figure 3. Lateral Displacements of the Structures with Different Arrangement Schemes of Hoop Stories

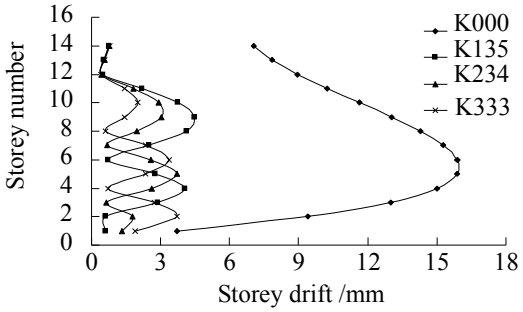

Figure 4. Storey Drifts of the Structures with Different Arrangement Schemes of Hoop Stories

2.2.3 Internal force distribution of columns

The columns with largest internal forces on the leeward side are taken to analyze. The influence law of hoop stories on distribution of internal forces is studied, and the mechanism of decrease in structural lateral displacement is accordingly investigated. The variation curves of axial force, shear force and bending moment of columns of various structures along the structural height are displayed in Figures 5, 6, and 7, respectively. From the figures, some information can be obtained as follows.

1) The axial force of columns in the scheme K000 almost linearly decreases along the structural height, while sudden change in those of the structures with hoop stories appears near the hoop stories. Also, in comparison with the scheme K000, the axial forces of columns of the schemes K135, K234 and K333 increase by almost 12%, 15%, and 19%, respectively. Actually, the hoop stories can be regarded as rigid beams between the columns, which powerfully strengthen the relation of the columns. The shear force can thus be transformed into axial force of columns sufficiently when horizontal load is applied on the structure. This will result in increase of the axial force of columns. Further, the increased axial force of columns effectively forms into the torque of couple, which can resist the overturning moment caused by the horizontal load. Thus, the lateral displacement can be remarkably reduced and the structural overturning resistance is improved accordingly.

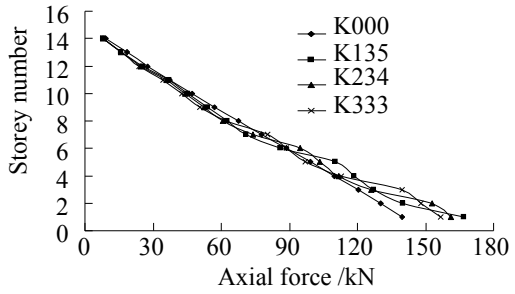

Figure 5. Axial Forces of Columns of the Structures with Different Arrangement Schemes of Hoop Stories

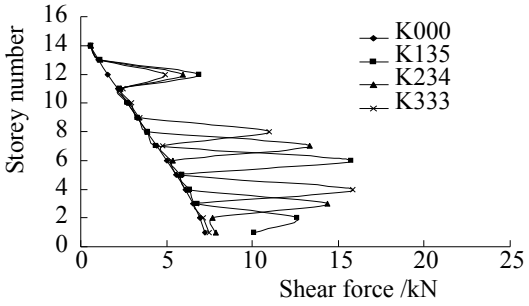

Figure 6. Shear Forces of Columns of the Structures with Different Arrangement Schemes of Hoop Stories

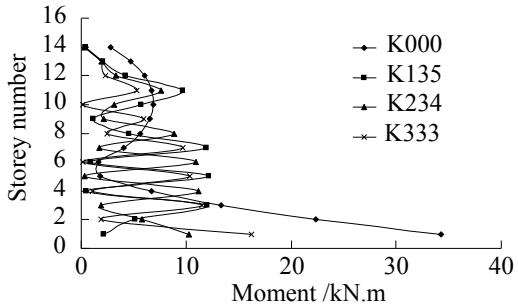

Figure 7. Bending Moments of Columns of the Structures with Different Arrangement Schemes of Hoop Stories

2) Sudden increase in shear forces of columns occurs at hoop stories, but change of those at the adjacent stories of hoop stories is not notable. The reason is that, the structural lateral displacement is continuous along the height but there exists sudden increase in shear stiffness of the columns in the hoop stories for the arrangement of cross braces, which results in the shear force concentration of columns in these stories. The strengthening measure of shear resistance should be considered at the column ends connected to the hoop stories. Additionally, the sudden change in shear force of the scheme K234 is minimum, which indicates that the rational arrangement of hoop stories is of benefit to moderating the sudden change of shear force.

3) The bending moment of bottom columns of scheme K000 is greatly larger than those of the schemes with hoop stories. Particularly, the bending moment of columns of the scheme K234 fluctuates along the height within the smallest range. Conclusions can be drawn that the hoop stories set with reasonable intervals in the structure will weaken the moment concentration at the bottom of the structure and make the distribution of moment be more uniform. The main reason is that, the arrangement of hoop stories leads to the increase in axial force of the columns, which partly provides the overturn-resisting moment and effectively reduces the bending moment of columns. On the other hand, since the structural lateral displacement decreases for the existence of hoop stories, the additional moment caused by second-order effect also decreases consequently.

2.3 Comparison in Stability of the Structures with Different Arrangement Schemes of Hoop Stories

2.3.1 Linear buckling analysis

Although linear buckling analysis cannot accurately obtain the ultimate bearing capacity, it can preliminarily reflects the structural overall stability and the calculation process is simple. Additionally, linear buckling mode is usually adopted as the initial imperfection distribution pattern in the imperfection sensitivity analysis (Zhao *et al*. [14]). Therefore, it is necessary to do linear buckling analysis before the nonlinear buckling analysis. As the key points of research, the structural first order buckling load and mode are discussed in this section. The values of various parameters are identical with those in *Section 2.2.1*. The first-order linear buckling loads of the structures with different arrangement schemes of hoop stories are summarized in Table 3.

Table 3. Linear Buckling Loads of the Structures with Different Arrangement Schemes of Hoop Stories

Arrangement scheme	K000	K135	K234	K333
Buckling load /kN	89.7	317.4	390.3	351.5

It can be seen from Table 3 that the buckling loads of the structures with hoop stories are markedly larger than that of the structure without hoop stories, which indicates that the hoop stories can notably improve the structural overall stability as expected. Moreover, the eminent behavior of the model K234 with optimal arrangement of hoop stories shows the importance of rational arrangement intervals of hoop stories by equal stability and equal drift principle.

The first order bucking modes of the structures with four different arrangement schemes of hoop stories are displayed in Figure 8. Obviously, the bucking mode of the model K000 presents inclination as a whole towards the transverse (X) direction, so the governing direction is transversal on the linear buckling of the building. For the model K234, there exists remarkable drift between the first and second hoop stories along the transverse direction, which leads to the structural overall buckling. The storey drifts at the upper and lower parts of the structure is not remarkable. Similarly, the overall buckling of the models K135 and K333 is also caused by the excessive storey drifts between two adjacent hoop stories at different parts of the structures. Therefore, the hoop stories have strong restriction effect on the columns. Actually, this kind of high-rise tubular structure can be regarded as a vertical cantilever fixed to the ground, and the whole structure is divided into several short columns for the existence of the hoop stories. And the structural overall stability depends on the stability of equivalent short columns between adjacent hoop stories. This results in remarkable increase of the structural overall stability bearing capacity.

2.3.2 Nonlinear stability analysis

Linear buckling analysis cannot reflect the influence of initial imperfection and usually overestimates the structural stability bearing capacity. Therefore, it is necessary to do structural nonlinear stability analysis. In this paper, an incremental-iterative method based on the Newton-Raphson method combined with constant arc length is adopted to do nonlinear stability analysis by tracking the equilibrium path (Widjaja [15]). The values of various parameters and load pattern are identical with those in *Section 2.2.1*. For this kind of tall and slender structure, only the geometric nonlinearity is taken into consideration. The influence of geometric imperfection is also considered and the imperfection amplitude of 30mm (about 1/1000 of the structural height) is

preliminarily adopted. Here, the first order linear buckling mode is adopted as the geometric imperfection distribution pattern, and the geometric imperfection is along the transversal direction of the structure. The load-displacement curves are displayed in Figure 9, in which, the load is the vertical concentrated load exerted on each column node, and the displacement is the lateral displacement of the top of the structure along the transverse direction. In the process of the structural displacement increasing with increase of the load exerted on the structure, if a little increase of load results in rapid increase of structural displacement and the structure is about to fail, the load at this moment is defined as the structural ultimate load in this paper. Evidently, the ultimate load implies the structural stability bearing capacity.

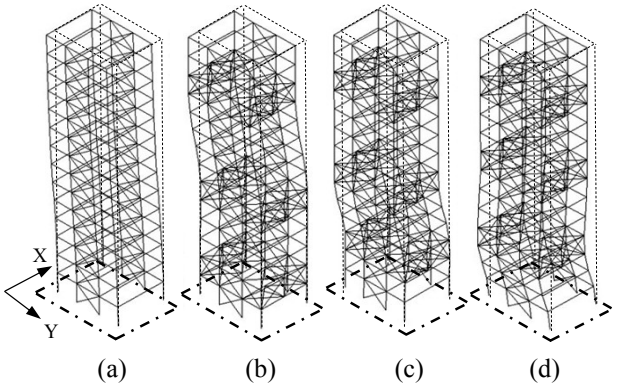

Figure 8. Buckling Modes of the Structures with Different Arrangement Schemes of Loop Stories: (a) K000; (b) K135; (c) K234; (d) K333

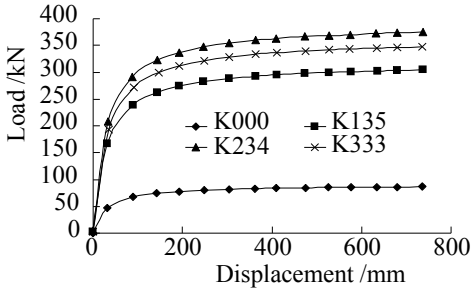

Figure 9. Load-displacement Curves of the Structures with Different Arrangement Schemes of Loop Stories

It can be seen that the stability bearing capacity of model K234 is obviously larger than those of the others. This is consistent with the result of linear buckling analysis and further demonstrates the superiority of hoop stories set according to the equal stability and equal drift principle. Additionally, as shown in Figure 9 and Table 3, the nonlinear stability bearing capacity is remarkably less than the linear result, so the geometrically nonlinear effect cannot be ignored in stability analysis of this kind of structure.

3. PARAMETRIC ANALYSIS OF STATIC PROPERTIES

In Section 2, the static property and stability of the high-rise tubular 3D parking structures with different arrangement schemes of hoop stories are compared in detail. And the rationality of the optimal arrangement principle of hoop stories is thus verified. To further obtain the reasonable design values of various parameters of the structure with optimal arrangement of hoop stories, the influence of the parameters on structural static properties, including the maximum lateral displacement, story drift angle, and peak stress, are investigated, respectively. The 14-storey 3D parking structure with optimal arrangement scheme of hoop stories, namely the model K234 as described in Table 1, is taken to analyze. And the geometrical nonlinearity is considered.

3.1 Influence of the Cross Section of the Side Braces

Let the cross section of front/rear braces be $\phi 121\times 4$, and different cross sections of the side braces such as $\phi 73\times 3$, $\phi 89\times 4$, $\phi 102\times 4$, $\phi 121\times 4$, $\phi 152\times 5$, $\phi 168\times 8$, as well as $\phi 203\times 9$ are considered, respectively. The other parameters and loads are identical with those described in *Section 2.2.1*. The static analytical results are summarized in Table 4. It can be seen that the maximum lateral

displacement, story drift angle (along the transversal direction, and similarly hereinafter) and peak stress notably decrease with increase of the cross section of the side braces within a certain range. However, the further increase of the cross section almost has no remarkable effect on drop of these static indices when it reaches to a certain value. Therefore, there exists a rational upper limit for the cross section of side braces, and a hoop storey can be approximately regarded as a rigid beam in this limit case. For the model in this section, the cross section of the side braces in the hoop stories should not exceed $\phi 152\times 5$, and the further increase after this value is not economical.

Table 4. Static indices of the structures with different cross sections of side braces

Side braces		Maximum lateral displacement (Transversal) /mm	Decline rate of maximum lateral displacement	Maximum storey drift angle (Transversal) /$\times 10^{-3}$rad	Decline rate of maximum storey drift angle	Peak stress /MPa	Decline rate of peak stress
Cross section	Cross-sectional area /mm^2						
$\phi 73\times 3$	337	36.3	79.4%	2.21	71.7%	39.14	39.9%
$\phi 89\times 4$	546	30.8	82.5%	1.92	75.4%	37.43	42.5%
$\phi 102\times 4$	628	29.5	83.3%	1.85	76.3%	37.02	43.1%
$\phi 121\times 4$	747	28.1	84.1%	1.78	77.2%	36.57	43.8%
$\phi 152\times 5$	1174	25.2	85.7%	1.62	79.2%	35.61	45.2%
$\phi 168\times 8$	2060	22.9	87.0%	1.49	80.9%	34.82	46.5%
$\phi 203\times 9$	2805	22.0	87.5%	1.33	95.5%	34.47	47.1%
Without side braces		176.1	-	7.81	-	65.04	-

PS: The decline rate of maximum lateral displacement is the percentage decrease of the maximum lateral displacement of the structure with side braces in comparison with that of the structure without side braces; similarly, those of the maximum story drift angle and peak stress are defined, the same as the following tables.

3.2 Influence of the Cross Section of the front/Rear Braces

Assume that the cross section of side braces is $\phi 152\times 5$, and different cross sections of the front/rear braces such as $\phi 73\times 3$, $\phi 102\times 4$, $\phi 121\times 4$, $\phi 152\times 5$, $\phi 168\times 8$, as well as $\phi 203\times 9$ are considered, respectively. The horizontal concentrated loads of each 5kN are applied on the nodes in one side frame of the structure along the longitudinal direction, and the vertical concentrated loads of each 8kN are exerted on various column nodes. The other parameters are identical with those in *Section 2.2.1*. The results by static analysis are listed in Table 5.

The results show that the setting of the front/rear braces of the hoop stories can significantly improve the lateral stiffness along the longitudinal direction and reduce the values of various static indices. Also, when the cross section of the front/rear braces reaches a certain value, its further increase just brings about slight decrease of the structural maximum lateral displacement, storey drift angle, and the peak stress. Additionally, synthesizing the results in Tables 4 and 5 shows that, the structural transverse stiffness is comparatively less than the longitudinal one, and thus the structural deformation depends on the transverse lateral displacement.

Table. 5 Static Indices of the Structures with Different Cross Sections of Front/Rear Braces

Cross section of the front/rear braces	Maximum displacement /mm	Decline rate of maximum displacement	Maximum storey drift angle /$\times 10^{-3}$rad	Decline rate of maximum storey drift angle	Peak stress /MPa	Decline rate of peak stress
$\phi 73\times 3$	25.2	85.2%	1.57	82.3%	49.64	57.4%
$\phi 89\times 4$	19.6	88.5%	1.16	87.0%	44.81	61.6%
$\phi 102\times 4$	18.3	89.3%	1.06	88.1%	43.52	62.7%
$\phi 121\times 4$	16.8	90.1%	0.94	89.4%	41.98	64.0%
$\phi 152\times 5$	13.7	92.0%	0.70	92.1%	38.38	67.1%
$\phi 168\times 8$	10.9	93.5%	0.58	93.5%	34.7	70.2%
$\phi 203\times 9$	9.8	94.2%	0.53	94.1%	33.44	71.3%
Without front/rear braces	170.3	-	8.90	-	116.58	-

3.3 Influence of Storey Height

The storey height of parking structures usually varies from 1.7 to 2.2m. Here let the cross sections of the front/rear and side braces be $\phi 121\times 4$ and $\phi 152\times 5$, respectively. The other parameters and loads are identical with those in *Section 2.2.1*. The static analytical results of the structures with different storey heights are summarized in Table 6.

Obviously, the maximum lateral displacement, storey drift angle and peak stress increase with increase of the storey height. Meanwhile, the structural ratio of height to width also increases correspondingly, which has adverse influence on the structures. On the other hand, the increase of storey height means the decrease of both the linear stiffness of columns and structural lateral stiffness. Therefore, the storey height should be as small as possible to improve the structural bearing capacity and reduce the steel consumption.

Table 6. Static Indices of the Structures with Different Storey Heights

Storey height /m	1.7	1.8	1.9	2.0	2.1	2.2
Maximum lateral displacement /mm	14.9	16.63	18.52	20.58	22.81	25.21
Maximum storey drift angle /$\times 10^{-3}$rad	1.18	1.26	1.34	1.43	1.52	1.62
Peak stress /MPa	33.02	33.54	34.05	34.57	35.09	35.61

3.4 Influence of Linear Stiffness Ratio of Beam to Column

Assume that the cross sections of the front/rear braces, side braces and columns are $\phi 121\times 4$, $\phi 152\times 5$, and H-250×300×8×10, respectively. Consider different cross sections of beams, and thus the linear stiffness ratios of beam to column are 1/89, 1/40, 1/20, 1/12, 1/7, and 1/3, respectively. The other parameters and loads are identical with those in *Section 2.2.1*. Various static indices of the structures with different linear stiffness ratios of beam to column are listed in Table 7. It can be seen that, with increase of the linear stiffness ratio of beam to column, various static indices of the structure decline basically. The increase of linear stiffness ratio of beam to column is actually an improvement of constriction to columns, which effectively restricts the end rotation and displacement of columns. Additionally, the decline ratio of each static index decreases with increase of the linear stiffness ratio of beam to column. The decline rate of peak stress is even negative, that is to say, the peak stress does not decrease but increase. This indicates that excessive linear stiffness

ratios of beam to column can cause evident stress concentration at the hoop stories, and the negative effect exceeds the positive one. Consequently, the linear stiffness ratio of beam to column should not be too large. For the model in this section, the reasonable value is 1/40 to 1/20.

Table 7. Static Indices of the Structures with Different Linear Stiffness Ratios of Beam to Column

Cross section of beam /mm	Linear stiffness ratios of beam to column	Maximum lateral displacement /mm	Decline rate of maximum lateral displacement /%	Maximum storey drift angle /$\times 10^{-3}$rad	Decline rate of maximum storey drift angle /%	Peak stress /MPa	Decline rate of peak stress /%
H100×100×6×8	1/89	25.2 (161.4)	84.4	1.62 (7.22)	77.5	35.62 (65.32)	45.5
H125×125×6.5×9	1/40	21.7 (83.6)	74.0	1.40 (3.97)	64.8	34.2 (48.15)	28.9
H150×150×7×10	1/20	18.2 (48.7)	62.6	1.15 (2.35)	51.2	32.58 (39.52)	17.6
H175×175×7.5×11	1/12	15.0 (31.0)	51.6	0.91 (1.50)	39.4	30.81 (33.96)	9.3
H200×200×8×12	1/7	12.4 (21.4)	41.8	0.71 (1.00)	29.4	29.07 (30.24)	3.9
H250×250×9×14	1/3	8.9 (12.2)	27.0	0.42 (0.51)	15.6	26.18 (25.89)	-1.1

PS: The data in brackets are the results of the corresponding conventional structures with hoop stories.

4. PARAMETRIC ANALYSIS OF STABILITY

The influence of various parameters such as the braces in hoop stories, linear stiffness ratio of beam to column, and the initial geometric imperfection on structural nonlinear stability is studied in this section. Similarly, the 14-storey structure with optimal arrangement of hoop stories is taken to analyze. The length, width and storey height of the structure are 8, 6, and 2.2m, respectively. The cross section of columns is H-250×300×8×10. And the load pattern is identical with that as described in *Section 2.2.1*.

4.1 Influence of the Bracing Stiffness

Let the cross sections of beams and the front/rear braces be H-150×150×7×10 and $\phi 121\times 4$, respectively. And different cross sections of side braces in the hoop stories such as $\phi 73\times 3$, $\phi 89\times 4$, $\phi 102\times 4$, $\phi 121\times 4$, $\phi 152\times 5$, $\phi 168\times 8$, and $\phi 203\times 9$ are considered, respectively. Then let the cross section of the side braces be $\phi 152\times 5$, and different cross sections of the front/rear braces in the hoop stories such as $\phi 73\times 3$, $\phi 102\times 4$, $\phi 121\times 4$, $\phi 152\times 5$, $\phi 168\times 8$, and $\phi 203\times 9$ are considered, respectively. The relational curves of the structural ultimate load with the cross-sectional area of the side braces and that of the front/rear braces are displayed in Figures 10 and 11, respectively.

From the results as shown in Figure 10 it can be seen that, the ultimate load significantly increases with increase of the cross section of side braces at some extent, but it is not the larger the better. Combined with the results in Table 4, it can be drawn that the side braces of hoop stories have similar influence on static property and stability. There exists a rational upper limit for cross section of the side braces. For this structure, the optimal cross section of side braces is $\phi 152\times 5$.

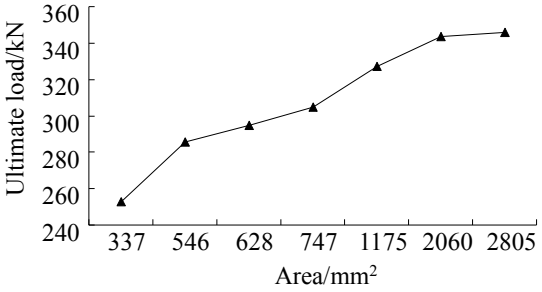

Figure 10. Relationship between Ultimate Load and Cross-sectional Area of the Side Braces of the Structure

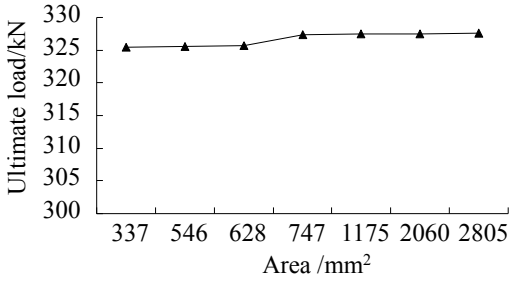

Figure 11. Relationship between Ultimate Load and Cross-sectional Area of the Front/Rear Braces of the Structure

As shown in Figure 11, the change of structural ultimate load with increase of cross section of the front/rear braces is not remarkable. Actually, from the first-order buckling mode as shown in Figure 8, it can be understood that the structural overall stability depends on the stability of columns along the transverse direction, but the front/rear braces can only improve the structural longitudinal stability. Therefore, the change of cross section of the front/rear braces has no effect on improvement of the structural overall stability and the cross section of these members can thus be determined according to the constructional requirements.

4.2 Influence of Linear Stiffness Ratio of Beam to Column

It is supposed that the cross sections of the front/rear braces and side braces are $\phi 121\times 4$ as well as $\phi 152\times 5$, respectively. Let the cross section of columns be H-250×300×8×10, and by changing the cross section of beams, different values of the linear stiffness ratio of beam to column such as 1/89, 1/40, 1/20, 1/12, 1/7, and 1/3 are considered, respectively. The other conditions are identical with those in Section 4.1. The relationship curves between ultimate load and linear stiffness ratio of beam to column of the structures are displayed in Figure 12.

It can be seen that, the ultimate loads of the two kinds of models increase remarkably with increase of the linear stiffness ratio of beam to column. In essence, the increase of linear stiffness of beams will strengthen the constraint of beams to the rotation of column ends, which will shorten the interval of inflection point of columns and improve the structural stability eventually. However, the increase rate of ultimate load of model K234 in comparison with the model K000 decreases with increase of the linear stiffness ratio of beam to column as shown in Figure 13, which indicates that the hoop stories can enhance the structural stability evidently when the linear stiffness ratio of beam to column is relatively small. Synthetically, considering the effect on structural static property and stability, there exists an optimal range for linear stiffness ratio of beam to column of the structure with optimal arrangement of hoop stories, namely 1/40 to 1/20.

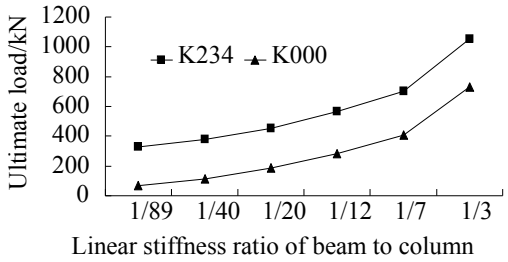

Figure 12. Relationship between Ultimate Load and Linear Stiffness Ratio of Beam to Column

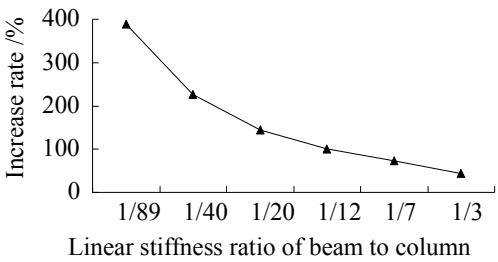

Figure 13. Relationship between Increase Rate of Ultimate Load and Linear Stiffness Ratio of Beam to Column

4.3 Influence of Initial Geometric Imperfection

The high-rise 3D parking structure with large ratio of height to width is typical tall and slender structure, which usually presents remarkable geometrical nonlinearity. It is also necessary to investigate the influence of initial geometric imperfections on structural stability. Let the cross section of the side braces be $\phi 152\times 5$, and the other parameters are the same as those in Section 4.1. Different imperfection amplitudes such as 10, 20, 30, 60, and 100mm (about 1/3000, 1/1500, 1/1000, 1/500, and 1/300 of the structural height) are considered, respectively. The load-displacement curves of the structures with different geometric imperfections are displayed in Figure 14, in which, the load is also the vertical concentrated load exerted on each column node, and the displacement is the lateral displacement of the top of the structure along the transverse direction.

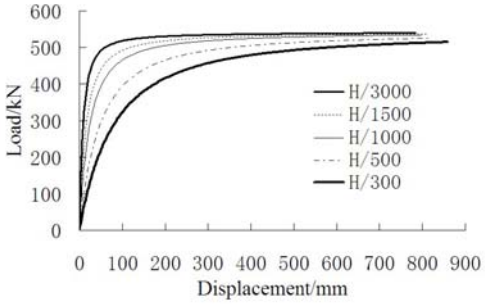

Figure 14. Load-displacement Curves of Structures with Different Geometric Imperfection Amplitudes

It can be seen that, the ultimate load decreases slightly with increase of the imperfection magnitude, but the effect is not notable. On the whole, the stability of this kind of structure is not sensitive to geometric imperfection.

5. CONCLUSIONS

The paper first presents a new structural arrangement style of high-rise tubular 3D parking structure, which is to set hoop stories at its proper height. Then the optimal intervals of hoop stories based on the equal stability and equal drift principle are determined. Additionally, comprehensive static property and stability of the structures with different arrangement schemes of hoop stories are compared. Finally, parameters analyses and discusses about the influence of various parameter on static properties and stability are carried out. The main conclusions can be drawn as follows.

1) The lateral stiffness of the structure with hoop stories arranged based on the equal stability and equal drift principle is obviously improved and the lateral displacement is thus controlled effectively. Moreover, the fluctuation amplitude of storey drift along the structural height is small, which benefits the stable operation of hoisting machines.

2) The axial force of columns at the bottom of the optimal structure increases for the introduction of hoop stories and the structural overturning resistance is also improved. Meanwhile, the concentration of bending moment of the columns at the lower several stories of the structure is avoided. Furthermore, the sudden change of shear force becomes not remarkable for the rational arrangement of hoop stories in the structure.

3) The long columns are divided into several equivalent short columns due to the restraint of hoop stories to columns. The structural overall stability depends on the equivalent short columns and the stability bearing capacity is thus improved evidently. Comparison analysis shows that the ultimate load of structure with optimal arrangement of hoop stories is larger than those of the others.

4) The good structural performance verifies the rationality of arrangement of hoop stories according to the equal stability and equal drift principle, which can provide a new design idea for this kind of structure.

5) The stability and static property can be effectively improved with increase of cross section of the side braces in the hoop stories, but it is not the larger the better. Whereas, the change in cross section of the front/rear braces almost has no influence on those indices and thus the cross section of these braces can be determined according to the constructional requirements.

6) The structural lateral stiffness and overall stability can be improved with increase of the linear stiffness ratio of beam to column. However, the excessive increase will result in stress concentration of members in the hoop stories, and the effect of hoop stories becomes not notable. Therefore, the linear stiffness ratio of beam to column should not be too large.

7) On the whole, the stability of the structure with optimal arrangement of hoop stories is not very sensitive to geometric imperfection.

ACKNOWLEDGMENT

This work was financially supported by the National Natural Science Foundation of China (Grant no. 51178176), Natural Science Foundation of Hunan Province (Grant no. 13JJ6022), Doctoral Fund of Ministry of Education of China (Grant no. 20120161110019), Science and Technology Innovative Research Team Project of Universities in Hunan Province, and the Fundamental Research Funds for the Central Universities of Hunan University, which are gratefully acknowledged.

REFERENCES

[1] Amott, R., “Spatial Competition between Parking Garages and Downtown Parking Policy”, Transport Policy, 2009, Vol. 13, No. 1, pp. 458-469.

[2] Amélie, Y.D. and Bryan, C.P., “The Environmental and Economic Costs of Sprawling Parking Lots in the United States”, Land Use Policy, 2010, Vol. 27, No. 2, pp. 255-261.

[3] Eduardo, B., Luis, C. and João, P. F., “Parking at the UC Campus : Problems and Solutions”, Cities, 2011, Vol. 28, No. 5, pp. 406-413.

[4] Yu, W.K. and Chung, K.F., “Axial Buckling of Bamboo Columns in Bamboo Scaffolds”, Engineering Structures, 2005, Vol. 27, No. 1, pp. 61-73.

[5] Tommy, Y. L. and Cui, H.Z., “Strength Analysis of Bamboo by Microscopic Investigation of Bamboo Fibre”, Construction and Building Materials, 2008, Vol. 22, No. 7, pp. 1532-1535.

[6] Khosrow, G., “Bamboo as Reinforcement in Structural Concrete Elements”, Cement and Concrete Composites, 2005, Vol. 27, No. 6, pp. 637-649.

[7] Ma, J.F., Chen, W.Y. and Zhao, L., “Elastic Buckling of Bionic Cylindrical Shells Based on Bamboo” Journal of Bionic Engineering, 2008, Vol. 7, No. 2, pp. 231-238.

[8] Karthikeyan, C., Krishnan, R. and Princy, S.A., "Bionics and Structural Biology: a Novel Approach for Bio-energy Production", Journal of Bionic Engineering, 2008, Vol. 5, No. 1, pp. 25-32.
[9] Zhao, L., Ma, J.F. and Wang, T., "Lightweight Design of Mechanical Structures Based on Structural Bionic Methodology", Journal of Bionic Engineering, 2010, Vol. 7, No. Suppl., pp. 224-231.
[10] He, Y.J. and Zhou X.H., "Approximate Analytical Method of Multi-storey or High-rise Steel Three-dimensional Parking Structures", International Journal of Advanced Steel Construction, 2012, Vol. 8, No. 2, pp. 112-123.
[11] Li, G.Q., "Design of High-rise Steel Structure", 2004, Beijing, China Building Industry Press (In Chinese).
[12] Hyo, G.K. and Jong, Y.S., "Live Load Factors for Parking Garage Members", Structural Safety, 2000, Vol. 22, No. 3, pp. 251-279.
[13] Salemi, F., Salone, V. and Wang, W.D., "Stability of a Competition Model with Two-stage Structure", Applied Mathematics and Computation, 1999, Vol. 99, No. 2, pp. 221-231.
[14] Zhao, Y.C., Xian, C. and Dong, S.L., "Strength and Stability Analysis of Circular Steel Arches in a Long-span Ellipsoidal Shell Structure", China Civil Engineering Journal, 2005, Vol. 38, No. 5, pp. 15-23 (In Chinese).
[15] Widjaja, BR., "Path-following Technique Based on Residual Energy Suppression for Nonlinear Finite Element Analysis", Computer & Structures, 1998, Vol. 66, No. 2, pp. 201-9.

NUMERICAL SIMULATION OF INELASTIC CYCLIC RESPONSE OF HSS BRACES UPON FRACTURE

Lucia Tirca[1,*] and Liang Chen[2]

[1] *Department of Building, Civil and Environmental Engineering, Concordia University, Montreal, Canada*
2 Department of Civil, Geological, and Mining Engineering, Ecole Polytechnique, Montreal, Canada
**(Corresponding author: E-mail: Lucia.Tirca@concordia.ca)*

Received: 21 April 2013; Revised: 27 August 2013; Accepted: 13 September 2013

ABSTRACT: Concentrically braced frames (CBFs) with a tension-compression bracing system dissipate hysteretic energy when braces yield in tension and buckle in compression, whereas the hysteretic response of hallow structural section (HSS) braces varies with brace slenderness, width-to-thickness ratio, and yield strength. Modelling the nonlinear response of braces upon the fracture requires an assigned brace fracture model and implicitly calibrated input material parameters. The selected brace fracture models are those that are compatible to nonlinear analysis and fiber-based elements formulation suited to OpenSees framework. To replicate the brace response, nonlinear beam-column elements that encompass distributed plasticity and discretized fiber cross-sections were used, whereas to simulate brace fracture, the strain fatigue model was considered. In this study, in order to predict the failure strain for a single reversal value that is required as input parameter in the strain fatigue model, regression analysis was employed and the proposed equation was given for square HSS braces and validated against experimental test results for a wide range of brace slenderness ratios, $50 \leq kL/r \leq 150$ and types of displacement loading history. The predicted failure strain value is expressed in terms of slenderness ratio, width-to-thickness ratio and yield strength of steel. Comparisons to existing brace fracture models, such as the strain-range and end-rotation of braces at fracture, are provided. All aforementioned brace fracture models were evaluated against experimental tests results, while replicating fourteen specimens that were found in the literature.

Keywords: HSS braces, brace fracture models, inelastic response, strain, buckling, yielding, fracture, fatigue material

1. INTRODUCTION

Concentrically braced frames (CBFs) with a tension-compression bracing system dissipate hysteretic energy when braces yield in tension and buckle in compression, whereas the hysteretic response of hallow structural section (HSS) braces varies with brace slenderness, width-to-thickness ratio, and yield strength. Accordingly, slender braces dissipate less hysteresis energy in compression than do stocky braces, although the latter are prone to low-cycle fatigue failure. To prevent the occurrence of local buckling and to maintain the plastic moment capacity through sufficient rotation, the CSA/S16-2009 standard [1] requires braces to comply to Class 1 sections. In addition, the slenderness ratio of HSS bracing members, *kL/r,* shall not exceed 200 and not be less than 70 when the CBF building is located in seismic area, whereas the short period spectral acceleration ratio is greater than 0.75 (e.g. Vancouver, BC, Canada). Although the seismic response of braces dominates the behaviour of CBFs, the out-of-plane rotation capacity of gusset plate connections that provide boundary conditions to steel HSS braces impacts on their strain life [2]. To preserve the integrity of the gravity-load carrying capacity system during large earthquakes, researchers have agreed that the tensile fracture of HSS braces is the desired failure mode of a ductile CBF system [3].

Prior experimental research has been conducted on the behaviour of HSS braces in order to assess their post-buckling capacity, axial deformation and fracture life [4-10]. To emphasize the effect of

the slenderness ratio and the width-to-thickness ratio, Tremblay [11] compiled a dataset of 76 specimens and reported a strong influence of the slenderness ratio and less effect of the with-to-thickness ratio and type of history loading on the fracture life of HSS braces. Han *et al.* [10] concluded that specimens that have a small width-to-thickness ratio cannot withstand several inelastic cycles due to early fracture at the slotted end of bracing members. Lee and Bruneau [12] investigated the behaviour of 66 brace specimens and reported a significant drop in the compressive strength, as well as a drop in the amount of hysteresis energy dissipated in compression by braces that have a slenderness ratio greater than 80.

The concept of performance based seismic design of structures is widely accepted. However, modelling the nonlinear response of braces upon fracture and collapse of the CBF system is not straightforward, as the input parameters that define the brace fracture model should be calibrated against experimental test results. In this study, the selected brace fracture models are those that are compatible to nonlinear analysis and fiber-based elements. Although local buckling is not considered in the brace model, the hysteresis response does not seem to be affected during the inelastic cyclic excursions prior to failure [13]. Previous brace fracture models have linked the initiation of fracture to the global response of HSS braces. These models, which were proposed by Uriz [14], Hsiao et al. [3] and Tremblay et al. [15], are presented and evaluated in this study using the OpenSees software (Open System for Earthquake Engineering Simulation) [16].

The brace fracture model that was developed by Uriz [14] is based on low-cycle fatigue, whereas the cumulative damage was assessed by employing a simplified rainflow cyclic counting technique. To reduce the volume of computations, this modified procedure was set in the formulation of fatigue material that is embedded in OpenSees. The consistency of fatigue material parameters values m and ε_o that were proposed by Uriz was verified by Santagati et al. [17] for 32 HSS specimens that were found in the literature and by Salawdeh and Goggins [18] for 28 HSS specimens. In both studies, square and rectangular HSS specimens were considered with an approximate distribution of 70% square and 30% rectangular cross-sections. In comparing the ε_0 values that ensued from the above studies, it was found that Salawdeh and Goggins recommended a value more than twice as great as that proposed by Santagati et al. Thus, to solve this drawback, Lignos and Karamanci [19] proposed an empirical regression equation that is able to predict the ε_0 value at the onset of HSS brace fracture by considering the following variables: slenderness ratio, width-to-thickness ratio and yield strength. The equation was validated for HSS braces whose slenderness ratio is between *27* and *85*. However, for modelling the nonlinear response of HSS braces with slenderness ratio larger than *85* an empirical expression for the predicted ε_0 value is required.

Hsiao et al. [3] recently compiled the responses of 44 square HSS brace specimens with a slenderness ratio between 35.8 and 166 and proposed a strain-range fracture model that is based on the maximum compressive strain-range that is developed in the extreme fiber of the cross-section of brace at the plastic hinge location. In addition, an empirical regression equation expressed as a function of slenderness ratio, width-to-thickness ratio and yield strength was provided to predict the maximum compressive strain-range developed when fracture of brace occurred.

To estimate the onset of HSS brace fracture, Tremblay et al. [15] investigated 7 specimens in single brace configuration and 10 specimens in X-bracing configuration. An empirical equation that quantifies the end-rotation of brace at fracture was proposed for rectangular HSS members as a function of slenderness ratio and width-to-thickness ratio. Latter, Tremblay [20] conducted a study on the effect of brace slenderness ratio versus the development of compressive strain and concluded that stocky braces experience larger compressive strain than slender braces.

Thus, the purpose of this study is two-fold: i) to propose an empirical regression equation for square HSS braces whose slenderness ratio is between 50 and 150 that is able to quantify the predicted failure strain for a single reversal value at the onset of brace fracture, $\varepsilon_{0,pred}$, and ii) to compare the responses of HSS braces when fracture models, such as the strain-range and end-rotation of braces at fracture, are considered versus the strain fatigue model that employs as input the computed $\varepsilon_{0,pred}$ value. Then, the strain-range, the end-rotation of braces at fracture and the proposed strain fatigue model are evaluated against experimental test results.

2. EXISTING BRACE FRACTURE MODELS

Existing approaches that are used to define the fracture model of brace members subjected to cyclic loading are based either on the strain fatigue model and strain-range model or on the end-rotation of braces at fracture model. In all cases, it has been assumed that the crack is initiated at the brace mid-length after the plastic hinge is formed. These brace fracture models are compatible with the OpenSees environment, where braces are modelled as beam-column elements with distributed plasticity and fiber-based formulation [21].

The first brace fracture model embedded in the OpenSees framework was developed by Uriz [14] and was based on low-cycle fatigue of constant plastic strain amplitude, which used an accumulative strain to predict damage in agreement with the Miner's rule [22]. To quantify the accumulation of plastic damage, a damage index, *DI,* was estimated by computing the sum of all contributing cycles *i* starting from $j = 1$ until failure was reached ($j = n$):

$$DI = \sum_{j=1}^{n} \left(\frac{n(\varepsilon_i)}{N_f(\varepsilon_i)} \right)_j \quad (1)$$

In Eq. 1, $n(\varepsilon_i)$ is the current number of cycles at strain amplitude ε_i and $N_f(\varepsilon_i)$ is the number of life cycles that a given brace member may sustain before failure. As shown in Eq. 1, the damage index is the ratio of the current plastic strain and total plastic deformability [23]. However, under seismic loading, the strain may not have constant amplitude [13]. Manson [24] and Coffin [25] conducted independent research on the matter of fatigue and concluded that the relationship between plastic strain amplitude, ε_i, that is experienced by each cycle *i,* and the number of fatigue cycles to failure, N_f, is linear on the log-log domain, while the slope is equal to *m* (Eq. 2).

$$\varepsilon_i = \varepsilon_o (N_f)^m \quad (2)$$

In Eq. 2, *m* and ε_o are known as the fatigue ductility exponent and fatigue ductility coefficient, respectively. The damage index, *DI,* varies from zero for an undamaged material to *1.0* at failure [14]. To consider the accumulation of damage and to reduce the volume of computations, the modified rainflow cyclic counting method that records only the four most recent peaks of strain reversals at any given time was implemented in the formulation of fatigue material embedded in OpenSees [13, 14]. Thus, when a fiber of the element cross-section reached its fatigue life ($ID \geq 1$), its stress and stiffness fell to zero. Since the model does not account for local buckling, the strain in the model does not reflect the strain developed in the member [26]. By considering this accumulated strain approach and the experimental tests performed by Yang [8], Uriz proposed the following set of fatigue material parameters value for HSS brace members: $\varepsilon_o = 0.095$ and $m = -0.5$. When different experimental tests were used by researchers to validate the consistency of material parameters value [17,18] the following sets were recommended: $\varepsilon_o = 0.07;\ m = -0.45$ [17] and $\varepsilon_o = 0.19;\ m = -0.5$ [18]. As from above, the largest recommended ε_o value (*0.19*) is more than twice than the smaller value (0.07). Also, in some cases, it was reported differences between the number

of life cycles experienced by the model and that exhibited by the physical brace.
To solve this drawback, Lignos and Karamanci [19] proposed the following regression equation to predict the material parameter value, $\varepsilon_{o,pred}$:

$$\varepsilon_{0pred.} = 0.291\left(\frac{kL}{r}\right)^{-0.484}\left(\frac{w}{t}\right)^{-0.613}\left(\frac{E}{F_y}\right)^{0.3} \quad (3)$$

where, *kL/r* is the slenderness ratio, *w/t* is the width-to-thickness ratio, and F_y and E are the yield strength of braces and Young's modulus, respectively. The value of fatigue ductility exponent, $m = -0.3$, is treated as constant. By using $m = -0.3$ and $\varepsilon_{o,pred}$ as resulted from Eq. 3, a good match between predicted and calibrated ε_o value was reported, while ε_o varied between 0.05 and 0.10 with a mean of approximately 0.064. Eq. 3 was validated for HSS braces that had a slenderness ratio between 27 and 85.

To capture the crack initiation, Hsiao et al. [3] proposed the strain-range brace fracture model. In this model, the main parameter is the maximum strain-range that is developed in the extreme compressive fiber of the HSS brace cross-section at the location of plastic hinge formation. However, the true strain deformation at the onset of cupping due to local buckling cannot be captured when fiber-based elements are considered. Based on a regression analysis comprising the responses of 44 square HSS brace specimens expressed in terms of simulated strain-range through the entire loading history, the following equation was proposed to predict the maximum strain-range:

$$max.\boldsymbol{\varepsilon}_{range\ ,pred.} = 0.1435\left(\frac{kL}{r}\right)^{-0.3}\left(\frac{w}{t}\right)^{-0.4}\left(\frac{E}{F_y}\right)^{0.2} \quad (4)$$

where, *kL/r*; *w/t* and E/F_y are the same parameters as in Eq. 3. Among the 44 square HSS specimens that were considered in the study that was reported by Hsiao et al. [3], 43 had a slenderness ratio that was less than 82.7 and the simulated maximum strain-range value, $max.\varepsilon_{rg,sim}$ value varied between 0.025 and 0.069. It may be noted that the literature contains relatively few experimental studies conducted on square HSS braces with *kL/r* larger than 85.

To predict the onset of fracture of rectangular HSS braces, Tremblay et al. [15] considered the brace end-rotation parameter, which is defined as a function of displacement ductility of braces and brace length. As a result of compiling 17 experimental tests conducted on pin-ended square and rectangular HSS brace members with *kL/r* varying between 60 and 140, the following equation that measures the maximum end-rotation corresponding to brace fracture is proposed:

$$\theta_{f,pred.} = 0.091\left(\frac{kL}{r}\right)^{0.3}\left(\frac{bo}{t}\ \frac{do}{t}\right)^{-0.1} \quad (5)$$

where b_o and d_o are the brace dimensions computed to verify the Class of sections for HSS braces ($b_o=b-4t$ and $d_o=d-4t$). Thus, the maximum end-rotation of a brace at fracture depends mainly on the slenderness ratio and width-to-thickness ratio.

3. EXPERIMENTAL DATA SELECTION

To validate the numerical simulation of HSS brace fracture models that were developed in the

OpenSees framework and the consistency of proposed material parameters values, the following criteria were considered for the selection of existing experimental test results: i) tests conducted on full-scale square HSS brace members that were subjected to quasi-static cycling loading applied first in compression; ii) specimens that exhibited brace fracture; iii) at least one selected specimen was subjected to different types of displacement loading history; iv) at least one selected brace was subjected to the same displacement loading history applied first in compression and first in tension; v) the selected experimental tests provide sufficient information about geometry, material properties and loading history. Thus, 14 full-scale HSS brace specimens with slenderness ratios between *52.4* and *143.5* were selected from three different studies reported by Archambault [5], Shaback [6] and Lee and Goel [4]. Twelve of the selected specimens [5,6] were made of steel G40.21-350W and two from study [4] were made of steel A500 grade B. All of them reached fracture failure while buckling out-of-plane. To emphasize on the effect of displacement loading history on brace response, two identical specimens (S1B and S1QB) were selected from study [5] despite their rectangular HSS cross-section. Data including the test ID, the area of brace cross-section, A_g, the yield strength of steel, F_y, the Young's modulus of elasticity, E, the clear length of brace measured between the gusset plates, L_b, the length between the expected hinges in gusset plates, L_H, the slenderness parameter, λ, and the yield axial deformation, δ_y are given in Table 1 and the geometrical scheme of the test setup is shown in Figure 1. The slenderness parameter: $\lambda = (KL/r)(F_y/\pi^2E)^{0,5}$ where r is the radius of gyration, is computed in agreement with the CSA/S16 standard [1] requirements. The tensile, T_r, and compressive resistance, C_r, computed with $\phi = 1.0$ are: $T_r = A_gF_y$ and $C_r = A_gF_y(1+\lambda^{2n})^{-1/n}$, where $n=1.34$. In accordance with the CSA/S16 standard, the probable postbuckling strength of braces, C_u', is computed as: $C_u' = 0.2A_gR_yF$ with $R_y = 1.1$. The probable tensile T_u and compressive resistance C_u are computed by multiplying T_r and C_r (calculated with $\phi = 1.0$) by R_y. For CBFs that are located in moderate-to-high seismic zones, the b_0/t limit prescribed in the CSA/S16 standard is given as a function of brace slenderness ratio, KL/r, while $b_0 = b-4t$. Thus, to be classified as Class 1 sections, the HSS braces

Table 1. Properties of Selected Brace Specimens

St.	Test no.	HSS size	A_g	L_b	L_H	F_y	E	λ	T_r	C_r	C_u'	C_r/T_r	δ_y
			mm^2	mm	mm	MPa	GPa		kN	kN	kN		mm
1	S1B[a)]	76x127x4.8	1790	4007	4610	353	189	1.319	632	272	139	0.430	7.92
	S1QB [a)]	76x127x4.8	1790	4009	4610	353	189	1.319	632	272	139	0.430	7.92
	S3B	76x 76x4.8	1310	4179	4610	332	187	1.991	435	98	96	0.225	8.13
	S3A	76x 76x4.8	1310	4179	4610	332	187	1.991	435	98	96	0.225	8.13
2	1B	127x127x8.0	3620	3350	3450	421	191	0.788	1524	1111	335	0.729	7.05
	2A	152x152x8.0	4430	3950	4040	442	202	0.794	1958	1419	431	0.724	8.30
	2B	152x152x9.5	5210	3950	4028	442	196	0.792	2303	1672	506	0.726	8.60
	3A [a)]	127x127x6.4	2960	4350	4446	421	191	0.968	1246	690	274	0.554	10.0
	3B	127x127x8.0	3620	4350	4446	421	191	0.983	1524	924	335	0.606	9.16
	3C	127x127x9.5	4240	4350	4446	421	191	0.921	1785	1036	393	0.580	10.0
	4A	152x152x8.0	4430	4850	4946	461	191	0.993	2042	1103	449	0.540	10.7
	4B	152x152x9.5	5210	4850	4946	461	191	0.934	2402	1376	528	0.573	10.7
3	Lee-1 [a)]	5x5x0.188	2271	2946	3429	426	200	0.864	967	658	213	0.681	6.27
	Lee-5	4x4x0.250	2316	3099	3454	510	200	1.230	1181	556	260	0.471	7.90

Study 1: Archambault et al. [5]; Study 2: Shaback [6]; Study 3: Lee and Goel [4].
a) Width-to-thickness ratio does not satisfy the current CSA/S16 requirements.

with $KL/r \leq 100$ must show a maximum b_0/t limit that is less than $330/F_y^{0.5}$ and braces with KL/r = 200 must show the b_0/t limit as $420/F_y^{0.5}$. For HSS braces with $100< KL/r < 200$, the width-to-thickness ratio is computed by a linear interpolation between $330/F_y^{0.5}$ and $420/F_y^{0.5}$. For the HSS braces given in Table 1, the b_0/t ratio varies between 9.4 for 3C and 15 for 4A. The normalized b_0/t ratio with respect to b_0/t limit varies between 0.45 (S3B, S3A) and 0.98 for 4A, whereas for specimens such as, S1B, S1QB, 3A and Lee-1, the b_0/t ratio does not satisfy the current standard requirements.

The four selected specimens from *Study 1* [5] and two from *Study 3* [4] were tested in a single bracing frame configuration as pin-ended members (Figure 1a), whereas the eight selected specimens from *Study 2* [6] were tested as independent pin-ended members (Figure 1b). The effective slenderness ratio of braces was evaluated in the buckling plan, while taking into account the applicable end conditions. The S1B and S3B specimens that were selected from *Study 1*, were tested under a cyclic quasi-static displacement protocol H_1, that is illustrated in Figures 2a and 2b,

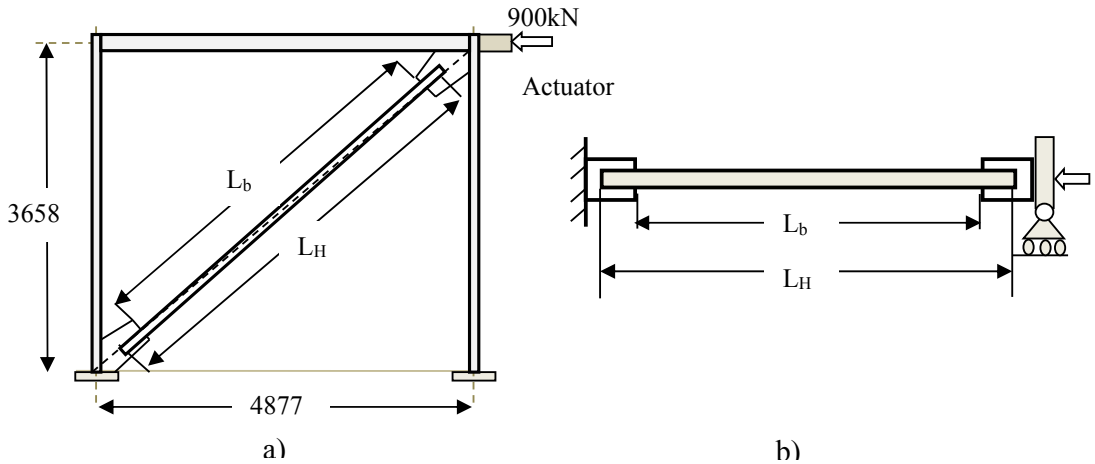

Figure 1. Geometrical Schemes of Brace Specimens:
a) Test Setup as per Study 1; b) Test Setup as per Study 2.

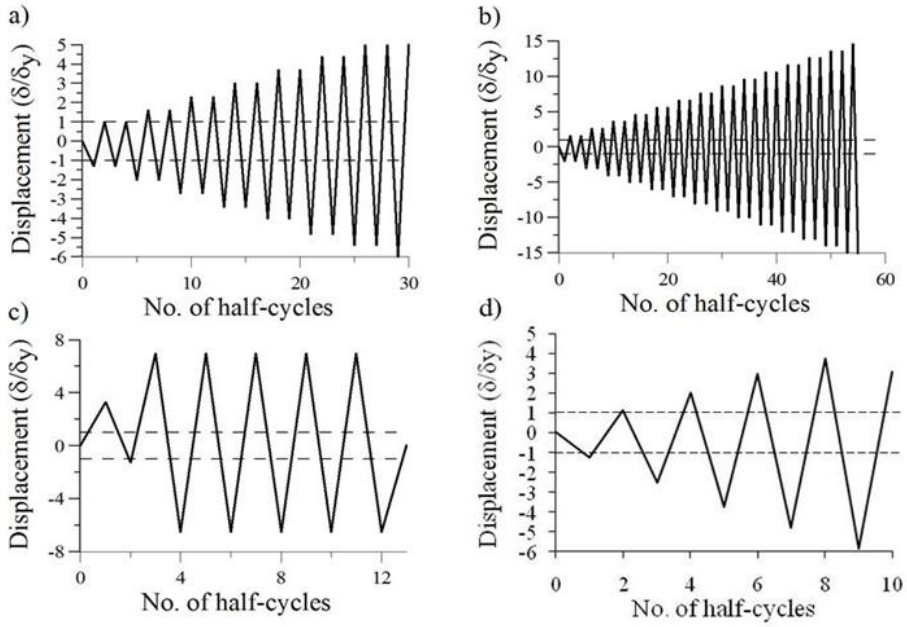

Figure 2. Types of Loading Histories: a) H_1 - S1B; b) H_1 - S3B; c) Q – S1QB; d) H_2 - 2A.

respectively. The S3A specimen was subjected to a loading similar to that of the S3B, but was first loaded in tension [11], whereas the S1QB was tested under the displacement history *Q,* shown in Figures 2c. The cyclic quasi-static displacement loading sequence H_1 shows a symmetrical displacement pattern with stepwise increasing deformation cycles, while the *Q* sequence was developed on the basis of results recorded from nonlinear dynamic time-history analyses conducted on typical two and three storey buildings that were subjected to several ground motions. All brace specimens belonging to *Study 2* are stocky members and were first loaded in compression under the asymmetric cyclic quasi-static displacement protocol, H_2, which is shown in Figure 2d [6,11]. Both selected specimens from *Study 3* were subjected to asymmetric loading history applied in compression. Thus, the Lee-1 brace was subjected to loading type 1, which is defined in [4], whereas the Lee-5 specimen was subjected to loading type 2 that was developed on the basis of the displacement history of a 2nd storey brace within a 6-storey CBF building that had been subjected to a large earthquake.

4. THE EFFECT OF MODELLING PARAMETERS ON THE BRACE RESPONSE

4.1 Fiber-Based Brace Model

The fiber-based brace model that was formulated in OpenSees consists of nonlinear beam-column elements with distributed plasticity along the element's length. Its nonlinear behaviour is embedded in the assigned Giuffre-Menegotto-Pinto steel material with isotropic strain hardening that is based on the Menegotto-Pinto function, which was defined to express stresses as a function of strain.

$$\sigma^* = b\varepsilon^* + \frac{(1-b)\varepsilon^*}{(1+\varepsilon^{*R})^{\frac{1}{R}}} \tag{6}$$

In Eq. 6, σ^* and ε^* are the effective stress and strain depending on the unload/reload interval, b is the ratio of the final to initial tangent stiffness and R is a material parameter that defines the shape of the unload curve. In the elastic range, the stress-strain relation is linear and the initial tangent stiffness E_t is equal to the elastic stiffness E. Along the yielding plateau, the strain increases from yielding strain ε_y to strain hardening ε_{sh}, whereas the stress σ_y is constant. The Giuffre-Menegotto-Pinto model is able to account for the accumulated plastic deformation at each point of load reversal. This implies that each hysteresis loop follows the previous loading path for a new reloading curve, while deformations are accumulated. In this study, all parameters that define the transition from the elastic to the plastic response of Giuffre-Menegotto-Pinto steel material are identical to those considered by Aguero et al. [26].

To simulate the brace inelastic response in OpenSees, the brace member is divided into *n*-number of nonlinear beam-column elements with fiber formulation and distributed plasticity as illustrated in Figure 3a. The model uses the corotational geometric transformation approach and the consideration of a sinusoidal pattern deformation at the onset of buckling, as well as the Gauss-Lobatto integration rule for distributed plasticity. For an accurate representation of curvature distribution along the element, at least three integration points are required, although four to six are recommended [27]. After the occurrence of buckling, the brace experiences large cycles of out-of-plane deformation and one may anticipate hinging of gusset plates [28]. To simulate the behaviour of gusset plate connection, two rotational springs and one torsional spring are defined in the zero-length element that connects each end of the brace to a rigid link. To replicate the out-of-plane flexural stiffness of the gusset plate, K_{gusset}, Hsiao et al. [21] recommended the following equation:

$$K_{gusset} = (E/L_{ave})(W_w t_g^3/12) \quad (7)$$

where E is Young's modulus of steel, W_w is the Whitmore width defined by a 30° projection angle, L_{ave} is the average of L_1, L_2, L_3 as shown in Figure 3b, and t_g is the thickness of the gusset plate. A second rotational spring that is added in the same zero-length element simulates the in-plane flexural stiffness of the gusset plate, which needs to be greater than the brace stiffness. When the out-of–plane buckling is anticipated, a third spring simulating the torsional restraint of gusset is added. It is defined as GJ/L_{ave}, where G is the shear modulus of steel material and J is the torsional constant of the Whitmore cross-section. Both flexural springs are made of Giuffre-Menegotto-Pinto steel material, whereas the torsional spring is made of elastic uniaxial material.

The accuracy of modelling braces with ends gusset plates depends on the following parameters: number of elements across the brace length, n_e; the number of integration points per element, n_i; initial out-of-straightness, e; fiber discretization technique and the number of fibers within cross-section, n_f; the gusset plate behaviour formulation and the definition of the brace fracture model.

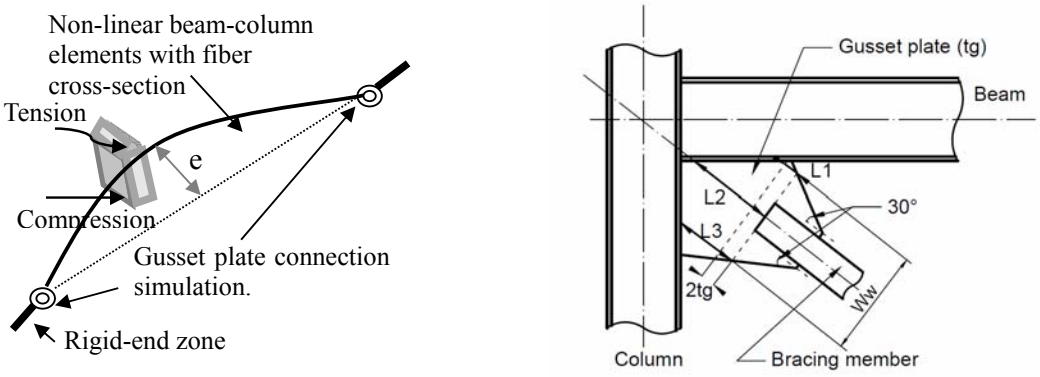

Figure 3. Model of Brace with End-Connections:
a) OpenSees Model; b) Geometry of Gusset Plate.

4.2 The Effect of Out-of-Straightness on the Brace Response

To capture the deflected shape of buckling braces, an initial out-of-straightness is assigned in the plan of buckling. Here, the S1B specimen was selected for investigations and the following out-of-straightness values were considered: $0.1\%L_b$; $0.2\%L_b$; $0.25\%L_b$; $0.33\%L_b$ and $1.0\%L_b$, where L_b is the brace length. To replicate the brace response, eight nonlinear beam-column elements with distributed plasticity [27] and a fiber-based formulation consisting of 64 fibers within the cross-section and discretization technique type *A* (Figure 4), as well as four integration points per element were considered. As shown in Figure 5, the initial out-of-straightness value influences the magnitude of the replicated buckling force. Thus, for a small assigned value, the buckling strength increases significantly, whereas the post-buckling strength remains unchanged [13]. Conversely, when the initial out-of-straightness is larger than expected (e.g. *L/100*), buckling occurred prematurely and may simulate a false inelastic deformation mechanism. When the initial out-of-straightness, e, varies between $0.2\%L_b$ ($L_b/500$) and $0.33\%L_b$ ($L_b/300$) a small difference in the simulated buckling force is reported. In this example, no brace fracture model was assigned.

The initial out-of-straightness may be estimated by using the equation proposed by Dicleli and Metha [30]:

$$e = \frac{M_{pb}}{P_b}\left(1 - \frac{P_b L^2}{12EI}\right) \tag{8}$$

where, M_{pb} is the reduced plastic moment of the brace that corresponds to the P_b compression force and both M_{pb} and P_b parameters are mapped on the surface bordered by the defined P-M interaction curve. The remaining parameters *L, E* and *I* are the length of the brace, the modulus of elasticity and the moment of inertia of the brace about its axis of buckling. For example, in the case of specimen 2A, the computed out-of-straightness value, $e = 8.9mm$, is equivalent to $L_b/500$. This ratio is in agreement with that proposed by Ziemian [31] for HSS braces.

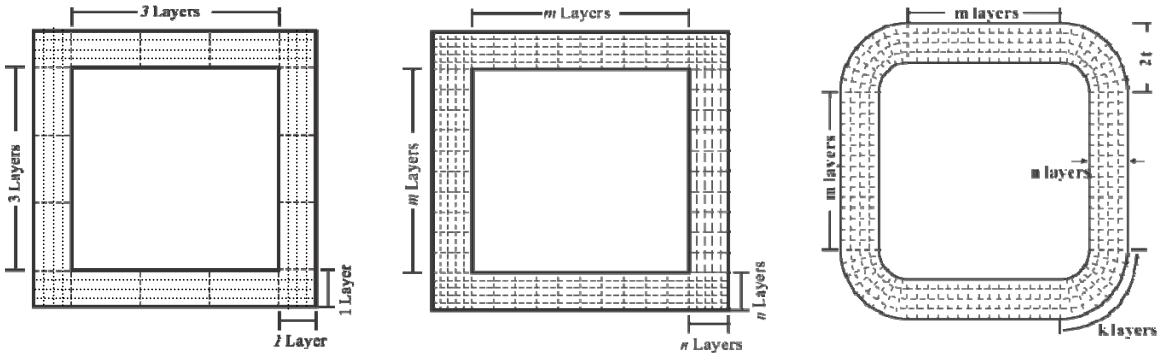

a) b) c)

Figure 4. Fiber Discretization Techniques Developed for the HSS Brace Cross-Section: a) Type *A, 4n(1+m)* fibers; b) Type *B, 4n(n+m)* fibers; c) Type *C, 4n(k+m)* fibers.

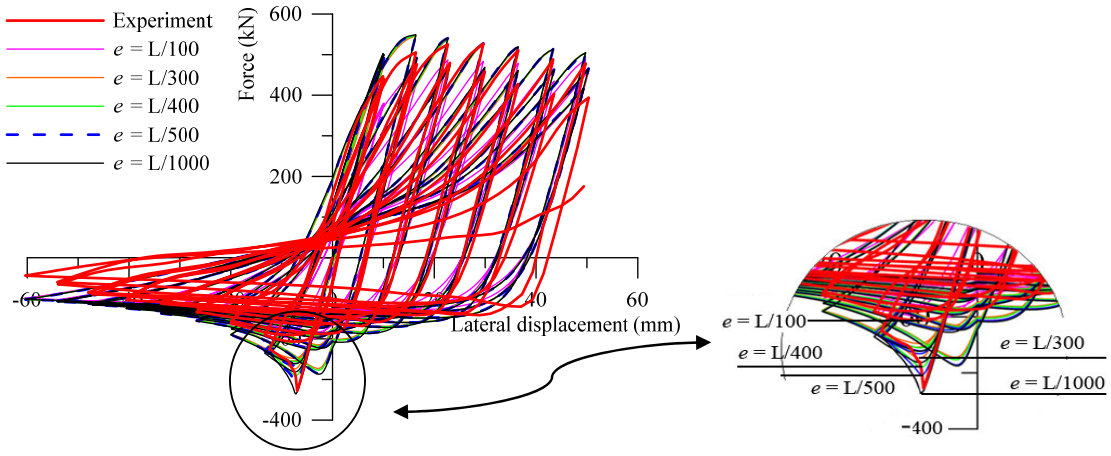

Figure 5. The Effect of Out-of-Straightness on the Buckling Strength of S1B Specimen.

4.3 The Effect of Number of Fibers within Brace Cross-Section and Discretization Technique

The number of fibers within a brace cross-section along with the applied discretization technique has an impact on the hysteretic response of HSS braces. Three types of existing fiber discretization techniques that are reported in the literature are labelled herein as types *A, B,* and *C* and are illustrated in Figure 4. Thus, type *A* consists of *4n(1+m)* fibers displayed as follows: *(n x 1.0)* fibers

are concentrated at each HSS corner and *4(n x m)* fibers are distributed at equal distances across the webs and flanges of the HSS cross-section. The type *B* discretization technique consists of *4n(n + m)* fibers with (*n x n*) fibers concentrated at each cross-sectional corner, and *4*(n *x m*) fibers distributed as per type *A*. Although type *C* fiber discretization displays the same number of fibers as type *B,* it differs by replacing the distributed line fibers that are located at HSS corners with rounded fibers that are assigned in parallel to the cross-sectional radius [20]. The effect of the number of fibers and the type of discretization technique on the inelastic brace response is illustrated for the S1B specimen in Figure 6a. In this example, the brace model consists of eight non-linear beam-column elements with four integration points per element and an out-of-straightness of $L_b/500$ that was assigned out-of-plane. The number of fibers within the HSS cross-section was set at 64 for discretization technique type *A* and at 500 (m = 20 fibers and n = 5 fibers) for types *B* and *C*. Although the cross-sectional area is unchanged, a difference in the behaviour of the brace under tensile force was observed when discretization technique type *C* was employed. As illustrated in Figure 6a, when using meshing technique type *B*, the tensile force is overestimated and the compressive force is slightly larger than that obtained from the experimental test. Thus, to match the test results, while avoiding converging problems and disturbance in the force-displacement hysteresis loops, fiber discretization technique type *C* is recommended.

To summarize, the number of fibers used to mesh the HSS brace cross-section influences its hysteresis response, whereas, in the case of highly nonlinear behaviour, using a finer meshing discretization improves the chance of convergence although increasing the computation time. Thus, mesh refinement "is not important for the global response of the brace but plays a significant role in the determination of the inelastic deformations at the critical brace sections" [13].

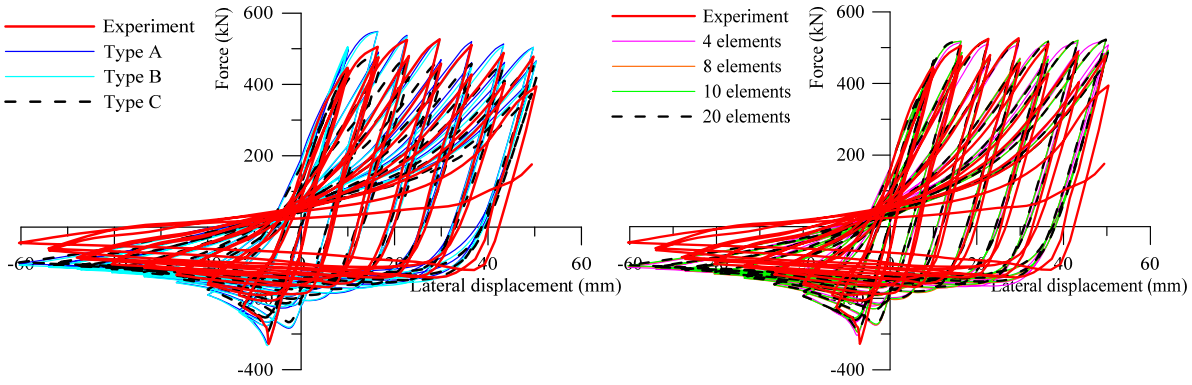

Figure 6. The Effect of Modelling Parameters on the Hysteresis Response of an S1B Specimen: a) Types of Fiber Discretization Technique; b) Number of Elements.

4.4 The Effect of the Number of Elements and Integration Points

To emphasize the importance of the number of distributed nonlinear beam-column elements along the HSS brace length, n_e, in this study, a suit of 4, 8, 10 and 20 elements with 4 integration points per element and fiber discretization technique type *C* are considered in order to simulate the brace response. Here, 500 fibers were assigned within the HSS cross-section and the out-of-straightness was set at $L_b/500$. As illustrated in Figure 6b, the number of elements selected to replicate the nonlinear response of S1B brace specimen has a small effect on the buckling force prediction and the global brace response. When the brace model is not loaded to failure, the use of eight nonlinear beam-column elements with four integration points per element and fiber discretization technique type *C* is sufficient to capture the fitted curvature during the nonlinear response, while the model

requires less computation time. Nonetheless, to capture the brace fracture, a minimum of 16 elements are required [3], although 20 are recommended [13] when the strain fatigue model is employed. However, by increasing the number of beam-column elements, the computation time increases as well. The number of integration points is not a sensitive parameter, but a minimum of three integration points per element are recommended [13,20,26].

4.5 The Effect of Fatigue Material Parameters on Brace Strain Life

The strain fatigue model that was proposed by Uriz [13] is based on cumulative damage. To reduce the volume of computations, a simplified rainflow cyclic counting technique was set in the formulation of fatigue material, which requires the calibrated value of material parameters as input. To validate the consistency of recommended constant values: $\varepsilon_0 = 0.095$ and $m = -0.5$, all specimens illustrated in Table 1 were replicated and assessed against the test results. Here, braces were modelled with 20 nonlinear beam-column elements with distributed plasticity, 4 integration points per element, fiber discretization technique type *C* with 500 fibers within the HSS cross-section and an initial out-of-straightness of $L_b/500$. Each end-gusset plate was simulated by two rotational and one torsional spring that were assigned in the zero-length element. Fatigue material was wrapped around the Giuffre-Menegoto-Pinto steel material assigned to brace and defined with 1% strain hardening for all braces, except one, the S1QB specimen for which a 5% strain hardening, was considered. In this study, $m = -0.5$ was treated as constant, whereas ε_0 was calibrated against experimental test results. To do this, its value varied until the simulated test had undergone the same number of cycles upon fracture as the experimental tests. The demanded failure strain for a single reversal, ε_0 that was required as input parameter in the definition of fatigue material and calibrated to match the experimental test results, is noted here $\varepsilon_{0,sim}$ and is provided for all specimens in Table 2. To understand the variation of accumulated strain at brace fracture, the behaviour of four HSS brace specimens given in Table 1 that were subjected at different displacement loading histories, and are characterized by different slenderness ratios and width-to-thickness ratios is displayed in Figure 7.

In this regard, the consistency of material parameters that were proposed by Uriz was investigated against experimental test results. Thus, by modelling the response of specimen S1B under displacement loading H_1, it was observed that the OpenSees model failed before the physical test, whereas the last four simulated cycles showed unstable loops as illustrated in Figure 7a. To match the experimental test response, the $\varepsilon_{0,sim}$ value was increased from 0.095 to 0.13, whereas the fatigue ductility exponent $m = -0.5$ remained constant. Conversely, when Uriz's fatigue material parameters' values [13] were used to replicate the response of the S1QB specimen, the OpenSees model did not fail during the last cycle and was able to undergo two more cycles of maximum amplitude that were fictitiously added to extend the initial loading history *Q* (Figure 7b). To match the experimental test, the $\varepsilon_{0,sim}$ value was decreased from 0.095 to 0.0665. The difference between the two demanded failure strain values (0.13 for S1B and 0.0665 for S1QB) is explained by the effect of the loading history on the brace response, which influences the development of strain in the cross-sectional fibers of the HSS brace at the plastic hinge location, although both specimens S1B and S1QB have the same slenderness ratio and width-to-thickness ratio.

In the second example, the effect of brace slenderness ratio on the demanded failure strain for a single reversal value, $\varepsilon_{0,sim}$ is emphasized. Thus, in case of specimens 2A and S3B, the slenderness ratio varies by a factor of 2.7 (53.3 for 2A versus 143.5 for S3B), whereas the width-to-thickness ratio shows a 20% variation (Table 2). By using $\varepsilon_0 = 0.095$ as input, the simulated S3B model was able to exhibit a lower number of cycles than the experimental test. In order to display the same number of cycles, a value that was twice as large ($\varepsilon_{0,sim} = 0.19$) was required. However, when $\varepsilon_0 = 0.095$ was considered to define the fatigue material assigned to specimen 2A, the simulated

response did not reach failure. Although two more virtual cycles of the same amplitude as the last cycle were added to the loading history, the simulated brace response showed strength degradation in tension and compression, without reaching failure. The last two hysteresis loops are depicted by a blue dashed-line in Figure 7d. To exhibit the same number of hysteresis cycles upon fracture as in the experimental test, the required value was $\varepsilon_{0,sim} = 0.067$. Thus, the demanded failure strain for a single reversal is larger for slender braces and decreases for stocky braces. It was noted that the S3B specimen was subjected to a smooth symmetric quasi-static cyclic loading, whereas specimen 2A was loaded to an asymmetric displacement history with large amplitudes in compression as shown in Figure 2d.

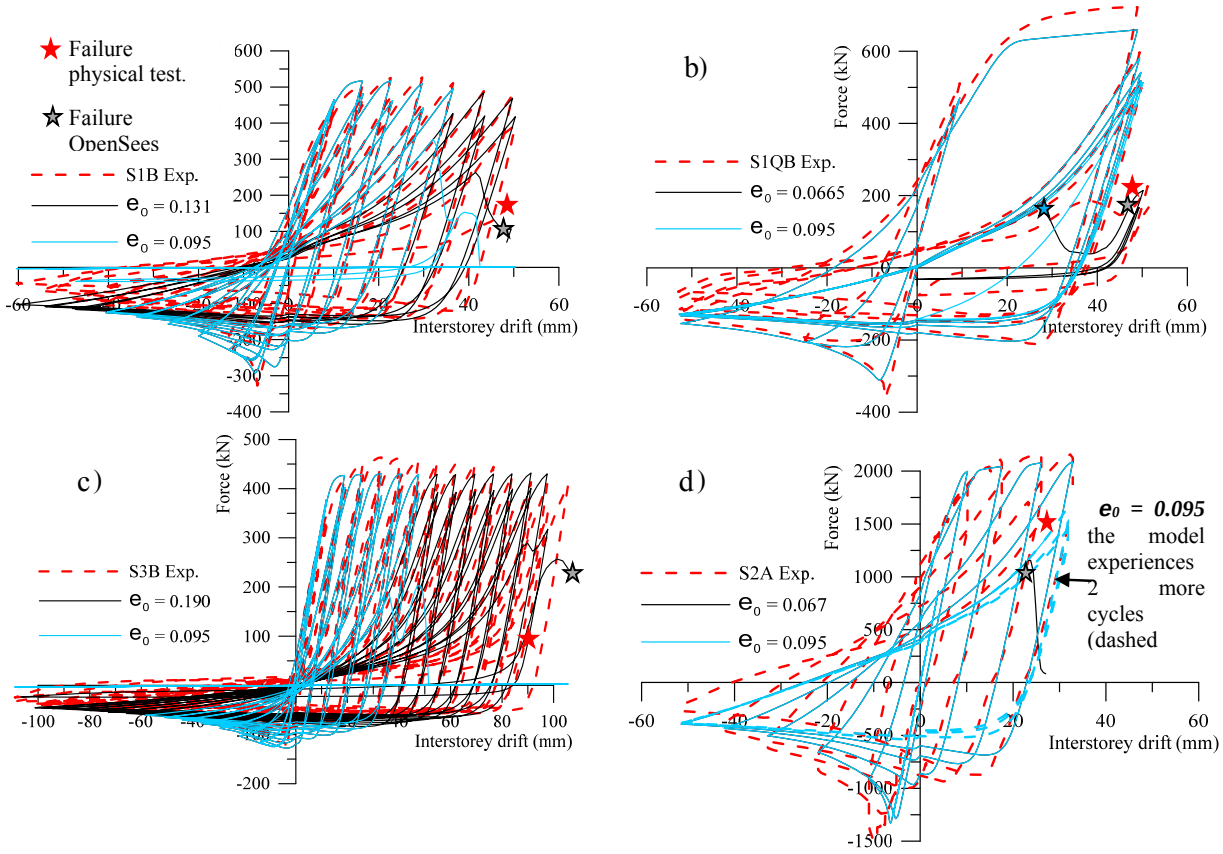

Figure 7. The Influence of Fatigue Material Parameters Values on Brace Response: a) S1B specimen, b) S1QB specimen, c) S3B specimen, d) 2A specimen.

In the third example, the effect of width-to-thickness ratio on the brace response is presented. Herein, specimens 3A, 3B and 3C were selected because of their similar slenderness ratios (an average of 64) and different width-to-thickness ratios. Although, specimen 3A is non Class 1 ($b_0/t > (b_0/t)_{limit}$ by 11%) it has a width-to-thickness ratio that is about twice as large as than that of specimen 3C (Table 2). To match the experimental test results, the demanded $\varepsilon_{0,sim}$ value is 129% larger for 3C than that for 3B and about 198% larger than that of 3A as illustrated in Table 2. These results are in agreement with Eq. 3, which shows a positive power for b_0/t. Thus, the failure strain for a single reversal parameter, ε_o, is sensitive to the slenderness ratio and width-to-thickness ratio, as well as the type of applied loading and steel strength. Using a smaller ε_o value than required may result in a conservative response (the model fails before the physical test), whereas using a larger value, the model dissipates more energy than the physical test.

5. BRACE FRACTURE MODELS

5.1 Predicted Material Parameters Values for the Strain Fatigue Model

In this study, Uriz's strain fatigue model is considered to simulate brace fracture in OpenSees, when the set of values assigned to material parameters m and ε_o are *-0.5* and $\varepsilon_{o,pred}$. To find the expression of predicted strain for a single reversal, $\varepsilon_{o,pred}$ is the main objective. By analyzing the variation tendency of $\varepsilon_{0,sim}$ that is seen for all specimens in Table 2, an ascendent demand with respect to slenderness ratio was observed. Thus, for square HSS specimens with similar width-to-thickness ratios (e.g., $b_0/t \sim 12.00$ and about 80% of $(b_0/t)_{\text{limit}}$) and different slenderness ratios, such as: 141.8 for S3B, 77 for Lee-5, 65.8 for 3B, 59.7 for 4B and 52.4 for 2B, the demanded $\varepsilon_{0,sim}$ value decreases from 0.19 for the slender specimen, S3B, to 0.077 for the stocky specimen, 2B. However, for square HSS specimens with $(b_0/t) \sim (b_0/t)_{\text{limit}}$ (e.g., 2A and 4A) or those non Class 1 (e.g., Lee-1 and 3A), the slenderness ratio seems to have a small effect on the demanded failure strain for a single reversal value, $\varepsilon_{o,sim.}$ In addition, the E/F_y ratio that is shown in Table 2, also has a slight effect on the brace fracture life. For all 12 square HSS specimens that appear in Table 2, the variation in the design parameters b_o/t, kL/r and E/F_y is expressed by the coefficient of variation and the resulted values are: 41.69% for kL/r, 24.83% for b_o/t and 11.38% for E/F_y.

Table 2. Brace Properties, Cumulative Strain, Strain-range and End-rotation at the Onset of Fracture

Test no.	*Size*	b_0/t	KL/r	E/F_y	$\varepsilon_{0,sim}$	$\varepsilon_{0,sim}/\varepsilon_{0,pred(Eq9)}$	$max\,\varepsilon_{rg,sim}$	$max\,\varepsilon_{rg,sim}/max\,\varepsilon_{rg,pred}$	$\theta_{f,sim}$	$\theta_{f,sim.}/\theta_{f,\,pred.}$
S1B	76x127x4.8	22.45	93.0	535.4	0.131	1.535	0.059	1.537	0.186	0.915
S1QB	76x127x4.8	22.45	93.2	535.4	0.067	0.784	0.040	1.092	0.175	0.864
S3B	76 x 76x4.8	11.83	141.8	563.3	0.190	1.049	0.102	2.456	0.265	1.078
S3A	76 x 76x4.8	11.83	143.5	565.3	0.180	0.984	0.072	1.741	0.233	0.947
1B	127x127x8.0	11.88	53.9	453.7	0.090	1.181	0.046	0.865	0.206	1.123
2A	152x152x8.0	15.00	53.3	457.0	0.067	1.015	0.041	0.837	0.193	1.109
2B	152x152x9.5	12.00	52.4	443.4	0.077	1.033	0.043	0.810	0.212	1.170
3A	127x127x6.4	17.80	64.8	414.3	0.058	0.778	0.035	0.786	0.191	1.045
3B	127x127x8.0	11.88	65.8	453.7	0.089	0.974	0.037	0.740	0.203	1.041
3C	127x127x9.5	9.40	61.6	414.4	0.115	1.165	0.038	0.710	0.234	1.168
4A	152x152x8.0	15.00	63.5	432.1	0.066	0.857	0.035	0.759	0.180	0.980
4B	152x152x9.5	12.00	59.7	432.1	0.078	0.938	0.037	0.736	0.211	1.120
Lee-1	5x5x0.188	22.40	58.0	469.0	0.056	1.000	0.041	0.997	0.135	0.816
Lee-5	4x4x0.250	11.88	77.0	392.0	0.124	1.269	0.064	1.428	0.234	1.145
Mean (12 specimens)*		13.57	74.6	457.5	0.099	1.020	0.049	1.072	0.208	1.061
Standard deviation		3.37	31.1	52.02	0.043	0.131	0.019	0.496	0.0315	0.100
St. dev./ Mean %		24.83	41.69	11.38	43.63	12.84	39.47	46.26	15.14	9.42

*Only the 12 square HSS specimens are considered.

Based on the foregoing, in this study, the following regression equation is proposed in order to predict the failure strain for a single reversal value that is available for square HSS braces whose slenderness ratio vary from 50 to 150:

$$\varepsilon_{0,pred.} = 0.006\left(\frac{kL}{r}\right)^{0.859}\left(\frac{bo}{t}\right)^{-0.6}\left(\frac{E}{F_y}\right)^{0.1} \quad (9)$$

In comparison to Eq. 3, which was provided for HSS braces with *KL/r* < *85*, the slenderness ratio in the above equation was considered to have a positive power, whereas a similar weight was maintained by E/F_y and with-to-thickness ratio. The series of $\varepsilon_{0,pred}$ values is illustrated in Figure 8 versus the simulated values, $\varepsilon_{0,sim}$, whereas the $\varepsilon_{0,sim}/\varepsilon_{0,pred}$ ratio is given for all specimens in Table 2. Thus, a good match was observed for braces with a square HSS cross-section, but for braces with a rectangular HSS cross-section, the addition of a 4th parameter d_o/t to negative power is required.

To validate the predicted failure strain for a single reversal value, $\varepsilon_{0,pred}$, computed from Eqs. 3 and 9, the simulated hysteresis loops that resulted for specimens 2A and 3B are depicted in Figures 9a and 9b, respectively, versus the experimental test results. Here, the $\varepsilon_{0,pred}$ computed from Eq. 3 is 0.051 for specimen 2A and 0.052 for 3B, whereas *m = -0.3,* was constant. As depicted, both sets of predicted material parameters value: (*m = -0.3* and $\varepsilon_{o,pred\text{-}Eq.3}$) and (*m = -0.5* and $\varepsilon_{o,pred\text{-}Eq.9}$) that were used as input in the assigned fatigue material are able to simulate the brace response when tensile fracture occurs. However, when the simulated response of 3B specimen that displays a 24% larger slenderness ratio than of the 2A specimen was investigated, a better match was obtained when the $\varepsilon_{o,pred\text{-}Eq.9}$ was employed. Conversely, using *m = -0.3* and $\varepsilon_{o,pred\text{-}Eq.3}$ caused the replicated response to be underestimated by two cycles as shown in Figure 9b.

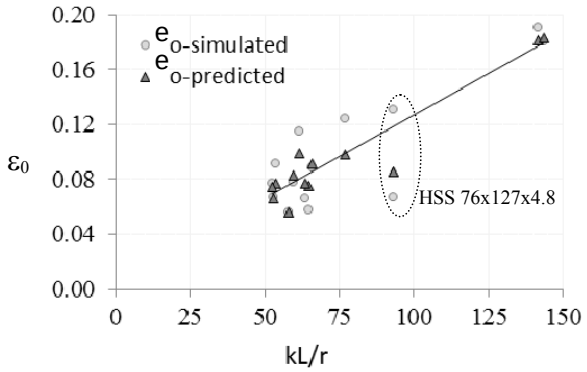

Figure 8. Simulated versus Predicted Strain for a Single Reversal against the Slenderness Ratio.

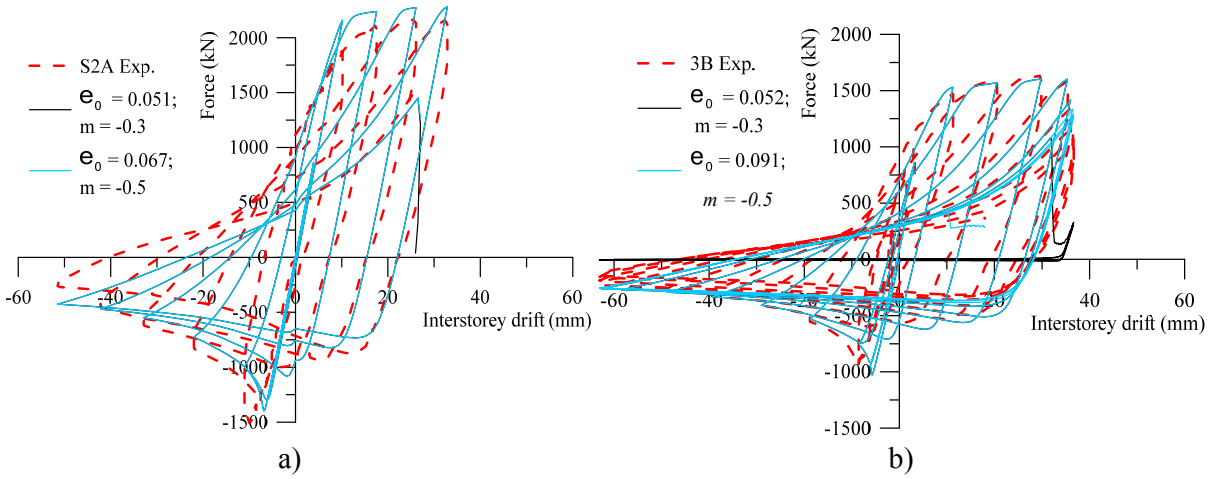

a) b)

Figure 9. Brace Fracture Simulation Based on the Strain Predicted from Eqs. 10 and 3 vs. Experimental Test Results: a) 2A specimen; b) 3B specimen.

5.2 Comparisons with the Existing Strain-Range and End-Rotation Brace Fracture Models

The simulated tensile and compressive strain history, recorded at two extreme fibers of the HSS corner cross-section, located at the brace's mid-length and schematically illustrated in Figure 3a, is plotted in Figure 10 for S1B, S1QB and 2A specimens. As depicted, the tensile fibers have accumulated a limited range of tensile strains per cycle, whereas the compressive fibers experienced a greater accumulated strain-range, as well as a greater maximum strain-range throughout the loading history. Based on this observation, Hsiao et al. [3] proposed the strain-range brace fracture model, where the maximum strain-range developed during the loading history in the compressive fiber of the HSS corner cross-section located at the brace's mid-length is recorded. For all specimens, the simulated maximum strain-range value, $max.\varepsilon_{rg}$ that is obtained throughout the loading history is shown in Table 2, as well as the ratio of simulated to the predicted maximum strain-range that was computed from Eq. 4. Furthermore, Figure 11a illustrates both series of simulated and predicted maximum strain ranges throughout the loading history at the onset of brace fracture against the slenderness ratio of given specimens. As shown, a good match is observed for the predicted $max.\varepsilon_{rg.}$value computed for stocky braces, while for slender braces, such as S3A and Lee-5, the ratio $max\varepsilon_{rg,sim.}/\ max\varepsilon_{rg,pred}$ is 1.741 and 1.428, respectively. For slender braces, the simulated strain-range magnitude is close to the predicted value obtained from Eq. 4, when the

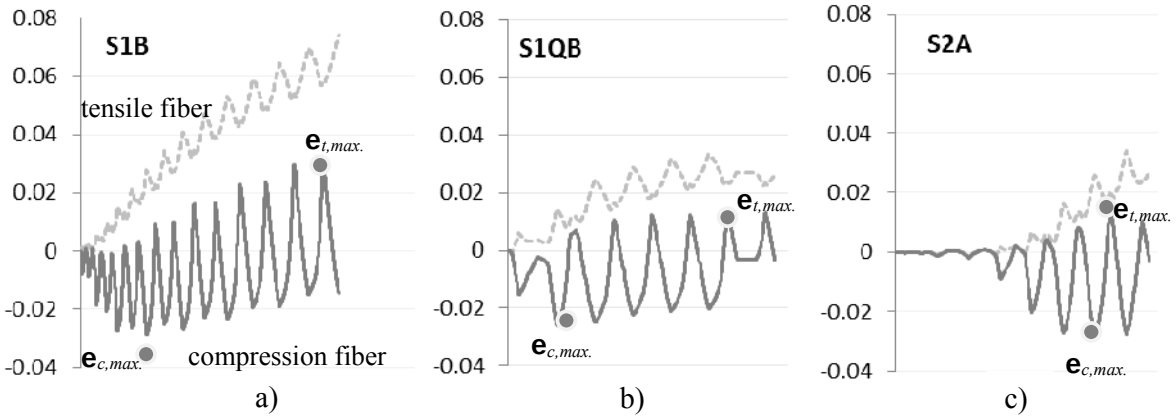

a) b) c)

Figure 10. Strain History of Tensile and Compression Fibers Recorded at the HSS Corner of the Braces's Mid-Length Cross-Section: a) S1B; b) S1QB; c) 2A.

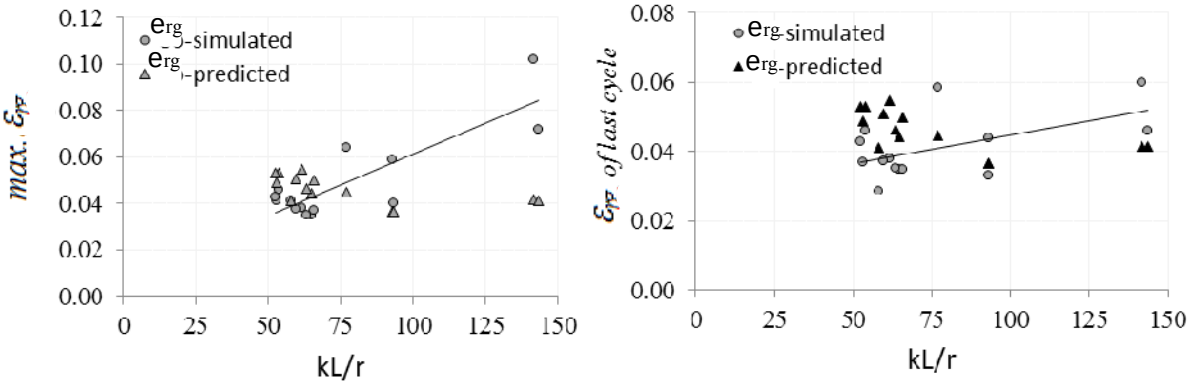

a) b)

Figure 11. Simulated vs. Predicted Strain-Range Against Slenderness Ratio: a) Maximum Strain-Range; b) Strain-Range of Cycle Prior Failure.

cycle prior failure is considered, instead of the whole strain-range history (Figure 11b). As illustrated in Figures 10a and 10b, the development of strain history and, implicitly, the strain life of brace members vary with the type of applied loading history. To link the strain history to the maximum out-of-plane brace deformation, *e*, Figures 12a and 12b illustrate the simulated deformation response of specimens S1B and S1QB. Although, both braces are able to undergo similar out-of-plane deflection, the strain developed in the extreme compression fiber of the HSS corner cross-section shows a different strain history path. This effect is explained by the microplastic deformation that is induced by the cyclic plastic strain in the steel material, whereas the changes affecting the mechanical properties of material have secondary influence [32]. In addition, the compressive stress relaxation that is contributed by strain reversal inhibits the crack nucleation. As seen in Figures 10 and 12, the strain in the extreme compression fiber of HSS corner cross-section varies for each cycle, *i*, between $(\varepsilon_c)_i$ and $(\varepsilon_t)_i$. When the total strain per cycle ($(\varepsilon_c)_i + (\varepsilon_t)_i$) remains in compression for several adjacent cycles, as is the case of specimens 2A (Figures 10c and 12d) and S1QB (Figures 10b and 12b), the strain life is reduced. For example, the ratio of the accumulated strain in compression $\Sigma(\varepsilon_c)_i$ to the accumulated strain in tension $\Sigma(\varepsilon_t)_i$, that is developed in the extreme compression fiber is 1.82 for the S1B specimen and 2.78 for the S1QB specimen. When compared, the slender braces (e.g., S3B, S3A) show light development of compression strain, especially in the first part of the applied loading history (Figure 12c). After that, the compression strain that is developed is inhibited by tensile strain and the specimen experiences a longer strain life.

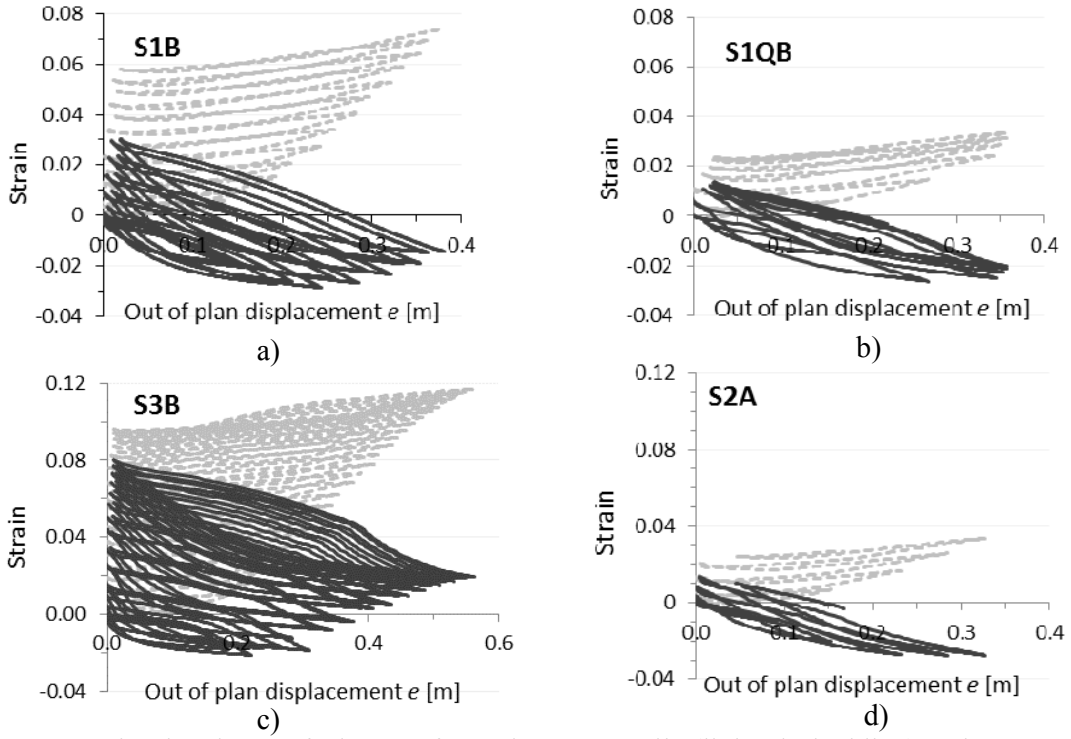

Figure 12. Simulated Out-of-Plane Deformation vs. Tensile (light, dashed line) and Compression (dark, solid line) Strain Developed in Braces: a) S1B; b) S1QB; c) S3B; d) 2A.

Furthermore, brace members that are subjected to a loading history applied first in tension (e.g., S3A vs. S3B) exhibit reduced residual lateral displacement. Thus, a correlation of maximum brace deformation at the onset of fracture and the accumulated strain or maximum strain-range computed in the compressive fiber of the HSS brace cross-section is observed.

The simulated time-history series of maximum out-of-plane brace deformation, e, is plotted for specimens S1B and S3B against the interstorey drift, Δ (Figure 13). Although local buckling is not considered in the model, the out-of-plane brace deflection versus interstorey drift, which is expressed as $\Delta/H\%$ where H is the storey height, does not seem to be affected during the inelastic cyclic excursions prior to failure [20]. By replicating the specimens behaviour with and without the consideration of fatigue material, small differences are observed in the magnitude of brace deflection. However, the failure of the brace at the onset of fracture is strongly influenced by the value of material parameters that are used as input in the definition of fatigue material. Based on the displacement ductility of HSS braces, Tremblay et al. [15] proposed the end-rotation of brace causing fracture model, where the end-rotation is measured at the onset of brace fracture, $\theta_{f,pred.}$, as per Eq. 5. The simulated end-rotation value, $\theta_{f,sim}$, together with the ratio $\theta_{f,sim}/\theta_{f,pre.}$, are given in Table 2. Both series of simulated and predicted end-rotation of brace at fracture versus slenderness ratios are illustrated for all specimens in Figure 14. A good match is seen.

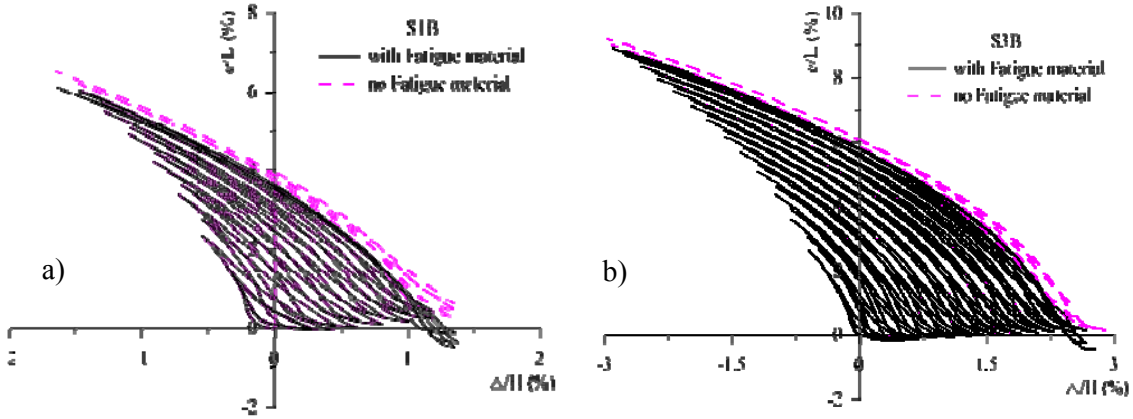

Figure 13. Simulated Out-of-Plane Deformation vs. Interstorey Drift: a) S1B; b) S3B.

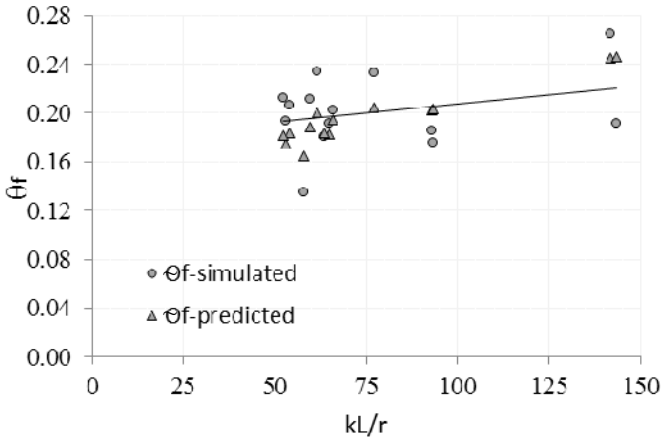

Figure 14. Simulated vs. Predicted End-Rotation of Braces at Fracture Against Slenderness Ratio.

To summarize, statistical results such as the mean, the standard deviation and the coefficient of variation are calculated in order to evaluate the ratio of simulated to predicted values that is obtained by employing the strain fatigue, strain-range and end-rotation brace fracture models. Due to the large variation in design parameters, especially in the slenderness ratio that showed a variation of 41.69%, the demanded strain for a single reversal parameter that fits the experimental tests, $\varepsilon_{0,sim,}$ exhibits a coefficient of variation in the same range, 43.63%. A similar coefficient of variation, 39.47%, was obtained for the fitted maximum strain-range parameter, $max\varepsilon_{rg,sim}$. By

using the predicted failure strain computed from the equation proposed in this study (Eq. 9) or the predicted end-rotation of brace at fracture resulted from the equation proposed by Tremblay et al. [15] a good match was obtained. Thus, for the 12 selected square HSS brace specimens, the coefficient of variation is 12.84% and 9.42% for the ratios $\varepsilon_{0,sim}/\varepsilon_{0,pred}$ and $\theta_{f,sim}/\theta_{f,pred}$, respectively. As seen in Table 2, there is a large difference between the coefficient of variation of 15.14% calculated for the simulated end-rotation of brace at fracture, $\theta_{f,sim}$ and that of 46.63% computed for the failure strain $\varepsilon_{0,sim}$. However, for the strain-range fracture model, the coefficient of variation is 46.26%. This brace fracture model gives a greater dispersion for slender braces, such as S3A and S3B. In this regard, the coefficient of variation dropped to 26.66% when both slender specimens were removed. By using 44 specimens from the literature with a mean slenderness ratio of 67.6 and 19.8% coefficient of variation, Hsiao et al. [3] reported a coefficient of variation of 15.7% for the strain-range fracture model employed. In Figure 11 there seems to be a slight negative trend of strain-range for specimens with $kL/r < 65$. However, this trend becomes ascendent for specimens that have a larger slenderness ratio.

6. CONCLUSIONS

To analyze the nonlinear seismic response of concentrically braced frame building structures, an accurate brace fracture model prior to and beyond fracture is required. According to the CSA/S16-2009 standard, HSS braces behaving in tension/compression should be Class 1 sections and respond to a slenderness ratio kL/r that is lower than 200, but not less than 70 for braces of CBF buildings that are located in seismic areas, whereas the short period spectral acceleration ratio is equal to or greater than 0.75. When using the strain fatigue model to simulate HSS brace fracture in OpenSees, the failure strain for a single reversal value is required as input parameter. Thus, in this study, a regression equation was proposed to compute the predicted failure strain value for square HSS braces whose slenderness ratio is between 50 and 150. For calibration, 14 experimental test results found in the literature that have experienced failure fracture under large out-of-plane displacement were replicated. All selected specimens correspond to a wide range of brace parameters and types of loading history. The brace member was modelled here using nonlinear beam-column elements with spread plasticity and discretized fiber formulation. In this study, the impact of modelling parameters on the nonlinear response of braces is also discussed. Comparisons with existing brace fracture models such as strain-range and end-rotation of brace are also provided. The conclusions of this research are as follows:

- The strain fatigue model that was implemented by Uriz in the formulation of fatigue material is able to simulate the brace response at the onset of fracture. In this study, the assigned fatigue material parameters m and ε_o receive as values -0.5 and $\varepsilon_{o,pred}$, respectively. To predict the value of failure strain for a single reversal parameter, $\varepsilon_{o,pred}$, a regression equation, developed for square HSS braces whose slenderness ratio is between 50 and 150 was proposed. The variables in the equation are: slenderness ratio, width-to-thickness ratio and yield strength. By compiling the results from 12 experimental tests conducted on pin-ended square HSS brace members, a coefficient of variation of 12.84% for the ratio $\varepsilon_{0,sim}/\varepsilon_{0,pred}$ was obtained. For Class 1 specimens, the $\varepsilon_{0,sim}$ value varies from 0.066 to 0.19 with a mean of 0.099 that is close to the recommended Uriz's value (0.095). For non Class 1 specimens the simulated failure strain dropped to 0.056.
- Based on the same strain fatigue model, the set of material parameters value that were proposed by Lignos and Karamanci ($m = -0.3$ and $\varepsilon_{o,pred}$) for HSS braces whose slenderness ratio is between 27 and 85 was evaluated. A good prediction for braces with a slenderness ratio that is less than 65 was achieved. For those with larger slenderness ratios, the predicted strain for a single reversal value is underestimated by one or two cycles.

- From comparisons with the existing end-rotation of brace fracture model, the coefficient of variation is slightly larger (12.84% versus 9.42%). This is explained by the large difference between the coefficient of variation of 15.14% calculated for the simulated end-rotation of brace at fracture, $\theta_{f,sim}$ and that of 46.63% computed for the simulated failure strain $\varepsilon_{0,sim}$.
- The existing strain-range brace fracture model is based on the maximum strain range of compressive fiber throught the entire history. This model shows larger dispersion for slender HSS braces and a good correlation for stocky braces, especially for those with a slenderness ratio that is lower than 65. However, for slender braces a good match was obtained when the strain range of the cycle prior failure was recorded. The coefficient of variation computed for the ratio $max\varepsilon_{rg,sim.}/max\varepsilon_{rg,pred}$ dropped to 26.66% after the slender specimens, S3A and S3B, were removed.
- The effect of loading history type on the strain life of braces is explained by the microplastic deformations that are induced by the cyclic plastic strain in the steel material, while the changes affecting the mechanical properties of material have a secondary influence. In addition, the compressive stress relaxation that was contributed by strain reversal inhibits the crack nucleation. Meanwhile, brace members that are subjected to the loading history applied first in tension (e.g. S3A) exhibit reduced residual lateral displacement. However, the strain life of HSS brace members subjected to cyclic axial deformations is highly influenced by the slenderness ratio. Thus, braces with larger slenderness ratios and lower width-to-thickness ratios have a longer strain life because are able to avoid the initiation of premature fracture.

ACKNOWLEDGMENTS

The authors would like to thank Professors Robert Tremblay and Tom Brown for providing their experimental test results. The financial support provided by the Natural Sciences and Engineering Research Council of Canada is gratefully acknowledged.

REFERENCES

[1] CSA. CAN/CSA-S16-09, “Limit States Design of Steel Structures”, Rexdale, Ontario, Canadian Standard Association, 2009.

[2] Lehman, D.E., Roeder, C. W., Herman, D., Johnson, S., Kotulka, B., “Improved Seismic Performance of Gusset Plate Connections”, Journal of Structural Eng., ASCE, 2008, Vol. 134, No. 6, pp. 890-901.

[3] Hsiao, P.C., Lehman, D., Roeder, C., “A Model to Simulate Special Concentrically Braced Frames Beyond Brace Fracture”, Journal of Earthquake Engineering and Structural Dynamics, 2013, Vol. 42, pp. 182-200.

[4] Lee, S. and Goel, S.C., “Seismic Behavior of Hollow and Concrete-filled Square Tubular Bracing Members”, Research Report UMCE 87–11, Department of Civil Engineering, University of Michigan, Ann Arbor, MI, 1987.

[5] Archambault, M.H., “Etude du Comportement Seismique des Contreventements Ductile en X avec Profiles Tubulaires en Acier”, Report no. EPM/GCS-1995-09, Montreal, Canada, Ecole Polytechnique, 1995.

[6] Shaback, B. “Behaviour of Square HSS Braces with end Connections under Reversed Cyclic Axial Loading”, Master thesis in the Dep. of Civil Eng., University of Calgary, Calgary, 2001.

[7] Shaback, B. and Brown, T., “Behaviour of Square Hollow Structural Steel Braces with end Connections under Reversed Cyclic Axial Loading”, Canadian J. of Civil Engineering,

2003, Vol. 30, No. 4, pp. 745-753.
[8] Yang, T.Y. and Mahin, S., "Limiting Net Section Fracture in Slotted Tube Braces", Steel Tips, Structural Steel Education Council, Orinda, Ca., 2005.
[9] Fell, B.V., Kanvinde, A.M., Deierleine, G.G., Myers, A.M., Fu, X., "Backling and Fracture of Concentric Braces under Inelastic Loading", Steel Tips, Tehnical Information and Product Service, Structural Steel Education Concil, Moroga, CA., 2006.
[10] Han, S.M., Kim, W.T., Foutch, D.A., "Seismic Behaviour of HSS Bracing Members According to Width-thickness Ratio under Symmetric Cyclic Loading", J. Struct. Eng., 2007, Vol. 133, No. 2, pp. 264-273.
[11] Tremblay, R., "Inelastic Seismic Response of Steel Bracing Members", Journal of Constructional Steel Research, 2002, Vol. 58, pp. 665-701.
[12] Lee, K. and Bruneau, M., "Energy Dissipation of Compression Members in Concentrically Braced Frames: Review of Experimental Data", Journal of Structural Engineering, ASCE, 2005, Vol. 131, No. 4, pp. 552-559.
[13] Uriz, P. and Mahin, S., "Toward Earthquake Resistant Design of Concentrically Braced Steel Frame Structures", PEER Report 2008/08.
[14] Uriz, P., "Towards Earthquake Resistant Design of Concentrically Braced Steel Buildings", Ph.D. Dissertation, University of California, Berkeley, 2005.
[15] Tremblay, R., Archambault, M.H., Filiatrault. A., "Seismic Response of Concentrically Braced Steel Frames Made with Rectangular Hollow Bracing Members", Journal of Structural Eng., ASCE, 2003, Vol. 129, No. 12, pp.1626-1636.
[16] Mazzoni, S., McKenna, F., Scott, M., Fenves, G. et al., "OpenSees User Manual", 2007, opensees.berkeley.edu/OpenSees/manuals/usermanual/OpenSeesCommandLanguageManu
[17] Santagati, S., Bolognini, D., Nascimbene, R., "Strain Life Analysis at Low-cycle Fatigue on Concentrically Braced Steel Structures with RHS Shape Braces", J. Earthquake Eng., 2012, Vol.16 (S1), pp. 107-137.
[18] Salawdeh, S. and Goggins, J., "Numerical Simulation for Steel Brace Members Incorporating a Fatigue Model", Engineering Structures, 2013, Vol. 46, pp. 332-349.
[19] Lignos, D. and Karamanci, E., "Predictive Equations for Modelling Cyclic Buckling and Fracture of Steel Braces", 10th International Conference on Urban Earthquake Engineering, March 1-2, 2013, Tokyo Institute of Technology, Tokyo, Japan, 2013.
[20] Tremblay, R., "Influence of Brace Slenderness on the Fracture Life of Rectangular Tubular Steel Bracing Members Subjected to Seismic Inelastic Loading", Proc. 2008 ASCE Structures Congress, Vancouver, BC., 2008.
[21] Hsiao, P.C., Lehman, D., Roeder, C., "Improved Analytical Model for Special Concentrically Braced Frames", Journal of Constructional Steel Research, 2012, Vol. 73, pp.80-94.
[22] ASTM. ASTM E 1049–85," Standard Practices for Cycle Counting in Fatigue Analysis", West Conshohocken, PA, 2003.
[23] Xue, L., "A Unified Expression for Low Cycle Fatigue and Extremely Low Cycle Fatigue and its Implication for Monotonic Loading", International Journal of Fatigue 2008, Vol. 30 (10–11), pp. 1691–1698.
[24] Manson, S., "Fatigue: A complex Subject - some Simple Approximations", Experimental Mechanics, 1965, Vol. 5, No. 7, pp. 193-226.
[25] Coffin, L., "A Study of the Effect of Cyclic Thermal Stresses on a Ductile Metal", Trans ASME, 1954, Vol. 1954, No. 76, pp. 931–950.
[26] Uriz, P., Filippou, F.C., Mahin, S., "Model for Cyclic Inelastic Buckling of Steel Braces", Journal of Structural Engineering, ASCE, 2008, pp. 619-628.
[27] Aguero, A., Izvernari, C., Tremblay, R., "Modelling of the Seismic Response of Concentrically Braced Steel Frames Using the OpenSees Analysis Environment", International Journal of Advanced Steel Construction, 2006, Vol. 2-3, pp. 242-274.

[28] Scot, M.H. and Fenves, G.L., "Plastic Hinge Integration Methods for Force-based Beam-column Elements", Journal of Structural Engineering, 2006, Vol. 132, No. 2, pp. 244-252.

[29] Yoo, J.H., Lehman, D., Roeder, C., "Influence of Gusset Plate Parameters on the Seismic Resistance of Braced Frames", J. of Constructional Steel Research, 2008, Vol. 64, pp. 607-623.

[30] Dicleli, M. and Mehta, A., "Simulation of Inelastic Cyclic Buckling Behaviour of Steel Box Sections", Computer and Structures Journal, 2007, pp. 446-457.

[31] Ziemian, R., "Guide to Stability Design Criteria for Metal Structures", J. Wiley & Sons, 2010.

[32] Li, S.J., Cui, T.C., Hao, Y.L., Yang, R., "Fatigue Properties of a Metastable b-type Titanium Alloy with Reversible Phase Transformation", Acta Biomaterialia Journal, Elsevier, 2008, Vol. 4, pp. 305-317.

FINITE ELEMENT ANALYSIS OF CFRP STRENGTHENED STEEL HOLLOW SECTIONS UNDER TENSION

Sabrina Fawzia[1] and Kaniz Shahanara[2]

[1, 2] *Science and Engineering Faculty, School of Civil Engineering and Built Environment, Queensland University of Technology, Brisbane 4000, Queensland, Australia*
**(Corresponding author: E-mail: sabrina.fawzia@qut.edu.au)*

Received: 2 December 2013; Revised: 19 June 2014; Accepted: 24 June 2014

ABSTRACT: This paper presents a nonlinear finite element (FE) model for the analysis of very high strength (VHS) steel hollow sections wrapped by high modulus carbon fibre reinforced polymer (CFRP) sheets. The bond strength of CFRP wrapped VHS circular steel hollow section under tension is investigated using the FE model. The three dimensional FE model by Nonlinear static analysis has been carried out by Strand 7 finite element software. The model is validated by the experimental data obtained from Fawzia et al [1]. A detail parametric study has been performed to examine the effect of number of CFRP layers, different diameters of VHS steel tube and different bond lengths of CFRP sheet. The analytical model developed by Fawzia et al. [1] has been used to determine the load carrying capacity of different diameters of CFRP strengthened VHS steel tube by using the capacity from each layer of CFRP sheet. The results from FE model have found in reasonable agreement with the analytical model developed by Fawzia et al [1]. This validation was necessary because the analytical model by Fawzia et al [1] was developed by using only one diameter of VHS steel tube and fixed (five) number of CFRP layers. It can be concluded that the developed analytical model is valid for CFRP strengthened VHS steel tubes with diameter range of 38mm to 100mm and CFRP layer range of 3 to 5 layers. Based on the results it can also be concluded that the effective bond length is consistent for different diameters of steel tubes and different layers of CFRP. Three layers of CFRP is considered most effective wrapping scheme due to the cost effectiveness. Finally the distribution of longitudinal and hoop stress has been determined by the finite element model for different diameters of CFRP strengthened VHS steel tube.

Keywords: Carbon fibre reinforced polymer (CFRP), Polymer, Finite element analysis (FEA), Analytical model, Joints and adhesive

1. INTRODUCTION

Civil infrastructure in Australia represents a substantial amount of investment and is essential to the function and economic well-being of society. Current social and political pressure to maintain existing facilities in service for extended periods of time are high because of the involvement of huge cost of replacing existing facilities. Engineers are facing a rising level of aging infrastructure which has, in turn, led them to implement new materials and techniques to efficiently combat this problem. Using non-ferrous materials in the form of carbon fibre-reinforced polymer (CFRP) sheets as external reinforcement for VHS steel tubular structures can provide extensive benefits including weight savings, high strength to weight ratio, resistance to corrosion, flexibility to form all kinds of shapes and ease of handling during construction. The outstanding properties of CFRP such as high strength, high elastic modulus, light weight and good durability have made them a suitable alternative to steel in strengthening work. CFRP's high strength-to-weight ratio has played a significant role in creating interest in strengthening, repair and rehabilitation of steel structures which has been demonstrated in a recent paper [2]. This review paper has covered wide area of CFRP strengthening of steel structure including hollow and concrete-filled steel tubes with external CFRP confinement. A comprehensive study on steel plates with double strap joint under tension has been done by the author Fawzia [3-6]. Although most columns should be in compression, sometimes they may be in tension under some load conditions such as wind uplift. Therefore research is needed for CFRP strengthened steel tube with double strap joint under tension load.

Experimental investigation on very high strength circular steel tubes strengthened by carbon fibre reinforced polymer subjected to axial tension has been conducted by Fawzia et al [1].VHS steel tube is popular due to its high strength (yield stress of around 1350 MPa and an ultimate strength of 1500 MPa), light weight and acceptable ductility [7]. High Modulus MBrace CF530 (640 GPa) and high strength epoxy Araldite 420 were used in the strengthening process of VHS steel tubes [1]. Several specimens with five layers of CFRP were tested in axial tension. Analytical model was developed to estimate the maximum load for a given CFRP arrangement based on the measured strain distribution across the CFRP layers. However, these experiments and the models were limited to one size of steel tube and 5 layers of CFRP [1].

In the present study an FE model has been developed for VHS steel hollow sections wrapped with CFRP sheets. The developed FE model was validated by the experimental data from Fawzia et at [1]. A detailed parametric study has been conducted by varying number of CFRP layers (3 to 5 layers), size of the steel hollow sections (diameters ranging 38mm to 100mm) and different bond length of CFRP sheet (5mm to 85mm). The results from FE models use to validate the analytical model developed by Fawzia et al [1] more widely. Finally the distribution of longitudinal and hoop stress has been established for different sizes of CFRP strengthened VHS steel tubes.

2. FINITE ELEMENT ANALYSIS (FEA)

In the present study a series of finite element models for circular hollow steel sections wrapped with CFRP sheet composites is developed. The simulation was done in Strand7 finite element software by running nonlinear FE analysis solver to account for the nonlinear properties of the materials.

In the models, a cylindrical coordinate system was selected. All materials were modelled as brick elements. Only a quarter of specimen was modelled for the symmetry of the sections. First cross sectional areas of all materials were created as plate element by adding nodes and then extruded along the longitudinal direction to represent the brick element.

Figure 1(a) shows the schematic of experimental specimen of circular hollow section with double strap joints under tension and Figure 1(b) shows the corresponding FE model in the longitudinal direction. Two steel tubes were joined together using adhesive at the joint and 5 layers of CFRP were applied in the joint with the aid of adhesive. The CFRP length L1 was kept shorter than L2 to make failure happen in shorter bond length side. The total length of the specimen was 800mm, diameter was 38mm, and the thickness varies from 1.6mm to1.84mm. As no noticeable changes were reported because of small changes in steel tube thickness [4], the steel thickness of 1.84 mm was considered in all FE models for simplicity. In FE model different layers of CFRP was created as individual layers to find the load carrying capacity of each layer. The thickness of CFRP sheets was 0.19mm according to the manufacturer data [8]. In the experiments, it was difficult to maintain constant thickness of CFRP layers throughout the bond length as constant thickness of adhesive used cannot be maintained. Therefore, the thickness of adhesive layers is measured at different locations and the average thickness (0.09mm) was used in all FE models.

Figure 2 represents the cross section of the sample in the FE model. Uniform displacement in the axial direction observed in the experimental test was applied in the FE model. This displacement data is factored in Strand 7 model to get a series of data to compare with experimental test until failure of the specimen. The FE model was validated using the experimental data from Fawzia et al.[1] and with the validated models a parametric study was carried out by varying number of CFRP layers (3 to 5), tube diameter (38 to 100mm) and CFRP bond length (5 to 85mm).

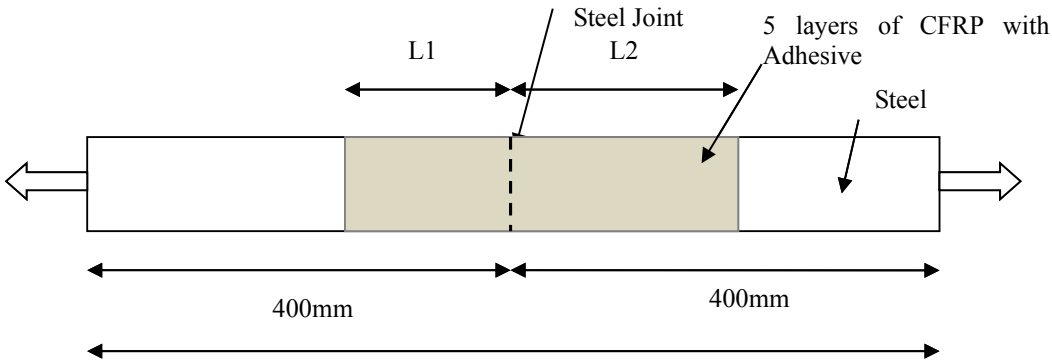

(a) Details of experimental specimen

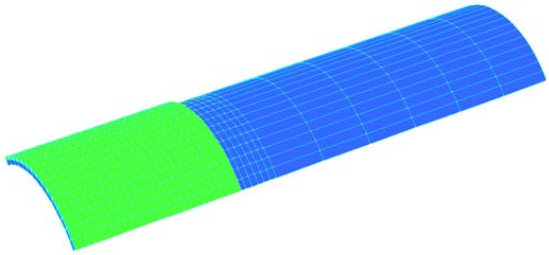

(b)FE model representation (one fourth model)

Figure 1. Schematics View of the Experimental Specimen and FE Model (Longitudinal Section)

3. MATERIAL PROPERTIES

In the present FE models, to match with the experimental investigation [1], MBrace high modulus fibre CF530, Araldite 420 adhesive and VHS steel tube were used. Similarly, all measured material properties from experimental study were used in the FE model. The summary of measured properties obtained from Fawzia et al [1] and Jiao and Zhao [9] are presented in Table 1.

4. FAILURE MODE AND ULTIMATE LOAD

In order to determine the deformation clearly, Strand7 uses information about the nominal size of the structure and automatically provide a reasonable displacement scale. Fig. 3 shows, by using 5% displacement scale from Strand 7 software. The failure mode was fiber break at the joint which was exactly same as the experimental failure mode shows in Figure 4.

The comparison of load carrying capacity between experimental [1] and FE results is shown in Table 2. It can be seen that there is reasonably good agreement between the experimental and the FE model results with mean =1.0325 and COV=0.1557.

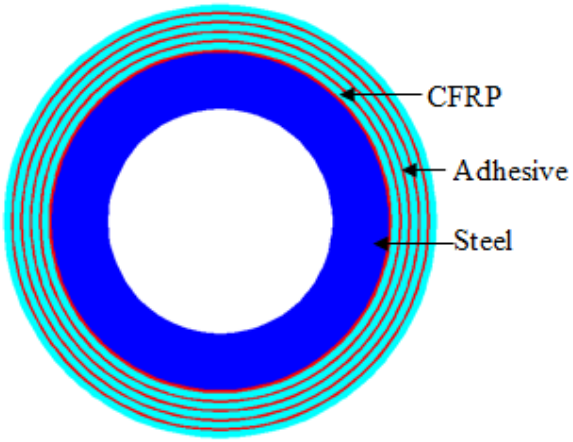

(a) Cross section of the FE model

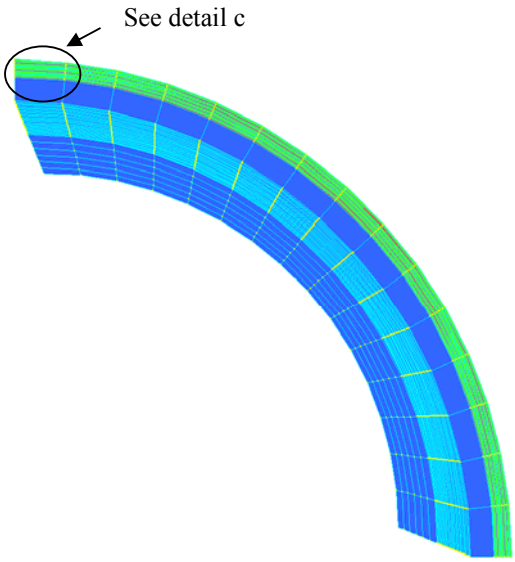

(b) One fourth model representation

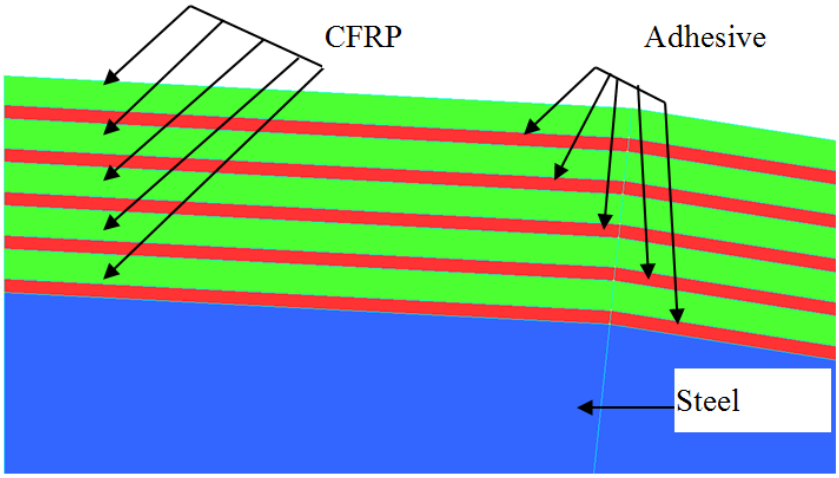

(c) Detail of One fourth model representation

Figure 2: FE model representation (cross section)

Table 1. Measured Material Properties by Fawzia et al [1] and Jiao and Zhao [9]

	CFRP	Steel	Adhesive
Tensile modulus (GPa)	475	200	1.9
Tensile strength (MPa)	1016	1500	28.6

Table 2. Comparison of Experimental (Fawzia et al[1]) and FE Results for VHS Circular Steel Tube

Specimens Level	D mm	t (mm)	Experimental Results		FE Model Results		$P_{u,FE}$ / $P_{u,EXP}$	Remarks
			Bond Length (mm)	$P_{u,EXP}$ kN	Bond Length (mm)	$P_{u,FE}$ kN		
M1	38.24	1.84	85	84.9	85	73.06	0.8605	Fibre Break
M3	38.30	1.79	65	74.1	65	73.53	0.9923	Fibre Break
M4	38.10	1.60	62	77.5	62	73.36	0.9466	Fibre Break
M5	38.27	1.74	50	67.3	50	72.73	1.0807	Fibre Break
M6	38.10	1.60	40	54.8	40	70.28	1.2825	Fibre Break
Mean							1.0325	
COV							0.1557	

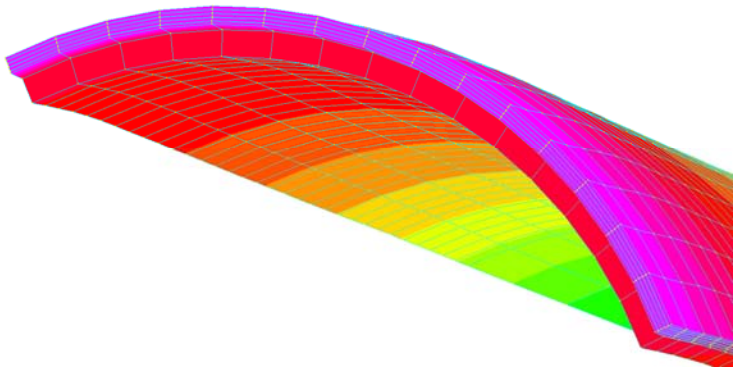

Figure 3. Failure Mode of the FE Specimen

5. EFFECTIVE BOND LENGTH

The ultimate load carrying capacity against the bond length is plotted in Figure 5. In this figure comparison between experimental results from Fawzia et al [1] and the results of FE model from same bond length specimens is presented. It can be seen that the load carrying capacity reaches a plateau after the bond length exceeds a certain value. This length, beyond which no significant increase in load carrying capacity will occur, is called the effective bond length.

It can also be seen from Figure 5 that the loads continue to increase with increase in the bond length. The ultimate load reaches a plateau after 50mm bond length. According to the definition of effective bond length, it can be concluded that effective bond length for 38mm diameter CFRP strengthened VHS steel tube is 50mm in both experimental [1] and FE model.

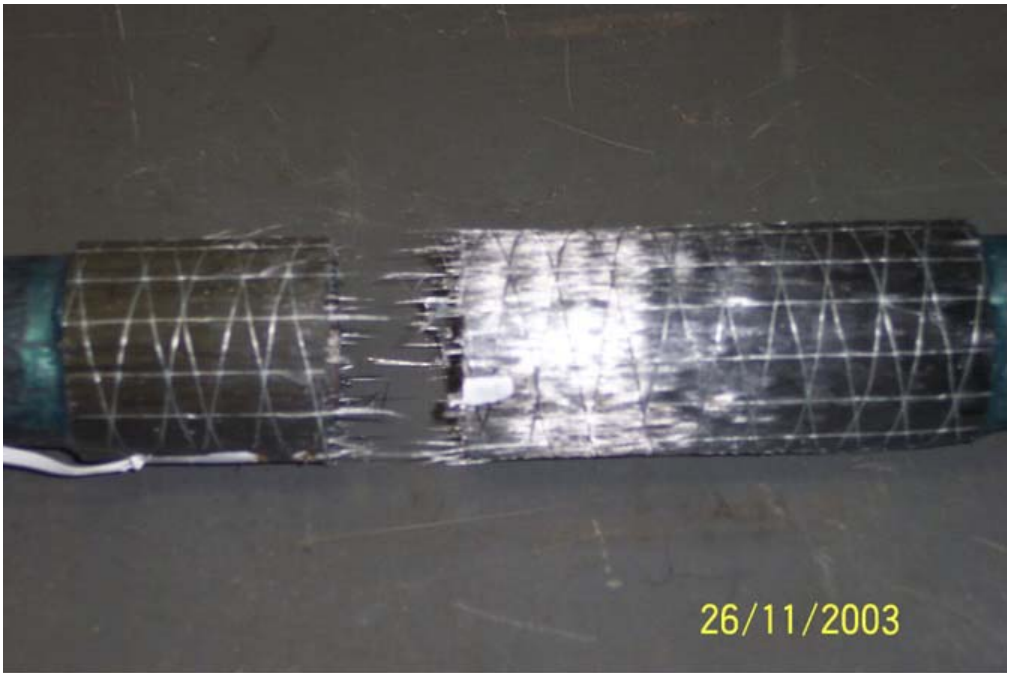

Figure 4. Failure Mode of the Test Specimen[1]

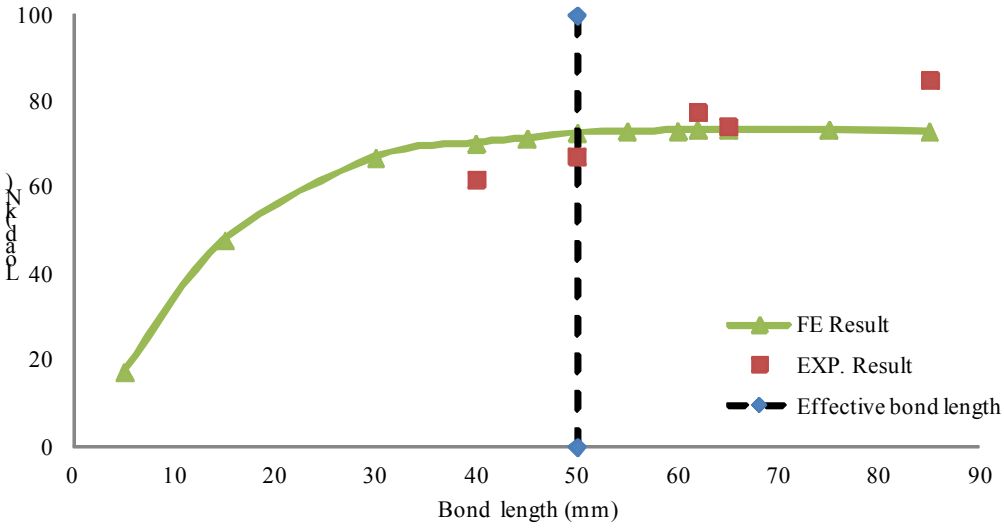

Figure 5. Comparison of Experimental [1] and FE Results

6. PARAMETRIC STUDY

VHS circular sections are used in situation where impact protection and extra strength is the critical requirement. It is also advisable that strength of VHS steel tube can be further increased by applying CFRP sheets. A parametric study has been conducted using finite element analysis. The main parameters studied are layers of CFRP, size of steel hollow sections and CFRP bond length.

6.1 Effect of Number of Layers of CFRP Sheets

Finite element analysis has been carried out for 38mm diameter steel hollow sections by varying CFRP layers from 3 layers to 5 in order to find out the variation of load carrying capacity with the increase in CFRP layers. Also it is intended to examine the changes in effective bond length by varying the CFRP number of layers. The ultimate loads from FE analysis for 3, 4 and 5 CFRP layers shown in Table 3. The objective of this analysis is to check the impact of reducing the number of CFRP layers for cost effectiveness. A comparison has been done for 3 to 4 layers and 3 to 5 layers. The values of COV are 0.054 and 0.094 for 4 layers/ 3 layers and 5layers / 3layers respectively. This comparison is showing that there are no significant changes in load carrying capacity with the increment of CFRP layers. Figure 6 presents the ultimate load under different bond lengths for 38mm diameter of 3 (38_3layers), 4 (38_4layers) and 5 (38_5layers) CFRP layer models. The load carrying capacity will contribute slightly higher by increasing the number of CFRP layers although it is not significant. From Figure 6 it can be determined that the effective bond length of 50mm [1] for high modulus CFRP strengthened VHS steel tube is not changed by the increase of number of CFRP layers. Therefore it can be concluded that three layers of CFRP are cost effective and most efficient.

Table 3. Comparison of Load Carrying Capacity of Different Layers of CFRP for 38mm Diameter Steel Tube

D mm	t (mm)	Bond Length (mm)	FE Model Results $P_{u,FE}$ kN			4 Layer/ 3 Layer	5 Layer/ 3Layer
			3 Layer	4 Layer	5 Layer		
38.0	1.84	85	55.96	64.52	73.06	1.153	1.306
38.0	1.84	75	55.79	64.46	73.39	1.155	1.315
38.0	1.84	65	56.47	64.30	73.53	1.139	1.302
38.0	1.84	55	56.42	65.85	73.05	1.167	1.295
38.0	1.84	50	56.36	65.68	72.73	1.165	1.290
38.0	1.84	45	56.21	65.43	71.42	1.164	1.271
38.0	1.84	30	54.68	60.93	67.01	1.114	1.225
38.0	1.84	15	46.25	47.30	47.78	1.023	1.033
38.0	1.84	5	17.26	17.27	17.27	1.001	1.001
Average						1.12	1.226
COV						0.054	0.094

6.2 Effect of Different Diameters of VHS Steel Circular Tube

Commercially available size of VHS circular sections are varies from 19mm to 100mm. Therefore FE model has been carried out by using four different diameters (38mm, 50mm, 75mm and 100mm) to check the effect of different sizes of CFRP strengthened VHS circular hollow section. Table 4 shows the list of ultimate load carrying capacity for 38mm, 50mm, 75mm and 100mm diameters VHS circular hollow sections. It can be concluded from the Table 4 that the load carrying capacity increases proportionally with the increase of diameter of VHS steel hollow sections. However, as can be seen in Figure 7 the effective bond length is not affected by the increase of diameter. The effective bond length remains 50mm for different sizes (38mm, 50mm, 75mm and 100mm) of CFRP strengthened VHS steel tube.

Table 4. Comparison of Load Carrying Capacity of Different Diameter of VHS Circular Steel Tube

Bond Length (mm)	Number of Layer	t (mm)	FE Model Results $P_{u,FE}$ kN			
			38mm	50mm	75mm	100mm
5	3	1.84	17.26	22.71	34.05	45.39
15	3	1.84	46.25	61.25	92.21	122.68
30	3	1.84	54.68	69.98	118.11	156.73
45	3	1.84	56.29	74.54	119.47	158.55
50	3	1.84	56.36	74.63	119.76	159.04
55	3	1.84	56.42	74.68	120.04	159.39
65	3	1.84	56.47	74.77	115.18	160.21
75	3	1.84	55.79	73.79	115.72	160.92
85	3	1.84	55.96	73.90	114.11	161.64

6.3 Effect of Different CFRP Bond Lengths

The main intention to generate different bond length models was to determine the effective bond length. Figure 6 presents the results of different CFRP layers on 38mm VHS steel tube sample and Figure 7 shows the results of different bond length models with 3 layers of CFRP. From the results presented in these figures it can be concluded that there are no changes of effective bond length for variation of size of steel tube and number of CFRP layers. It can also be seen that the ultimate load reaches a plateau after 50mm bond length in both figures. Therefore it can be concluded that effective bond length is 50mm for different sizes of the tube and different layers of CFRP.

7. LOAD CARRYING CAPACITY OF EACH LAYERS OF CFRP

Analytical model has been developed by Fawzia et al [1] by using the strain reading across the layers from experimental study. The load carried by each CFRP layers can be calculated as the product of the area of that layer (A_i) and the ultimate stress in that layer ($\sigma_{i,u}$). The total predicted load carrying capacity (P_p) can be written as:

$$P_p = \sum A_i \cdot \sigma_{i,u} = \sum A_i \cdot E \cdot \frac{\varepsilon_{1,u}}{\sqrt{i}} \quad (1)$$

Where $\sigma_{i,u} = E \cdot \varepsilon_{i,u} = E \cdot \frac{\varepsilon_{1,u}}{\sqrt{i}}$

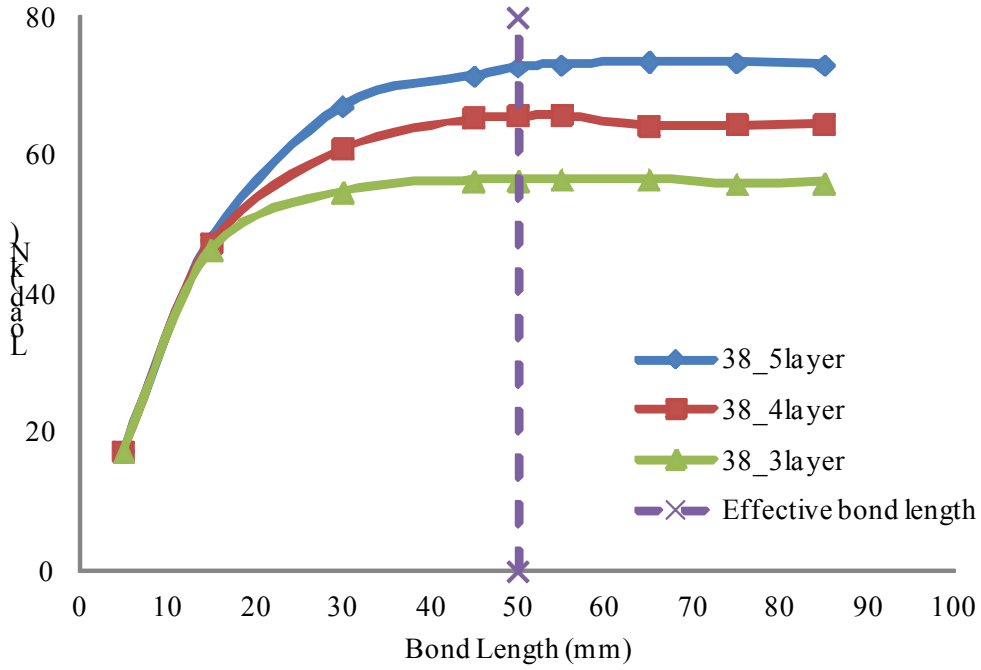

Figure 6. Effect of Number of CFRP Layers

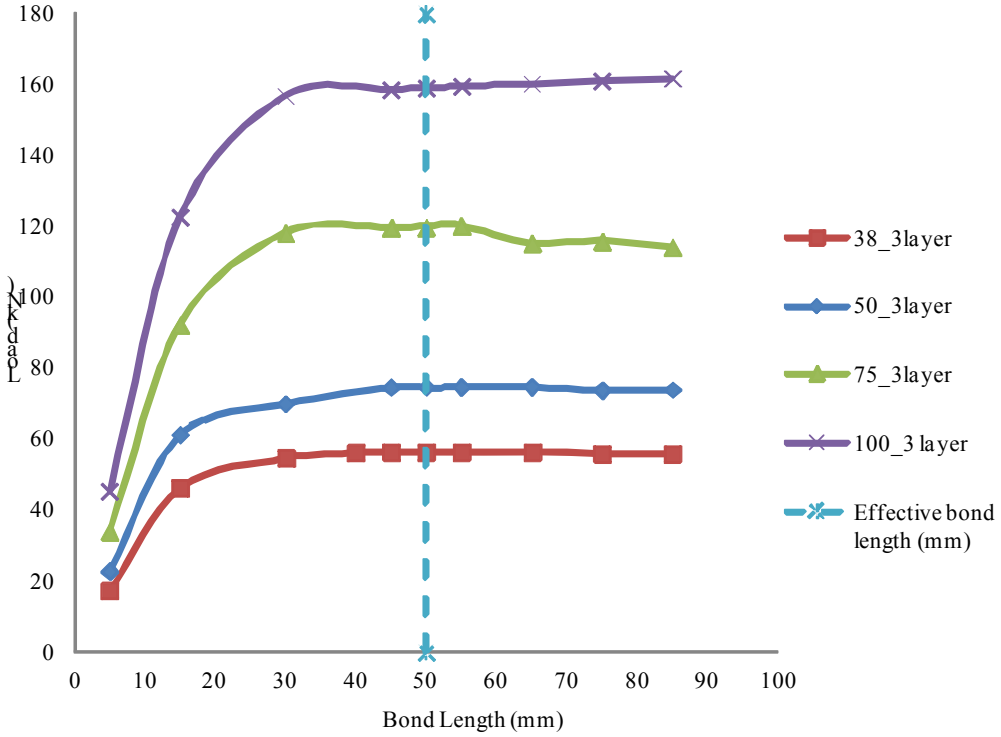

Figure 7. Effect of Different Size of Circular Steel Sections in FE Results

The value of $\varepsilon_{1,u}$ is taken as the maximum strain (2113 microstrain) obtained in tensile tests of CFRP with epoxy and the Young's modulus E is taken as 457,900 MPa [1]. The above analytical model has been used to calculate the ultimate load carrying capacity for each layer of CFRP. Table 5 and Figure 8 present the load carrying capacity of 1st, 2nd and 3rd layers of CFRP on 38, 50, 75 and 100 mm VHS circular steel tube. It can be seen that the first CFRP layer is carrying larger load than others. Once this layer carried the maximum capacity then the load is transferred to 2nd layer and so on. Finally the third layer is carrying very minimum load.

Table 5. Load Carrying Capacity of Different CFRP Layers of 38, 50,75 and 100 mm dia VHS Circular Steel Tube

Layer number	38mm dia	50mm dia	75mm dia	100mm dia
	Ultimate load (kN)	Ultimate load (kN)	Ultimate load (kN)	Ultimate load (kN)
1	22.92	30.12	45.13	60.14
2	16.37	21.46	32.07	42.68
3	13.50	17.66	26.32	34.98
Total	52.79	69.24	103.52	137.80

The first layer is carrying almost 43% of total load, 2nd layer is carrying 30% and 3rd layer is carrying only 25% load. From this finding it can be concluded that 3 layers of CFRP can be considered as the most efficient combination. Use of 4th and 5th layers of CFRP will only slightly increase the ultimate load which will be negligible compared to the 3 layers capacity. Table 6 shows the comparison of analytical model and FE Model for load carrying capacity of different diameters of CFRP strengthened VHS circular steel tube. The analytical model has reasonable agreement with the FE model as the COV of Table 6 is 0.04. It can be concluded that the analytical model to predict the load carrying capacity by using the ultimate strain of each layers of CFRP is applicable to 38mm to 100mm range of CFRP strengthened VHS steel tubes.

Table 6. Comparison of Analytical Model and FE Model for Load Carrying Capacity of Different Diameter of VHS Circular Steel Tube

Diameter	Analytical Ultimate load	FE Ultimate load	FE/Analytical
mm	kN	kN	
38	52.79	56.36	1.07
50	69.24	74.63	1.08
75	103.52	119.76	1.16
100	137.80	159.04	1.15
mean			1.11
COV			0.04

8. DISTRIBUTION OF LONGITUDINAL STRESS

Figure 9 shows the distribution of longitudinal stress at the joint for CFRP strengthened 38mm, 50mm, 75mm and 100mm diameter VHS steel hollow sections. In this figure, longitudinal stress of the first or bottom CFRP layer is shown as the bottom layer of CFRP is carrying the highest load. The horizontal axis of Figure 9 is a factor which has been applied to the FE model to represent the applied load. It can be seen that the longitudinal stress is increasing with the increase of the factor,

which means that longitudinal stress increases with the increase of the load. From Figure 9 it can be seen that longitudinal stress is increasing with the increase of the size of steel tube. Therefore it can be concluded that increasing the size of steel tube will increase the longitudinal stress at the joint of double strap joint.

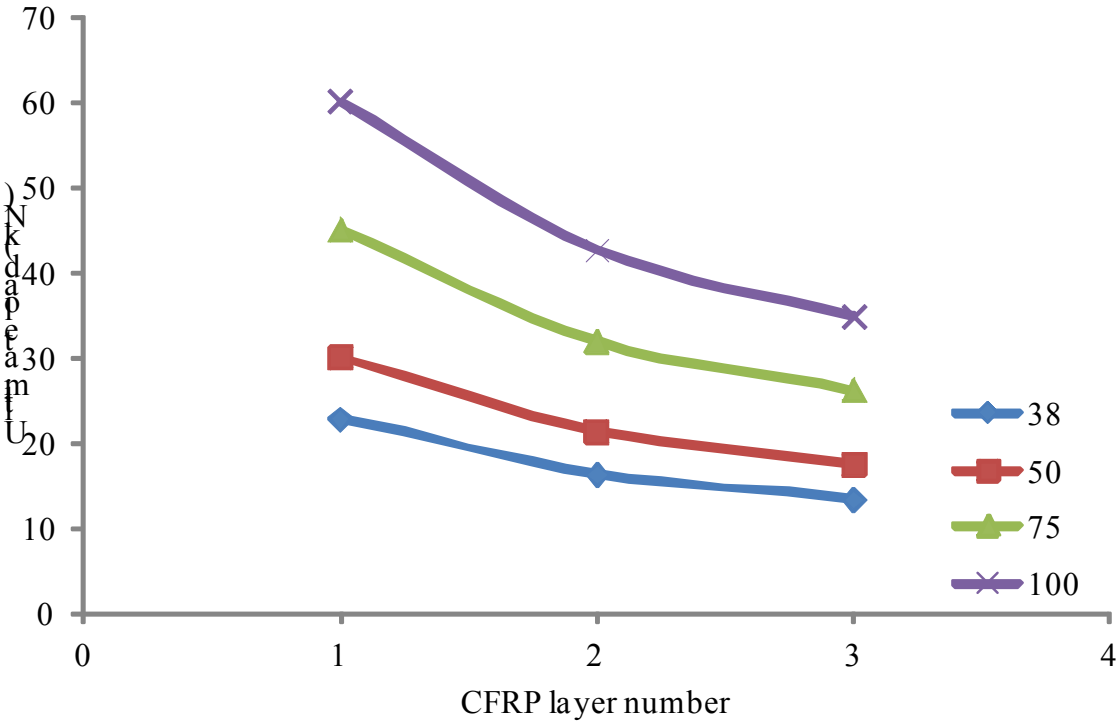

Figure 8. Comparison of Load Carrying Capacity of Different Layers of CFRP for 38, 50, 75 and 100 mm dia CFRP Strengthened VHS Steel Tube

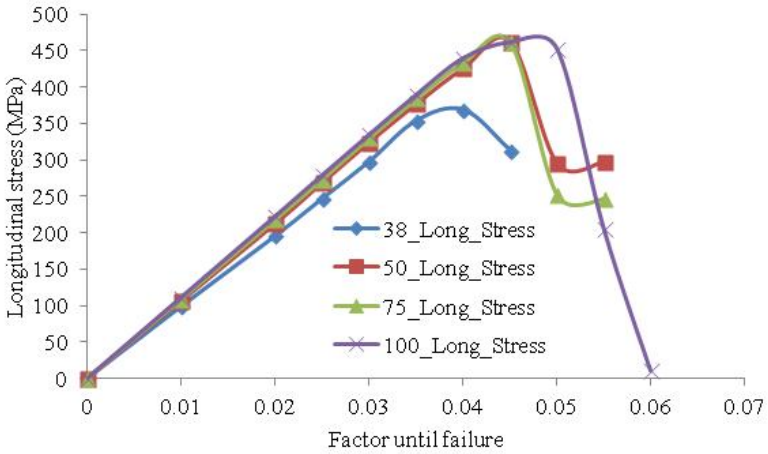

Figure 9. Distribution of Longitudinal Stress for Different Diameter CFRP Strengthened VHS Steel Hollow Section

9. DISTRIBUTION OF HOOP STRESS

Figure 10 shows the distribution of hoop stress for 38mm, 50mm, 75mm and 100mm diameter VHS steel hollow section double strap joints. Determination of the distribution of hoop stress is really important for circular hollow section. Figure 10 is representing the hoop stress distribution at the first or bottom CFRP layer at the joint of double strap joint. The horizontal axis of Figure 10 is a factor which has been applied to the FE model to represent the applied load. It can be seen that the hoop stress is increasing with the increase of the factor, which means that hoop stress is increasing with the increase of the applied load. It can be seen that the maximum hoop stress at the joint for 38mm, 50mm, 75mm and 100mm diameter samples are 50, 85, 97 and 113MPa respectively. Therefore it can be concluded from Figure 10 that increasing the size of steel tube will increase the hoop stress capacity of CFRP strengthened steel hollow tube.

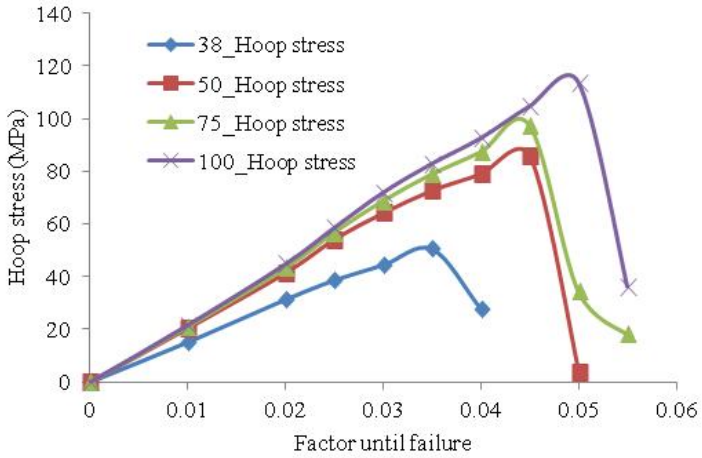

Figure 10. Distribution of Hoop Stress for Different Diameter CFRP Strengthened VHS Steel Hollow Section

10. SUMMARY

In this paper the results from finite element analysis of CFRP strengthened VHS steel tube double strap joint specimens under tension are presented. The investigated variables are CFRP bond lengths, number of CFRP layer, and size of circular steel hollow sections. The findings from the parametric studies are summarised as follows:

1. Load carrying capacity does not change significantly with the increment of bond length after 50mm for CFRP strengthened VHS steel tube double strap joint. Therefore it can be concluded that the effective bond length is 50mm for CFRP strengthened VHS steel tubes.
2. There was no change in effective bond length for variation of CFRP layers. Load carrying capacity increased with the increase in number of CFRP layers but the improvement was not significant. Therefore it can be concluded that three layers of CFRP is the most effective for CFRP strengthened VHS steel tubes. Effective bond length of CFRP strengthened VHS steel tubes is 50mm for different number of CFRP layers (3 to 5 layers).
3. There was no change in effective bond length for different diameters of CFRP strengthened VHS steel hollow sections. Load carrying capacity increased by increasing the size of steel hollow section but the change was not significant. Effective bond length of CFRP strengthened VHS steel specimens is 50mm for different sizes (38mm to 100mm) of CFRP strengthened VHS steel tubes.
4. Three layers of CFRP do not carry same load for a given CFRP arrangement. The first or bottom layer of CFRP carry about 43% load, 2nd layer carry 30% and 3rd layer carry 25% load for the double strap joint investigated in this research.

5. Three layers of CFRP are cost effective and most efficient layers for CFRP strengthened VHS steel hollow tube.
6. Increasing the size of steel tube will increase the longitudinal stress and hoop stress at the joint of steel hollow section double strap joint.

NOTATION

A_i = Product of the area of the layer
E = Young's modulus of CFRP
L1 = Short bond length (mm)
L2 = Long bond length (mm)
$P_{u,EXP}$ = Ultimate load of experiment
$P_{u,FE}$ = Ultimate load of FE model
P_p =The total predicted load carrying capacity
$\sigma_{i,u}$ =The ultimate stress in the ith layer
$\varepsilon_{i,u}$ =The ultimate strain in the i^{th} layer
$\varepsilon_{1,u}$ =The ultimate strain in the first (bottom) layer
ε_i = Strain in the i^{th} layer
I = Layer number

REFERENCES

[1] Fawzia, S., Al-Mahaidi, R., Zhao, X.L., and Rizkalla, S., "Strengthening of Circular Hollow Steel Tubular Sections using High Modulus CFRP Sheets", Construction and Building Materials, 2007, Vol. 21, No. 4, pp. 839-845.
[2] Teng, J.G., T.B. Yu and Fernando, D., "Strengthening of Steel Structures with Fiber-reinforced Polymer Composites", Journal of Constructional Steel Research, 2012, Vol. 78, pp.131–143.
[3] Fawzia, S. "Evaluation of Shear Stress and Slip Relationship of Composite Lap Joints", Composite Structures, 2013, 100, pp.548-553.
[4] Fawzia, S., Zhao, X.L. and Al-Mahaidi, R., "Bond–slip Models for Double Strap Joints Strengthened by CFRP", Composite Structures, 2010, Vol. 92, No. 9, pp. 2137-2145.
[5] Fawzia, S., Al-Mahaidi, R. and Zhao, X.L., "Experimental and Finite Element Analysis of a Double Strap Joint between Steel Plates and Normal Modulus CFRP", Composite Structures, 2006, Vol. 75, No. 1-4, pp. 156-162.
[6] Fawzia, S., Zhao, X.L., Al-Mahaidi, R. and Rizkalla, S., "Bond Characteristics between CFRP and Steel Plates in Double Strap Joints", Advanced Steel Construction-An International Journal, 2005, Vol. 1, No. 2, pp. 17–28.
[7] Zhao, X.-L., "Section Capacity of Very High Strength (VHS) Circular Tubes under Compression", Thin-Walled Structures 2000, Vol. 37, No. 3, pp. 223-240.
[8] BASF Construction Chemicals Australia Pty Ltd., "Mbrace Fibre CF 530, Technical Data Sheet", 7 Kingston Town Close, Oakleigh, Australia.
[9] Jiao, H. and Zhao, X.L., "Material Ductility of Very High Strength (VHS) Circular Steel Tubes in Tension", Thin-Walled Structures, 2001, Vol. 39, No. 11, pp. 887–906.

NUMERICAL ANALYSIS OF FATIGUE BEHAVIOR OF WELDED CFCHS T-JOINTS

Min Gu[1], Le-Wei Tong[2,*], Xiao-Ling Zhao[3] and Yun-Feng Zhang[4]

[1, 2] State key laboratory for Disaster Reduction in Civil Engineering, Tongji University and College of Civil Engineering, Tongji University, Shanghai 200092, China
[3] Department of Civil Engineering, Monash University, Clayton, VIC 3800, Australia
[4] Department of Civil & Environmental Engineering, University of Maryland, College Park, MD 20742, USA and Guang-Hua Education Foundation Scholar, College of Civil Engineering, Tongji University, Shanghai 200092, China
**(Corresponding author: E-mail: tonglw@tongji.edu.cn)*

Received: 21 February 2014; Revised: 29 April 2014; Accepted: 2 May 2014

ABSTRACT: Fatigue life assessment of welded joints made of circular hollow sections (CHS) with concrete filled (CF) chord member subject to vehicle load is vital in designing of CFCHS arch truss bridge. A key issue in fatigue life assessment of such joints is how to accurately estimate the stress intensity factor. This paper describes a methodology for calculating the stress intensity factor of the hot spot region in the welded CFCHS T-joints based on a finite element analysis which considers weld modeling, crack modeling and nonlinear interface element between steel and concrete. A procedure for fatigue life estimation of welded CFCHS T-joints is also established. Discussions are made on the effect of the initial crack size and concrete strength on fatigue life and hot spot stresses. The majority of crack propagation life is found to be associated with the shallow crack stage. The proposed method gives reasonable estimation of fatigue life of welded CFCHS T-joints.

Keywords: Concrete-filled circular hollow section, Welded joints, Fatigue life prediction, Fracture mechanics, Finite element analysis

1. INTRODUCTION

Concrete-filled steel tubes have been widely used in civil engineering structures [1, 2]. Recently in China, concrete-filled circular hollow sections (CFCHS) have been increasingly used in large-span arch truss bridges. One example is the Wuxia Bridge located in Chongqing City, China, which has a 460 m main span. In the CFCHS arch truss bridges, circular hollow section (CHS) chord members and the brace members are welded together and the main chords are filled with concrete while the braces are unfilled. The motivation for using such CFCHS structures comes from the fact that the concrete infill can substantially improve the stability of the compressive chords as well as the stiffness near the intersection of the chords and braces. However, it is well known that cyclic loads may cause fatigue failure at the weld toe of the CHS joints due to high stress concentration and welding defects. The welded CFCHS joints in these arch truss bridges are therefore susceptible to fatigue cracking since they are subject to cyclic loads induced by daily traffic. Fatigue is an important issue in designing welded CFCHS joints.

Extensive research has been conducted on fatigue of welded tubular joints without infill of concrete (e.g. [3-7]). The hot spot stress method has been widely adopted in designing such welded tubular joints [3], where SCF (stress concentration factor) formulae and S-N (hot spot stress range - fatigue strength) curves are required. The existing design rules for unfilled tubular joints cannot be applied to welded CFCHS joints because different SCF values and S-N curves are expected. There are

some research on CFCHS and CFSHS (concrete filled square hollow section) joints, e.g. CFCHS K-joints [8, 9], CFSHS T-joints [10, 11] and CFCHS T-joints [12]. However there are not yet enough experimental data to establish reliable SCF formulae and S-N curves for concrete filled tubular joints.

This paper presents a fracture mechanics approach to assess the fatigue life of CFCHS T-joints, which involves the determination of initial crack location and size, stress intensity factor and proper crack growth model. The stress intensity factor is a function of the applied stress field, crack length and geometry [13, 14]. A brief summary of the experimental work is given in terms of hot spot stresses and fatigue life of welded CFCHS T-joints under axial tensile force in the brace. Some assumptions about the crack are made in order to carry out fatigue life assessment using fracture mechanics. To determine the stress intensity factor in such fatigue details, a procedure involving parameter transformation method, geometrical modeling and mesh generation procedures for the welded CFCHS T-joint with surface crack, and displacement extrapolation are presented. The crack propagation behavior from numerical analysis is discussed in this paper. The predicted fatigue life of welded CFCHS T-joints agrees well with that obtained from experimental testing.

2. BRIEF SUMMARY OF FATIGUE TESTS ON WELDED CFCHS T-JOINTS

The dimensions and geometry of welded CFCHS T-joint specimens are shown in Figure 1 and Table 1. A total of ten specimens were tested, which had varying geometry and concrete grades in order to study their effect on the joint behavior. The steel material used for both the chord and brace in the joint was steel Q345. The brace was connected to the chord through manual arc welding with full penetration weld in accordance with AWS 2000 [15]. The chord was filled with concrete, while the brace was unfilled.

Static tests in the elastic range were first conducted on the welded CFCHS T-joints at Tongji University to obtain hot spot stress and to consequently derive stress concentration factor SCF (defined as the ratio of hot spot stress and the nominal stress in the brace) of these welded joint specimens. For the static tests, the brace was subjected to axial tensile force F while the main chord was simply supported (see Figure 1). The experimental results indicated that for each specimen the maximum SCF_{max} listed in Table 2 occurred at the chord crown position.

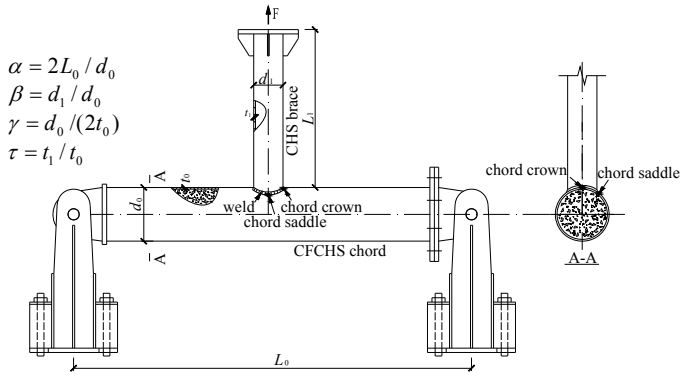

Figure 1. Welded CFCHS T-joint Specimen and Static Test Setup

Table 1. Details of Test Specimens

Joint	$d_0 \times t_0$ (mm×mm)	$d_1 \times t_1$ (mm×mm)	Nondimensional geometrical parameter			Steel Grade	Concrete Grade
			$\beta=d_1/d_0$	$2\gamma=d_0/t_0$	$\tau=t_1/t_0$		
CFCHS-1	245×8	133×8	0.54	30.62	1.00	Q345	C50
CFCHS-2	180×6	133×6	0.74	30.00	1.00	Q345	C50
CFCHS-3	133×4.5	133×4.5	1.00	29.56	1.00	Q345	C50
CFCHS-4	245×8	133×6	0.54	30.62	0.75	Q345	C50
CFCHS-5	245×8	133×4.5	0.54	30.62	0.56	Q345	C50
CFCHS-6	245×8	133×8	0.54	30.62	1.00	Q345	C20
CFCHS-7	245×8	133×8	0.54	30.62	1.00	Q345	C70
CFCHS-8	203×8	140×8	0.69	25.38	1.00	Q345	C50
CFCHS-9	203×10	140×10	0.69	20.30	1.00	Q345	C50
CFCHS-10	203×12	140×12	0.69	16.92	1.00	Q345	C50

Note : Both the yield strength and the impact toughness at 20□ of Steel Q345 are 345 MPa and over 34 Joules respectively. The cubic compressive strength of Concrete C20, C50 and C70 is 20, 50 and 70 MPa respectively.

Table 2. Experimental SCF and Fatigue Life of Test Specimens

Joint	Maximum SCF	Axial force range F_r (kN)	Fatigue life N
CFCHS-1	6.79	80	1133000
CFCHS-2	8.86	60	410994
CFCHS-3	12.50	60	20295
CFCHS-4	3.98	100	844800
CFCHS-5	4.08	80	737706
CFCHS-6	7.42	90	394800
CFCHS-7	6.54	80	1351350
CFCHS-8	7.98	80	881280
CFCHS-9	8.77	110	599720
CFCHS-10	8.65	65	4013272

Constant-amplitude fatigue loading tests were conducted after the static elastic tests of these welded CFCHS T-joints. The brace of each T-joint was subjected to an axial cyclic force with a frequency of 4 Hz. The stress ratio, defined as the ratio of the minimum force to maximum force, was from 0.23 to 0.35. Seeing that the actuator of the fatigue testing machine could only push out, the brace was reversed and a loading frame between the actuator and the brace end was installed so that a "push" from the fatigue testing machine was transformed into a "pull" to the brace, as shown in Figure 2. The applied axial force range F_r for each joint is given in Table 2.

A typical damage pattern with fatigue crack initiating at the weld toe of chord crown for the welded CFCHS T-joints is shown in Figure 3. The fatigue test results showed that fatigue crack usually initiated at or near the chord crown location which was exactly the position of maximum hot spot stress (i.e. the position of maximum stress concentration factor) indicated by static tests. The crack propagated along the weld toe intersecting the chord and brace and finally along the chord circumference. The fatigue life N of each CFCHS T-joint obtained from the fatigue tests is listed in

Table 2, which will be used to check the fatigue life predicted using numerical analysis based on the theory of fracture mechanics. In this paper N is defined as the number of load cycle when the fatigue induced crack fully penetrates the wall thickness of the steel tubular chord, which is a commonly accepted fatigue failure criterion [3]. The details of the fatigue test results have been reported in the reference [12].

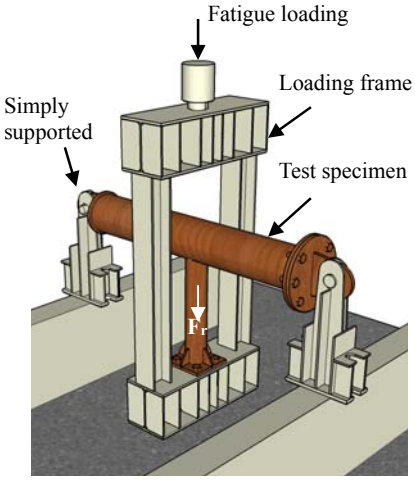

Figure 2. Fatigue Test Setup

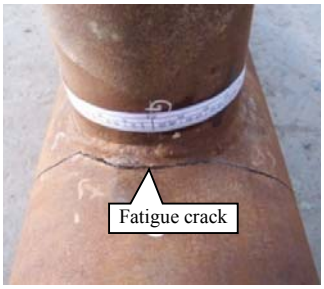

Figure 3. Typical Fatigue Crack

3. NUMERICAL SIMULATION STUDY

This section presents the numerical analysis procedure for the welded CFCHS T-joints, which includes assumptions for fatigue crack location and shape, as well as features of finite element model. This numerical analysis model will be used later for calculating the stress intensity factors of CFCHS T-joints.

3.1 Assumptions for Fatigue Crack Location and Shape

In order to facilitate numerical analysis, assumptions was made about the initial crack location, size and crack shape of the welded CFCHS T-joint based on the experimental data of hot spot stress, fatigue strength and observed fatigue behavior.

3.1.1 Initial crack location and size

The surface crack is assumed to initiate at the chord crown position which has the maximum stress concentration factor. This is also verified through extensive finite element based parametric study of the CFCHS T-joints' chord subject to cyclic load transmitted from axially loaded brace. It is assumed that the deepest point of the semi-elliptical fatigue crack is located at the two crowns of the chord, as shown in Figure 4.

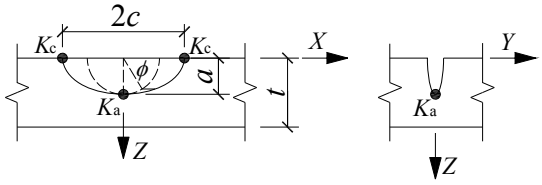

Figure 4. Schematics of Semi-elliptical Surface Crack Model

In the HSE document [16], slag intrusions are specified to range from 0.15 to 0.4 mm in depth and typical sizes at the weld toe are set as $a_i = c_i = 0.25$mm. In this study, the initial crack sizes are also assumed as $a_i = c_i = 0.25$mm for the semi-elliptical crack shape.

3.1.2 Crack shape

Based on the knowledge of linear elastic fracture mechanics and observed typical damage pattern for the welded CFCHS T-joints (e.g., Figure 3), the surface crack is assumed to exhibit a semi-elliptical shape with a depth of a and length of $2c$ around the weld toe. When unwrapped and projected into a plane, the elliptical equation of $(x/c)^2 + (z/a)^2 = 1$ can be used to describe the crack shape, as shown in Figure 4. The crack growth in the thickness direction is assumed to be perpendicular to the surface of the chord because it requires the least amount of energy for crack propagation. In this study two stress intensity factors K_a and K_c (associated with the deepest point and the crack ends respectively) are calculated because they govern the crack growth.

3.2 Finite Element Analysis

The major challenges encountered in the process of establishing the numerical model for the welded CFCHS T-joints with surface crack defect at the chord crown positions include: weld modeling, crack modeling, nonlinear interface element between steel tube and concrete infill. To accomplish this using the general computational software ANSYS [17], the APDL (ANSYS Parametric Design Language) was employed in this study to implement a geometric transformation scheme as well as constructing a new crack-tip singular element. Through geometric transformation, the complex problem of modeling welded CFCHS T-joints with surface crack defect is converted into a relatively simple model of welded T-butt plate with surface crack at weld toe.

3.2.1 Modeling procedure

In this study, the mesh of the welded T-butt plate with surface crack at weld toe was generated using the APDL code for a good balance between refined mesh near the crack tip, good transition and compatibility of the mesh and computing time. A depiction of the finite element modeling procedure is given in Figure 5, and details of each step in this procedure are described as follows,

(a) T-butt with surface crack (b) Quarter of CHS brace (c) CHS brace with the unfolded surface of a quarter of chord

(d) Quarter CHS joint (e) Quarter CHS joint with concrete infill in chord

Figure 5. Illustration of Finite Element Modelling Procedure

STEP 1: The first step in the modeling process is to build a welded T-butt plate with a semi-elliptical crack defined by two dimensionless parameters, a/t_0 and a/c where t_0 is the chord wall thickness. Crack tip singular elements are included. This plate is only for a quarter of the brace member in the T-joint.
STEP 2: The T-butt plate is then built into a quarter of the round brace tube because of the symmetry of the T-joint and applied load.
STEP 3: A flat plate model for the chord is generated and then connected to the quarter brace model from STEP 2 by merging the common nodes of both the chord plate and the brace.
STEP 4: The chord plate model is built into the half hollow circular tube with the parameters α, β, γ, τ, t_0 of the joint defined.
STEP 5: Concrete elements are added to the chord member. Caution is exercised here to match the interface mesh of the concrete and steel chord for which contact elements are used at the interface of these two materials.

3.2.2 Geometric transformation

Geometric transformation is employed here to map nodes on a flat plane to circular surface while maintaining their topological relationships for the same elements. Geometric transformation formulas have been derived and implemented into the ANSYS model using the APDL commands in this study. Crack tip singular element has been developed which is previously not available in the ANSYS element library. In order to simulate the crack propagation path, both the crack and joint sizes have been chosen as the varying parameters. Additionally, nonlinear contact elements between the steel chord member and the concrete infill are also employed.

For high-quality mesh generation, the unfolded surface of a quarter of chord was divided into four regions as shown in Figure 6. In Region I and II, a series of concentric circles with different radius (r_i) have been drawn, where $r_i = 0.5d_1\text{-}t_1$ represents the brace inner wall projection, $r_i = 0.5d_1 + h_{f1}$ represents the chord weld toe projection, and $r_i = 0.5d_1 + h_{f1} + Tr$ represents the border line where different transformation formulas will be used for the inner nodes and outer nodes on its two sides. h_{f1} is the weld toe height on the chord side. h_{f2} is the weld toe height on the brace side. The mesh for both Region I and II needs to be symmetrical.

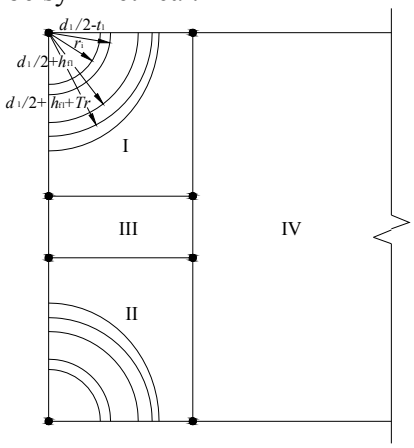

Figure 6. Four Regions for Finite Element Mesh on the Unfolded Surface of a Quarter of Chord

It is noteworthy that the nodes on the interior surface of the steel tube and the nodes on the external surface of the concrete coincide with each other while they cannot be merged together. Otherwise, it may lead to non-convergence or erroneous results in the finite element simulation based on the ANSYS model due to the initial gap or penetration between the two contact materials. The following formulas are derived to make the geometric transformation easier.

3.2.2.1 Geometric transformation for chord

An unfolded plane surface mesh of a quarter of chord at T-joint in Figure 7 is transformed into its curved surface mesh using Eqs. 1, 2 and 3.

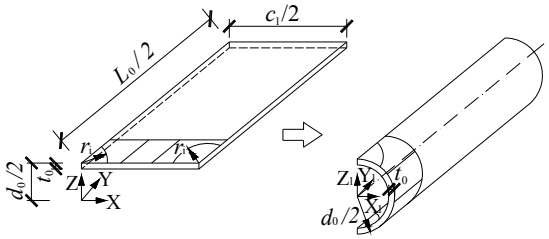

Figure 7. Geometric Transformation for Chord Mesh

For $X \le d_1/2+h_{f1}+Tr$ and $r \le d_1/2+h_{f1}+Tr$ (see Figure 7),

$$\begin{cases} X_1 = Z\sin[\dfrac{d_0 \arcsin\dfrac{2X}{d_0} - \dfrac{(d_0/2-Z)(c_1-c_2)d_0}{t_0c_1}\arcsin\dfrac{2X}{d_0}}{2Z}] \\ Y_1 = Y \\ Z_1 = Z\cos[\dfrac{d_0 \arcsin\dfrac{2X}{d_0} - \dfrac{(d_0/2-Z)(c_1-c_2)d_0}{t_0c_1}\arcsin\dfrac{2X}{d_0})}{2Z}] \end{cases} \tag{1}$$

Where c_1 is the outer circumference of a chord, and c_2 is the inner circumference of a chord.
For $X \ge c_1/2-(d_1/2+h_{f1}+Tr)$ and $r \le d_1/2+h_{f1}+Tr$,

$$\begin{cases} X_1 = Z\sin[\dfrac{(c_1-d_0\arcsin\dfrac{c_1-2X}{d_0}) - \dfrac{(d_0/2-Z)(c_1-c_2)}{t_0c_1}(c_1-d_0\arcsin\dfrac{c_1-2X}{d_0})}{2Z}] \\ Y_1 = Y \\ Z_1 = Z\cos[\dfrac{(c_1-d_0\arcsin\dfrac{c_1-2X}{d_0}) - \dfrac{(d_0/2-Z)(c_1-c_2)}{t_0c_1}(c_1-d_0\arcsin\dfrac{c_1-2X}{d_0})}{2Z}] \end{cases} \tag{2}$$

For others,

$$\begin{cases} X_1 = Z\sin[\dfrac{X - \dfrac{(d_0/2-Z)(c_1-c_2)}{t_0c_1}X}{Z}] \\ Y_1 = Y \\ Z_1 = Z\cos[\dfrac{X - \dfrac{(d_0/2-Z)(c_1-c_2)}{t_0c_1}X}{Z}] \end{cases} \tag{3}$$

3.2.2.2 Geometric transformation for brace

A plate mesh with weld in Figure 8 is transformed into the brace mesh using Eqs. 4 and 5.

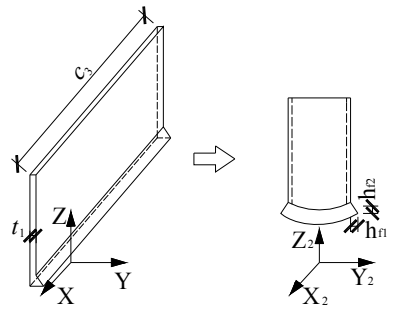

Figure 8. Geometric Transformation for Brace Mesh

For $Z \in [d_0/2, d_0/2 + h_{f2}]$,

$$\begin{cases} X_2 = Y \sin[\dfrac{X - \dfrac{(d_1/2 + h_{f1} - Y)(c_5 - c_4)}{(t_1 + h_{f1})c_5} X}{Y}] \\ Y_2 = Y \cos[\dfrac{X - \dfrac{(d_1/2 + h_{f1} - Y)(c_5 - c_4)}{(t_1 + h_{f1})c_5} X}{Y}] \\ Z_2 = Z - [d_0/2 - \sqrt{(d_0/2)^2 - X^2}] \end{cases} \tag{4}$$

Where c_4 is the inner circumference of a brace, and c_5 is the projection length in plane of a weld toe on the chord side.

For $Z \in [d_0/2 + h_{f2}, d_0/2 + L_1]$,

$$\begin{cases} X_2 = Y \sin[\dfrac{X - \dfrac{(d_1/2 + h_{f1} - Y)(c_5 - c_4)}{(t_1 + h_{f1})c_5} X}{Y}] \\ Y_2 = Y \cos[\dfrac{X - \dfrac{(d_1/2 + h_{f1} - Y)(c_5 - c_4)}{(t_1 + h_{f1})c_5} X}{Y}] \\ Z_2 = Z - \dfrac{d_0/2 + L_1 - Z}{L_1 - h_{f2}} [d_0/2 - \sqrt{(d_0/2)^2 - X^2}] \end{cases} \tag{5}$$

3.2.2.3 Geometric transformation for concrete

In order to make the nodes on the interior surface of the steel tube be the same with the nodes on the external surface, concrete mesh in Figure 9 is transformed using Eqs. 6, 7 and 8.

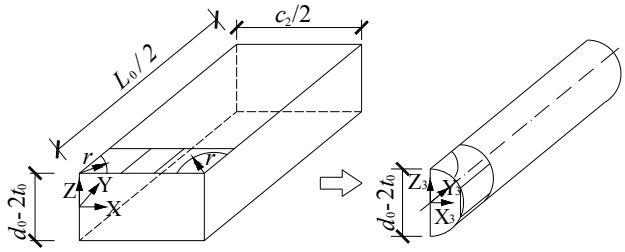

Figure 9. Geometric Transformation for Concrete Mesh

For $X \le d_1/2 + h_{f1} + Tr$ and $r \le d_1/2 + h_{f1} + Tr$,

$$\begin{cases} X_3 = (d_0/2 - t_0)\sin[\dfrac{c_2 d_0 \arcsin\dfrac{2X}{d_0}}{c_1(d_0 - 2t_0)}] \\ Y_3 = Y \\ Z_3 = \dfrac{Z\sqrt{(d_0/2 - t_0)^2 - X_3^{\,2}}}{d_0/2 - t_0} \end{cases} \tag{6}$$

For $X \ge c_1/2 - (d_1/2 + h_{f1} + Tr)$ and $r \le d_1/2 + h_{f1} + Tr$,

$$\begin{cases} X_3 = (d_0/2 - t_0)\sin[\dfrac{c_2(c_1 - d_0 arc\sin\dfrac{c_1 - 2X}{d_0})}{c_1(d_0 - 2t_0)}] \\ Y_3 = Y \\ Z_3 = \dfrac{Z\sqrt{(d_0/2 - t_0)^2 - X_3^{\,2}}}{d_0/2 - t_0} \end{cases} \tag{7}$$

For others,

$$\begin{cases} X_3 = (d_0/2 - t_0)\sin[\dfrac{2c_2 X}{c_1(d_0 - 2t_0)}] \\ Y_3 = Y \\ Z_3 = \dfrac{Z\sqrt{(d_0/2 - t_0)^2 - X_3^{\,2}}}{d_0/2 - t_0} \end{cases} \tag{8}$$

3.2.3 Material property and element type

In the finite element analysis, most part of the steel tube is simulated using the SOLID45 element in the ANSYS software except for the crack tip singular element. The modulus of elasticity and Poisson's ratio are set 206 GPa and 0.3 [12], respectively.

Particular attention was given to understand the behavior of the concrete inside the chord under fatigue load as this is important to the fatigue failure mode and thus fatigue strength. After each fatigue test was completed, steel tube near the intersection of the brace and the chord was cut to expose the concrete for a close examination. As shown in Figure 10 for a typical specimen, no

visual sign of concrete crushing was seen in any specimen. It is found from subsequent finite element analysis that the concrete infill changes the hot spot stress distribution at the intersection of a CHS brace and a CHS chord and thus affects the fatigue strength of a welded joint. However, when concrete strength grade changes, the hot spot stresses remain almost the same. Although the effect of concrete strength grade is insignificant, the fatigue property of the concrete itself cannot be neglected. The fatigue deformation modulus for concrete can be found in the Chinese *Code for the Design of Concrete Structures* (GB 50010-2010). They are summarized in Table 3. The Poisson's ratio of concrete is taken as 0.2. In the ANSYS finite element model, concrete is simulated using the SOLID65 element.

(a) Concrete extreme fiber in tension (b) Concrete extreme fiber in compression

Figure 10. View of Concrete Infill Damages

Table 3. Concrete Fatigue Deformation Modulus E_c^f

Concrete grade	C20	C30	C40	C50	C60	C70	C80
E_c^f (MPa)	11000	13000	15000	16000	17000	18000	19000

The weld is modeled using SOLID45 element in the ANSYS with its geometry configuration defined according to the AWS (2000) recommendations and its material properties were assumed to be the same as the parent steel metal.

The contact elements (TARGE 170 and CONTA 174 in the ANSYS software) at the interface of concrete infill and steel chord tube were employed to simulate the contact mechanism between the steel and concrete. The friction coefficient for the interface was set as 0.4.

The crack tip singular element (see Figure 11) is based on Basroum's research [18] where the middle nodes in the wedge-shaped elements are moved to the quarter points of the element side in order to model the $1/\sqrt{r}$ singularity. Since this type of element is unavailable in ANSYS, the wedge-shaped singular element was constructed from the SOLID95 element using the APDL programming language.

Figure 11. Crack Tip Singular Element

In order to accurately simulate the bending stresses and stress concentrations in the intersection region, more than four layers of finite elements were used along the chord wall thickness direction and three layers along the brace wall thickness direction, which poses a challenge for the transition between the fine mesh near the intersection and the outer coarse mesh. The crack tip is surrounded

by four rings of elements and each ring contains eight elements. Figure 12 shows a close up of the finite element mesh at the chord crown position.

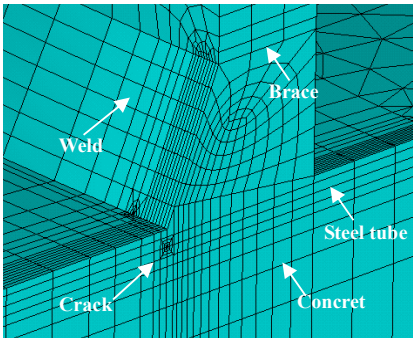

Figure 12. Close-up View of Finite Element Mesh near the T-joint Crown position

4. STRESS INTENSITY FACTOR CALCULATION

4.1 General Methodology

From the knowledge of linear elastic fracture mechanics, displacements near the crack tip and stress intensity factors can be expressed as follows.

$$\begin{cases} u = \dfrac{K_{\mathrm{I}}}{4\mathrm{G}}\sqrt{\dfrac{r}{2\pi}}[(2\mathrm{k}-1)\cos\dfrac{\theta}{2}-\cos\dfrac{3\theta}{2}]- \\ \quad -\dfrac{K_{\mathrm{II}}}{4\mathrm{G}}\sqrt{\dfrac{r}{2\pi}}[(2\mathrm{k}+3)\sin\dfrac{\theta}{2}+\sin\dfrac{3\theta}{2}]+\mathrm{o}(r) \\ v = \dfrac{K_{\mathrm{I}}}{4\mathrm{G}}\sqrt{\dfrac{r}{2\pi}}[(2\mathrm{k}+1)\sin\dfrac{\theta}{2}-\sin\dfrac{3\theta}{2}]- \\ \quad -\dfrac{K_{\mathrm{II}}}{4\mathrm{G}}\sqrt{\dfrac{r}{2\pi}}[(2\mathrm{k}+3)\cos\dfrac{\theta}{2}+\cos\dfrac{3\theta}{2}]+\mathrm{o}(r) \\ w = \dfrac{2K_{\mathrm{III}}}{\mathrm{G}}\sqrt{\dfrac{r}{2\pi}}\sin\dfrac{\theta}{2}+\mathrm{o}(r) \end{cases} \tag{9}$$

where

$$\mathrm{k} = \begin{cases} 3-4\nu & \texttt{plane strain} \\ \dfrac{3\nu}{1+\nu} & \texttt{plane stress} \end{cases}$$

In Eq. 9, u, v, w denotes the local radial, normal and tangential displacement (see Figure 13). K_{I}, K_{II}, K_{III} are the mode I, II, III stress intensity factors respectively. G is the shear modulus and ν denotes the Poisson's ratio.

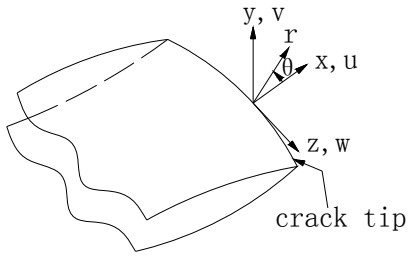

Figure 13. Crack Tip Coordinate System

Based on these equations, displacement extrapolation method [19, 20] was employed to calculate the stress intensity factors because the J-integral is no longer path independent near the crack when the crack meets the weld. A comparative study reveals that the K_I and K_{II} values for the plane stress state are greater than those values from the plane strain state by 9.8 percent while K_{III} has the same value. Plane strain state was assumed by Bowness and Lee [20]. For the sake of conservativeness and simplicity, plane strain assumption is adopted in this study.

4.2 Verification with Flat Plate

To validate the APDL programs and the crack tip singular elements, solutions of the stress intensity factors for a simple case – flat plate with different crack sizes are computed and compared with the widely accepted results given by Newman and Raju's work [21]. The mesh plan for the flat plate model is consistent with the welded CFCHS T-joints at the crack front. The plate has a length, width and thickness of 200 mm, 500 mm and 8 mm respectively. The following two load cases were considered: the first one is tensile load resulting in a nominal membrane stress of 100 MPa, the other one is bending moment resulting in a nominal stress of 100 MPa in the extreme fiber. The following crack sizes are considered in the validation study: a/c = 0.4 or 0.6, a/t = 0.2, 0.4, 0.6, 0.8. The computation results show that K_{II} and K_{III} are less than one percentage of K_I. Thus K_{II} and K_{III} can be neglected. The values of $K_I/(\sigma_{nom}\sqrt{\pi a/Q})$ at the crack tip from the finite element analysis are compared with the Newman-Raju's solution for both shallow cracks (see Figure 14) and deep cracks (see Figure 15). It can be seen from Figures 14 and 15 that the trends agree well with each other, where σ_{nom} is the nominal stress of the flat plate and Q is a function of a/c in the Newman-Raju's solution. The maximum discrepancy between the two results is 9% occurring at the deepest point and 12% at the crack ends. Clearly, the finite element model can produce reliable SIF results in the case of a flat plate with surface crack.

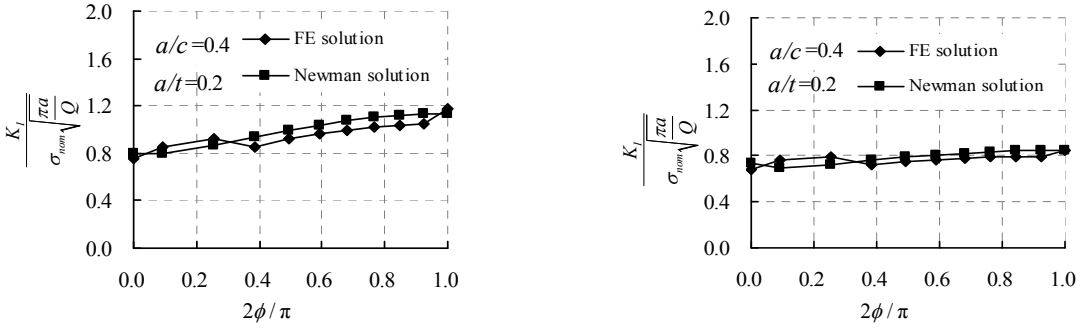

(a) Flat plate in tension (b) Flat plate subjected to pure bending moment

Figure 14. K_I Distribution of a Flat Plate with Shallow Crack

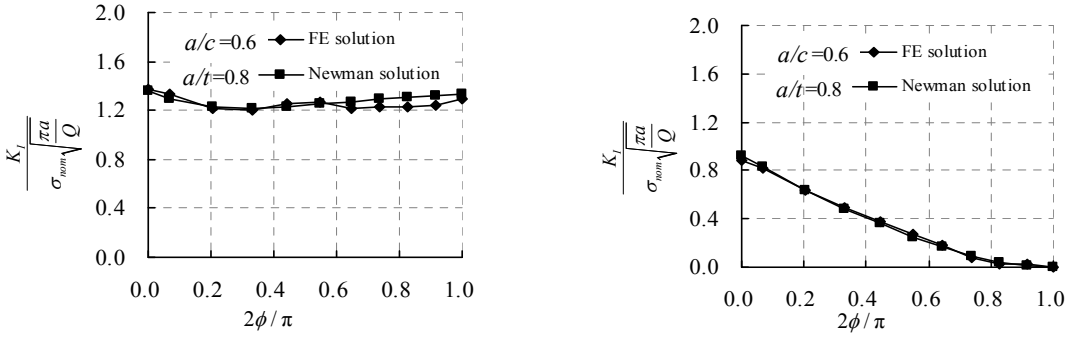

(a) Flat plate in tension (b) Flat plate subjected to pure bending moment

Figure 15. K_I Distribution of a Flat Plate with Deep Crack

4.3 Calculating SIFs for Welded CFCHS T-joint

After the finite element model is validated in a simple flat plate case, the stress intensity factors of the welded CFCHS T-joints with surface cracks were computed from finite element analysis. Specimen CFCHS-2 T-joint in the hot spot stress experiment conducted by Wang et al. [12] at Tongji University is selected for this study, as shown in Figure 1 and Table 1. The dimensions of this T-joint specimen are: β =0.74, γ =15.00, τ =1.00, t_0 =6mm, α =16.89, concrete grade is C50 and steel material is Q345. An axial force range F_r of 60 kN was applied to the brace of CFCHS-2 T-joint. The calculation shows that K_I, K_{II}, K_{III} are on the same order of magnitude and none of them is thus negligible which is different from the afore-mentioned study on plates. Therefore effective stress intensity factor K_{eff} has been used here, which can be computed using Eq. 10 below as given in BS7910 [22]. In this study, $K_{a,eff}$ and $K_{c,eff}$ are chosen to denote the effective stress intensity factor for the deepest point and the crack ends, respectively, which have been calculated for different crack sizes as presented in Figure 16.

$$K_{eff} = \sqrt{K_I^2 + K_{II}^2 + K_{III}^2/(1-\nu^2)} \tag{10}$$

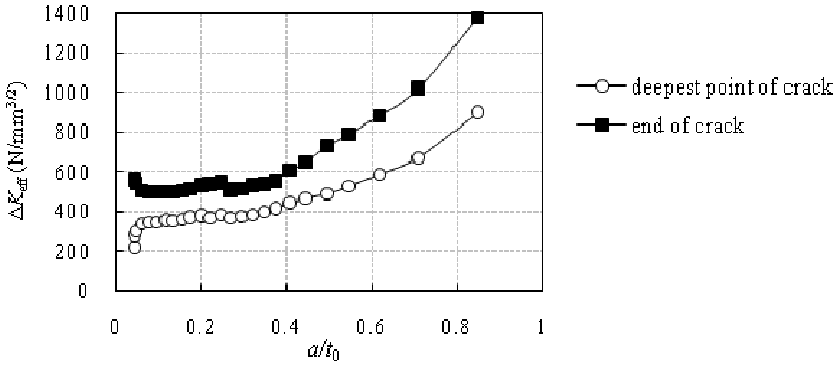

Figure 16. Variation of Effective Stress Intensity Factor at the Deepest Point and Crack Ends during Crack Growth

5. FATIGUE LIFE MODELING AND PREDICTION

Accurate fatigue life prediction depends not only on the use of reliable stress intensity factor solution, but also on the appropriate crack growth law.

5.1 Fatigue Growth Model

Paris' Law, which is the most popular fatigue crack growth model first introduced by Paris and Erdogan [23], relates the fatigue crack growth rate to the stress intensity factor range, as given in Eq. 11 below,

$$\frac{\mathrm{d}a}{\mathrm{d}N} = \mathrm{C}(\Delta K)^{\mathrm{m}} \tag{11}$$

where N is the number of load cycles, a is the crack size, ΔK is the stress intensity factor range, C and m are the crack growth material constants. It is fairly convenient to calculate the fatigue life N by integrating Eq. 11, if the stress intensity factor range (ΔK), the initial crack depth (a_0) and the final crack depth (a_f) are known, i.e.,

$$\int_0^{\mathrm{N}} \mathrm{d}N = \int_{a_0}^{a_f} \frac{\mathrm{d}a}{\mathrm{C}(\Delta K)^{\mathrm{m}}} \tag{12}$$

However, difficulty exists in obtaining the explicit formula of ΔK because stress redistribution occurs with growing crack size, especially for the 3-dimensional complex welded CFCHS T-joint. Paris Law is expressed in an ordinary differential equation with given initial value, and thus the Euler method can be used to convert Eq. 12 into

$$N_{\mathrm{n+1}} = N_{\mathrm{n}} + \frac{\mathrm{d}a}{\mathrm{C}(\Delta K_{\mathrm{n}})^{\mathrm{m}}}, \mathrm{n} = 0,1,2...\mathrm{t} \tag{13}$$

where t is the number of integration subintervals, C and m are taken as the mean value specified in PD6493 [24], i.e. $\mathrm{C} = 1.832 \times 10^{-13}$ and m = 3.0.

5.2 Crack Shape Assumption

The Newman and Raju's "Two point plus semi-ellipse" method [21] defines the semi-elliptical shape relationship of the crack's length and depth. Therefore, the crack shape is assumed to be a semi-ellipse in this study and the crack growth in the two directions is governed by the Paris Law as below,

$$\begin{cases} \dfrac{\mathrm{d}a}{\mathrm{d}N} = \mathrm{C_A}(\Delta K_{\mathrm{a}})^{\mathrm{m}} \\ \dfrac{\mathrm{d}c}{\mathrm{d}N} = \mathrm{C_C}(\Delta K_{\mathrm{c}})^{\mathrm{m}} \end{cases} \tag{14}$$

where ΔK_{a} and ΔK_{c} denote the stress intensity factor range in the thickness and length direction respectively. $\mathrm{C_A}$ is determined from experiments. $\mathrm{C_C}$ is related to $\mathrm{C_A}$, and in the past different relations have been proposed, for example, $\mathrm{C_C} = \mathrm{C_A}$ or $\mathrm{C_C} = 0.9^{\mathrm{m}}\mathrm{C_A}$. In this study, $\mathrm{C_C} = \mathrm{C_A}$ is adopted since it is more conservative, which leads to the following equations.

$$\begin{cases} a_{\mathrm{n+1}} = a_{\mathrm{n}} + \Delta N[\mathrm{C}(\Delta K_{\mathrm{a,eff}})^{\mathrm{m}}] \\ c_{\mathrm{n+1}} = c_{\mathrm{n}} + \Delta N[\mathrm{C}(\Delta K_{\mathrm{c,eff}})^{\mathrm{m}}] \end{cases} \tag{15}$$

5.3 Failure Criterion and Fatigue Life Estimation

The critical crack size is defined as the crack size above which the fatigue limit state (i.e., failure) is assumed to occur. For the fatigue life estimation of circular hollow section joints, it can be determined either as a critical length or as a critical crack depth. Since very few results are available for welded CFCHS joints, the following critical crack size criteria reported for circular hollow section joints might provide insight on how to choose the fatigue failure criterion for welded CFCHS T-joints in terms of critical crack size: (i) half wall thickness as critical crack size used by Schumacher et al. [25]. (ii) 90% wall thickness as critical crack size used Borges and Nussbaumer [26], and Nussbaumer and Haldimann-Sturm [27]. (iii) full wall thickness is more commonly accepted as the critical crack size because crack grows extensively in the length direction when the crack penetrate the full wall thickness. Small variation has little influence on the fatigue life as the majority of the life is spent at small crack depth.

To avoid unexpected failure, people usually take the relatively conservative value which is from serviceability criterion as the critical crack size. In this study, the full thickness of the chord tube is taken as the critical crack size.

The fatigue test results of the welded CFCHS T-joints subjected to axial tension load on its brace show that the load cycles corresponding to the first visually identified crack, crack penetrating through the wall thickness of the steel tubular chord and the specimen's loss of load bearing capacity differ from each other by less than 12%. Therefore, in this study, the simulation is terminated when the crack depth reaches the chord wall thickness, as indicated in Figure 17.

5.4 Results and Discussions

Following the aforementioned procedure, fatigue life of the welded CFCHS T-joint subjected to cyclic tension load in its brace can be calculated and APDL program was developed by the authors to implement this procedure in the ANSYS software. As an example, CFCHS-2 T-joint specimen in Table 1 with L_0 = 1520 mm and L_1 = 753 mm was listed to illustrate the approach. The process is divided into a total of 25 steps to determine the fatigue life, as shown in Table 4.

To evaluate the validity of the fatigue life modeling method, the fatigue life of all welded CFCHS T-joints were predicted and compared with available experimental data, as given in Table 5 and Figure 18. It can be seen from Figure 18 that the FE predicted fatigue lives reasonably agree with the experimental data. The following factors are likely to contribute to the discrepancy between the FE results and experimental results: (i) the mean value of the initial crack sizes given by HSE [16] was used here, which might be different from the actual crack size; (ii) the mean values of the C and m parameters set by the PD6493 [24] as well as Paris Law are only empirical model that is used to approximate the fatigue growth of welded CFCHS T-joints; (iii) residual stress due to the welding process was not taken into account in the finite element model; (iv) Experimentally determined fatigue life might not correspond to the exact time instant when fatigue crack reached the full chord tube thickness due to difficulty in monitoring fatigue crack growth in the thickness direction.

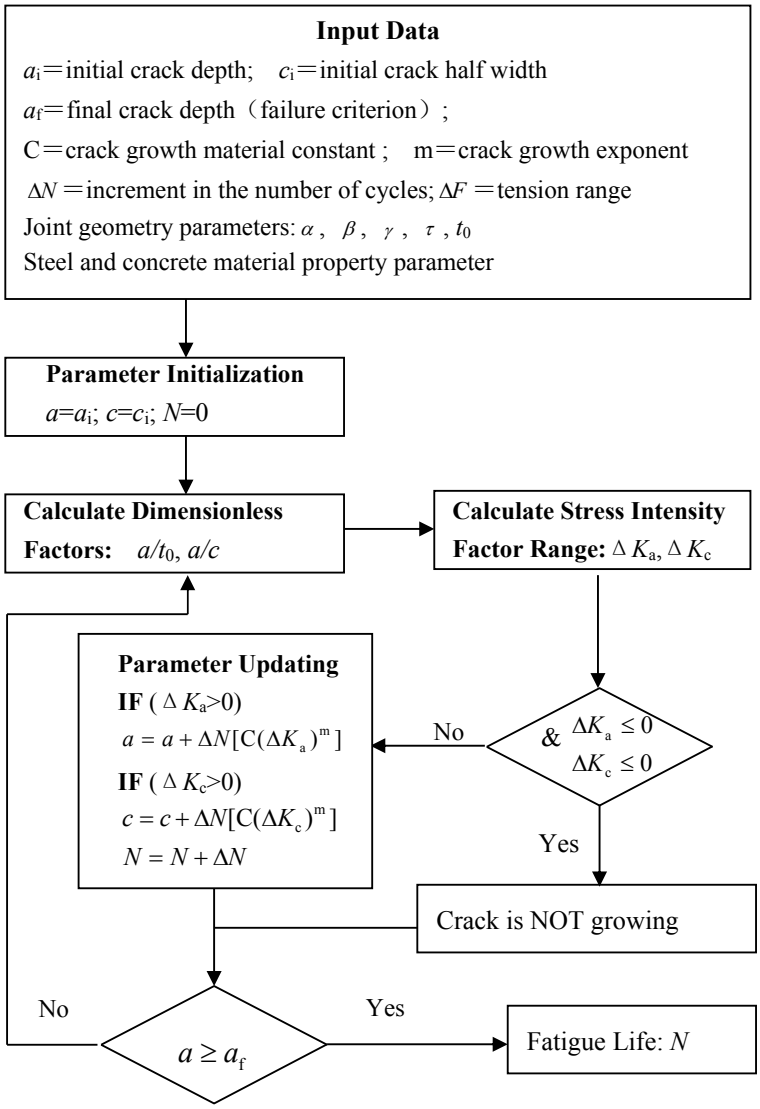

Figure 17. Flow Chart of Fatigue Life Estimation of Welded CFCHS T-joints

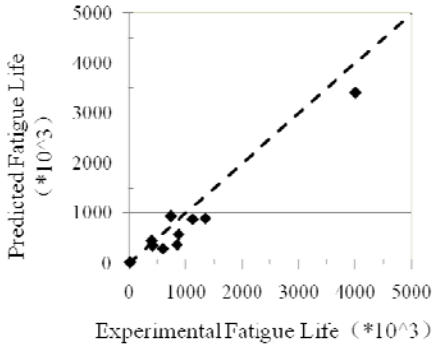

Figure 18. Comparison between Predicted and Experimental Fatigue Lives

Table 4. Illustrative Example for Fatigue Life Estimation of CFCHS-2 T-joint

step	a (mm)	c (mm)	$\triangle K_a$ (N/mm$^{3/2}$)	$\triangle K_c$ (N/mm$^{3/2}$)	$\triangle N$ ($\times 10^3$)	N ($\times 10^3$)	da (mm)	dc (mm)
1	0.25	0.25	213	564	5	5	0.009	0.16
2	0.26	0.41	275	557	5	10	0.02	0.16
3	0.28	0.57	303	545	15	25	0.08	0.44
4	0.35	1.02	338	506	15	40	0.11	0.36
5	0.46	1.37	348	498	15	55	0.12	0.34
6	0.58	1.71	348	496	15	70	0.12	0.34
7	0.69	2.05	351	497	15	85	0.12	0.34
8	0.81	2.39	356	500	15	100	0.12	0.34
9	0.93	2.73	361	507	15	115	0.13	0.36
10	1.06	3.09	366	515	15	130	0.13	0.38
11	1.20	3.46	372	523	15	145	0.14	0.39
12	1.34	3.86	367	532	15	160	0.14	0.41
13	1.48	4.27	386	538	15	175	0.16	0.43
14	1.64	4.70	371	501	15	190	0.14	0.35
15	1.78	5.05	378	513	15	205	0.15	0.37
16	1.93	5.41	386	524	15	220	0.16	0.40
17	2.09	5.81	400	531	15	235	0.18	0.41
18	2.25	6.22	410	547	15	250	0.19	0.45
19	2.45	6.67	445	612	15	265	0.24	0.63
20	2.69	7.30	469	649	15	280	0.28	0.75
21	2.97	8.05	490	731	15	295	0.32	1.07
22	3.30	9.12	530	795	15	310	0.41	1.38
23	3.71	10.50	586	883	15	325	0.55	1.89
24	4.26	12.39	672	1015	15	340	0.84	2.87
25	5.09	15.26	894	1384	7	347	0.92	3.40
26	6.00	18.67						

Table 5. Conparison in Fatigue Life between FEA and Test

Joint	FE predicted fatigue life	Experimental fatigue life
CFCHS-1	880600	1133000
CFCHS-2	346930	410994
CFCHS-3	16350	20295
CFCHS-4	365290	844800
CFCHS-5	931000	737706
CFCHS-6	438680	394800
CFCHS-7	896300	1351350
CFCHS-8	577950	881280
CFCHS-9	291800	599720
CFCHS-10	3406262	4013272

5.4.1 Effect of initial crack size

The data presented in Table 5 is based on assumed initial crack sizes of $a_i = c_i = 0.25$ mm. It is of interest to study the effect of varying initial crack shape on fatigue life estimation. Therefore, four cases with increasing initial crack size ($a_i = c_i = 0.15$ mm, $a_i = c_i = 0.20$ mm, $a_i = c_i = 0.30$ mm, $a_i = c_i = 0.35$ mm) which fall within the slag intrusion range given by HSE [16] were chosen here for a parametric study of the CFCHS-2 T-joint specimen in Table 6. The smaller the initial crack size, the longer the fatigue life. As shown in Table 6, the fatigue life results are about 90% to 104% of the benchmark case with $a_i = c_i = 0.25$ mm. It is found that the fatigue life of welded CFCHS T-joints with normal quality weld (with initial crack size falling within the range specified by HSE) do not change more than 10%.

Table 6. Effect of Initial Crack Size on Fatigue Life Prediction

No.	Initial crack size	Fatigue life N_i	N_i / N_3
1	a_i=c_i=0.15mm	361000	1.04
2	a_i=c_i=0.20mm	348000	1.00
3	a_i=c_i=0.25mm	347000	1.00
4	a_i=c_i=0.30mm	319000	0.92
5	a_i=c_i=0.35mm	312000	0.90

5.4.2 Crack growth behavior

Figure 19 shows the relationships between crack sizes and stress cycles of the CFCHS-2 T-joint specimen while other specimens exhibit a similar trend. It is found that the majority of the T-joints' fatigue life is in the shallow crack stage. In shallow crack stage, fatigue crack grows slowly in the depth direction while propagates more rapidly along its length. This is evidenced by the fact that when $a/t < 0.05$, the ratio of a/c rapidly dropped from 1.0 to 0.35 as crack grows. When the crack depth reached half wall thickness, crack growth rate accelerated in both directions. This observation agrees well with the experiment result that the time duration from the first visual crack to large crack spread over the chord wall is fairly short. Therefore, once fatigue crack becomes visible, retrofit actions such as external reinforcement need to be done near the hot spot stress location on the CFCHS structure under fatigue loading.

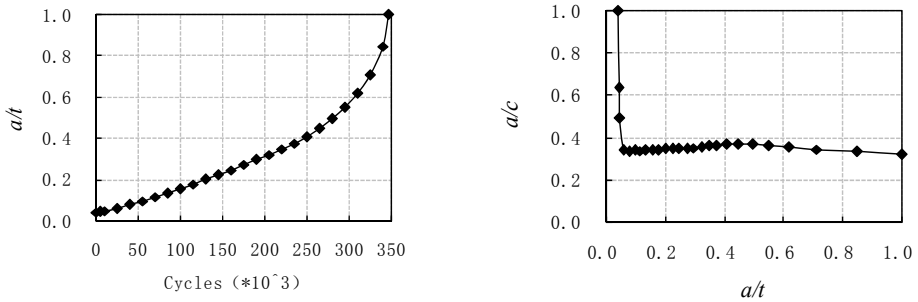

(a) Cycles- *a/t* relation curve (b) *a/t* - *a/c* relation curve

Figure 19. Relationship between Crack Size and Load Cycles

5.4.3 Effect of concrete grade

CFCHS-1, CFCHS-6 and CFCHS-7 T-joints have completely the same non-dimensional geometrical parameters β, γ and τ, but different concrete grades, i.e. different concrete strength (see Table 1). It can be seen from Table 7 that the difference in the experimental SCF_{max} among the three CFCHS T-joints with concrete grades C20, C50 and C70 is not significant, although SCF_{max} decreases as concrete grade increases. Finite element analysis also illustrated this feature. Take an example for a T-joint having the same size as CFCHS-5, SCF_{max} was calculated in the condition of concrete grades from C20 to C80, as shown in Table 8. The calculated SCF_{max} decreases as concrete grade increases, but their difference compared with C50, a usually used concrete grade in concrete-filled tubular structures, is within the range of 4%. This feature means that the improvement in fatigue behavior of tubular joints by filled-in concrete is significantly attributed to the rigidity (not strength) of concrete which improves the rigidity of joint and consequently decreases hot spot stress or stress concentration.

Table 7. Effect of Concrete Grade on SCF_{max} from Test

Joint	CFCHS-6	CFCHS-1	CFCHS-7
Concrete grade	C20	C50	C70
SCF_{max}	7.42	6.79	6.54
SCF_{max} ratio to C50	1.09	1.00	0.96

Table 8. Effect of Concrete Grade on SCF_{max} from FEA

Concrete grade	C20	C30	C40	C50	C60	C70	C80
SCF_{max}	4.39	4.31	4.24	4.21	4.18	4.12	4.12
SCF_{max} ratio to C50	1.04	1.02	1.01	1.00	0.99	0.98	0.98

6. CONCLUSIONS

This paper outlines a fatigue life assessment procedure for welded concrete filled circular hollow section (CFCHS) T-joint subjected to cyclic axial load in its brace. Finite element analysis was first performed to compute the stress intensity factors for the welded CFCHS T-joints. Special APDL programs were developed in the ANSYS software to simulate the T-joint with surface crack. Crack tip singular element is constructed. Experimental data from ten CFCHS T-joint specimens are also presented and compared with the analysis results. The comparison shows the validity of the analysis approach for fatigue life estimation of welded CFCHS T-joints. Specifically, the following conclusions can be drawn based on the findings of this research:

(1) Based on experimental data of hot spot stresses and fatigue crack growth, a computational model for calculating the stress intensity factors of welded CFCHS T-joints has been established.

(2) In order to obtain converged results, the interface nodes located on the interior surface of the steel tube and the external surface of the concrete of welded CFCHS T-joints should be separated even though they are at the same location. Contact elements were added between the interface nodes to simulation friction and bonding effect.

(3) A fatigue life estimation procedure is proposed for welded CFCHS T-joints. The fatigue life estimated from finite element analysis is generally in agreement with the experimental results. The effect of the initial crack size on the joint fatigue life was studied. The change in fatigue life of welded CFCHS T-joints with normal quality weld (with initial crack size falling within the range specified by HSE) was within 10%.

(4) Relationship between the crack size and load cycles is established for the welded CFCHS T-joints. The most part of the T-joints' fatigue life is associated with the shallow crack stage. In shallow crack stage, fatigue crack grows slowly in the depth direction while propagates more rapidly along its length. When the crack depth reached half wall thickness, crack growth rate accelerated in both directions. Thus repair actions (e.g., external reinforcing) need to be taken when the crack becomes visible near the hot spot region of the CFCHS structure subjected to cyclic loading.

(5) The filled-in concrete can effectively increase fatigue strength or fatigue life of a tubular joint. This behavior benefits from the effect of rigidity of concrete which improves the rigidity distribution of the whole joint and then decreases hot spot stress or stress concentration at the weld toe of tubular chord. The concrete grade or concrete strength itself has no significant influence on stress concentration.

ACKNOWLEDGEMENTS

The authors would like to acknowledge the financial support from the Natural Science Foundation of China through the grants NO.50478108 and 51078291. The fourth author is also grateful to the Kwang-Hua Scholar Foundation of Tongji University for providing additional financial support for this research project.

NOTATION

a	Depth of a semi-elliptical crack
a_0	Depth of a initial crack
a_f	Depth of a final crack
c	Half length of a semi-elliptical crack
L_0	Length of a chord
L_1	Length of a brace
d_0	External diameter of a chord
d_1	External diameter of a brace
t_0	Wall thickness of a chord
t_1	Wall thickness of a brace
α	Chord length parameter ($\alpha = 2L_0/ d_0$)
β	Diameter ratio between a brace and a chord ($\beta = d_1/ d_0$)
γ	Half diameter-to-thickness ratio of a chord ($\gamma = d_0/(2\ t_0)$)
τ	Wall thickness ratio between a brace and a chord ($\tau = t_1/ t_0$)
h_{f1}	Height of weld toe on the chord side
h_{f2}	Height of weld toe on the brace side
c_1	Outer circumference of a chord
c_2	Inner circumference of a chord
c_3	Outer circumference of a brace
c_4	Inner circumference of a brace
c_5	Projected length in plane of weld toe on the chord side
K	Stress intensity factor
K_I	Stress intensity factor of Mode I
K_{II}	Stress intensity factor of Mode II
K_{III}	Stress intensity factor of Mode III
ΔK	Stress intensity factor range
K_{eff}	Effective stress intensity factor
γ, θ	Polar co-ordinate system for a crack tip
G	Elastic shear modulus
ν	Poisson's ratio
u, v, w	Local radial, normal and tangential displacement
C	Paris's crack growth law coefficient
m	Paris's crack growth law exponent
N	Number of cycles
σ_{nom}	Nominal stress in a plate
Q	Shape factor in Newman-Raju's solution
SCF	Stress concentration factor

REFERENCES

[1] Wardenier, J., Packer, J.A., Zhao, X.L. and van der Vegte, G.J., "Hollow Sections in Structural Applications", Delft Bouwen met Staal, 2010, pp.145-150.

[2] Zhao, X.L., Han, L.H. and Lu, H., "Concrete Filled Tubular Members and Connections", London: Taylor & Francis, 2010, pp.110-150.

[3] Zhao, X.L., Herion, S., Packer, J.A., Puthli, R.S., Sedlacek, G., Wardenier, J., Weynand, K., van Wingerde, A.M. and Yeomans, N.F., "Design Guide for Circular and Rectangular Hollow Section Welded Joints under Fatigue Loading", CIDECT, TUV-Verlag, 2001, pp. 25-32.

[4] Lee, C., Chiew, S., Lie, S. and Ji, H., "Fatigue Behaviors of Square-to Square Hollow Section T-joint with Corner Crack. II: Numerical Modeling", Engineering Fracture Mechanics, 2007, Vol. 74, No. 5, pp. 721-738.

[5] Lee, C.K., Chiew, S.P., and Lie, S.T. et al, "Experimental Study on Stress Concentration Factors for Partially Overlapped Circular Hollow Section K-joints", Advanced Steel Construction, 2009, Vol. 5, No. 4, pp. 481-499.

[6] van Wingerde, A.M., Packer, J.A. and Wardenier, J., "IIW Fatigue Rules for Tubular Joints", IIW International Conference on Performance on Dynamically Loaded Welded Structures, San Francisco, USA, 1997, pp. 98-107.

[7] Tong, L. and X. L. Zhao, et al. "Fatigue Behavior of Welded Thin-walled T-joints between Circular and Square Hollow Sections." International Journal of Steel Structures, 2006, Vol. 6, No. 1, pp. 37-44.

[8] Udomworarat, P., Miki, C., Ichikawa, A., Sasaki, E., Sakamoto, T., Mitsuki, K. and Hasaka, T., "Fatigue and Ultimate Strengths of Concrete Filled Tubular K-joints on Truss Girder", Journal of Structural Engineering, 2000, Vol. 46A, pp. 1627-1635.

[9] Tong, L.W., Sun, C.Q., Chen, Y.Y., Zhao, X.L., Shen, B. and Liu, C.B., "Experimental Comparison in Hot Spot Stress between CFCHS and CHS K-joints with Gap", Proceedings of 12th International Symposium on Tubular Structures, Shanghai, China, 2008, pp. 389-395.

[10] Mashiri, F.R. and Zhao, X.L., "Square Hollow Section T-joints with Concrete-filled Chords subjected to in-plane Fatigue Loading in the Brace", Thin-Walled Structures, 2010, Vol.48, No. 2, pp. 150-158.

[11] Zhao, X.L. and Tong, L.W., "New Development in Steel Tubular Joints", Advances in Structural Engineering, 2011, Vol. 14, No. 4, pp. 699-715.

[12] Wang, K., Tong, L.W., Zhu, J., Shi, W.Z., Mashiri, F.R. and Zhao, X.L., "Fatigue Behaviour of Welded T-joints between CHS Brace and CFCHS Chord under Axial Loading in the Brace", Journal of Bridge Engineering, 2013, Vol. 18, No. 2, pp. 142-152.

[13] Hobbacher, A., "Stress Intensity Factors of Welded Joints", Engineering Fracture Mechanics, 1993, Vol. 46, No. 2, pp. 173-182.

[14] Bowness, D. and Lee, M.M.K., "The Development of an Accurate Model for the Fatigue Assessment of Doubly Curved Cracks in Tubular Joints", International Journal of Fracture, 1995, Vol. 73, No. 2, pp. 129-147.

[15] American Welding Society (AWS), "Structure Welding Code-steel, 17th Ed.", Miami, 2000, pp. 10-16.

[16] Health and Safety Executive (HSE), "Background to New Fatigue Guidance for Steel Joints and Connections in Offshore Structures", O/S Technical Report OTH 92 390, 1999, pp. 105-110.

[17] ANSYS, Release 14.0, Help System, "Coupled Field Analysis Guide", ANSYS, Inc., 2011.

[18] Barsoum, R.S., "Triangular Quarter-point Elements as Elastic and Perfectly-plastic Crack Tip Elements", Int. J. Num. Meth. Eng., 1977, Vol. 11, No. 1, pp. 85-98.

[19] Chiew, S.P., Lie, S.T., Lee, C.K., and Huang, Z.W., "Stress Intensity Factors for a Surface Crack in a Tubular T-joint", International Journal of Pressure Vessels and Piping, 2001, Vol. 78, No. 10, pp. 677-685.
[20] Bowness, D., Lee, M.M.K., "A Finite Element Study of Stress Fields and Stress Intensity Factors in Tubular Joints", Journal of Strain Analysis, 1995, Vol. 30, No. 2, pp. 135-142.
[21] Newman, J.C. and Raju, I.S., "An Empirical Stress Intensity Factor Equation for the Surface Crack", Engineering Fracture Mechanics, 1981, Vol. 15, No. 1-2, pp. 185-192.
[22] British Standards Institution BS7910, "Guide on Methods for Assessing the Acceptability of Flaws in Metallic Structures", London, UK, 2005, pp.168-185.
[23] Paris, P.C., Edorgan, F., "Critical Analysis of Crack Propagation Laws", ASME Journal of Basic Engineering, 1963, Vol. 85, No. 4, pp. 528-534.
[24] British Standards Institution PD6493, "Guidance on Methods for Assessing the Acceptability of Flaws in Fusion Welded Structures", London, UK, 1991, pp. 35-45.
[25] Schumacher, A. and Nussbaumer, A., "Experimental Study on the Fatigue Behavior of Welded Tubular K-joints for Bridges", Engineering Structures, 2006, Vol. 28, pp. 745-755.
[26] Borges, L. and Nussbaumer, A., "Advanced Numerical Modeling of Fatigue Size Effects in Welded CHS K-joints", Proceedings of 12th International Symposium on Tubular Structures, China, 2008, pp. 135-144.
[27] Nussbaumer, A. and Haldimann-Sturm, S.C., "Fatigue of Bridge Joints using Welded Tubes or Cast Steel Node Solutions", Proceedings of the 11th International Symposium on Tubular Structures, London, 2006, pp. 61-68.